PHYSICALLY-BASED MODELS FOR ELEVATED TEMPERATURE LOW CYCLE FATIGUE CRACK INITIATION AND GROWTH IN RENE 88DT

A Dissertation
Presented to
The Academic Faculty

By

Kip O. Findley

In Partial Fulfillment
Of the Requirements for the Degree
Doctor of Philosophy in
Materials Science and Engineering

Georgia Institute of Technology

August, 2005

PHYSICALLY-BASED MODELS FOR ELEVATED TEMPERATURE LOW CYCLE FATIGUE CRACK INITIATION AND GROWTH IN RENE 88DT

Approved by:

Dr. Ashok Saxena, Advisor
School of Materials Science and Engineering
Georgia Institute of Technology

Dr. Tom Sanders
School of Materials Science and Engineering
Georgia Institute of Technology

Dr. Arun Gokhale
School of Materials Science and Engineering
Georgia Institute of Technology

Dr. Steven Johnson
School of Materials Science and Engineering
Georgia Institute of Technology

Dr. David McDowell
School of Materials Science and Engineering
Georgia Institute of Technology

Date Approved: April 22, 2005

To all those from whom I've garnered a
lifelong education - my parents,
my mentors, my closest friends,
and Dawn

ACKNOWLEDGEMENTS

I would like to express my sincere gratitude to the large number of people who aided me substantially in this work. First, I would to thank my advisor, Dr. Ashok Saxena. His insight has provided invaluable lessons on both technical and non-technical matters, and I have spent a great deal of time drawing from his wisdom and learning from his professionalism. I would also like to thank my committee members for their time and support. I have had very constructive and educational discussions with Dr. Arun Gokhale and Dr. David McDowell about different aspects of this research. Dr. Tom Sanders not only provided technical assistance but also presented me an excellent opportunity to learn about classroom education. I've enjoyed working with Dr. Steve Johnson through the MPRL and in educational settings. I'm also very appreciative of the discussions and insight I've drawn from Dr. Stephen Antolovich and Dr. Naresh Thadhani. I am greatly indebted to the entire MSE staff, especially Rick Brown, Robert Cooper, and Susan Bowman.

I would like to thank my peers in the department and at the University of Arkansas. I greatly enjoyed working with my fellow group members, colleagues, and mentors including Art Counts, Alejandro Ibanez, Shubhra Bansal, Heather Major, Matt Trexler, Ali Gordon, and Dr. Srinivasan. I owe special thanks to Sau Wee Koh for his assistance in finite element analysis and I hope to continue collaboration with him. The MSE community has provided a strong network of support and companions, several of which will evolve into lifelong friendships.

Finally, the support, love, and wisdom of my closest family and friends are a pillar that I constantly lean on and are something I cherish beyond words. My parents have given me love beyond my imagination, catalyzed my dreams, and been amazing role models. Dawn is my inspiration for the future.

TABLE OF CONTENTS

ACKNOWLEDGEMENTS iv

LIST OF TABLES vii

LIST OF FIGURES viii

NOMENCLATURE xiv

SUMMARY xvi

CHAPTER 1 INTRODUCTION 1

1.1 Background 1

1.2 Objectives 3

1.3 Overview of Thesis 4

CHAPTER 2 LITERATURE REVIEW 6

2.1 Microstructural Evolution in Nickel-Base Superalloys 6

2.2 High Temperature Crack Initiation and Propagation in Nickel-Base Superalloys 15

2.2.1 Crack Initiation and Small Crack Growth Mechanisms in Nickel-Base Superalloys 16

2.2.2 Long Fatigue Crack Propagation Mechanisms for Nickel-Base Superalloys 31

2.3 Literature Review Summary 36

CHAPTER 3 EXPERIMENTAL PROCEDURE 38

3.1 Material 38

3.2 Microstructural Characterization 39

3.2.1 Grain Size Determination 39

3.2.2 γ' Precipitate Volume Fraction and Size Distribution 40

3.2.3 Carbide Characterization Methods 41
3.3 Mechanical Testing 48
3.3.1 Tensile Testing 50
3.3.2 Low Cycle Fatigue Testing 51
3.3.3 Fracture and Crack Analysis 55
3.3.4 Fracture Toughness Testing 57
3.3.5 Fatigue Crack Growth Testing 59
3.4 Experimental Procedure Summary 62
CHAPTER 4 RESULTS AND DISCUSSION 63
4.1 Materials Characterization 63
4.2 Mechanical Testing 72
4.2.1 Tensile Testing 73
4.2.2 Low Cycle Fatigue Testing 74
4.2.3 Fracture Toughness and Fatigue Crack Growth Testing 99
4.3 Long Crack Growth Models Applied to Low Cycle Fatigue Conditions 110
4.4 Crack Initiation and Short Crack Growth Models 138
4.5 Results and Discussion Summary 153
CHAPTER 5 CONCLUSIONS AND RECOMMENDATIONS 154
APPENDIX A LOW CYCLE FATIGUE ΔΣ VERSUS ΔE CURVES 160
APPENDIX B TEMPERATURE VERSUS TIME HEAT TREATMENT DIAGRAMS FOR MICROSTRUCTURE CONDITIONS N AND O 163
APPENDIX C LOW CYCLE FATIGUE FRACTURE SURFACE IMAGES 165
REFERENCES 170

LIST OF TABLES

2.1. Role of various alloying elements in determining the properties of superalloys.....13

2.2. Summary of defect initiation sites on LCF fracture surfaces from extruded and forged Rene 95.....19

3.1. Chemical composition of Rene 88DT. Values are in weight percent.....38

3.2. Description of the heat treatments performed on the bore drop material.....39

3.3 Nominal composition of IN100.....41

3.4. Total and grain boundary carbide number per unit volume averages and standard deviations.....45

3.5. Tabulated data on the carbide stereological parameters.....46

4.1. Summary of the target heat treatments performed on Rene 88DT bore drop material.....64

4.2. Expected γ' size distributions from heat treatments described above.....64

4.3. Actual heat treatments for microstructural conditions N and O.....65

4.4. Summary of the grain size and γ' characteristics for the three microstructures.....70

4.5. Summary of the tensile properties for the experiments shown in Figure 4.8.....74

4.6. Test matrix for low cycle fatigue property comparison.....75

4.7. Summary of low cycle fatigue results from N, O, and P conditions.....80

4.8. Summary of initial crack dimensions in P specimens exhibiting subsurface initiation.....115

4.9. The predicted final crack dimensions and corresponding number of cycles to reach these dimensions for the P specimens exhibiting subsurface crack growth.....118

4.10. Summary of results obtained from the fitted equations based on FEA experiments.....131

4.11. Summary of P condition crack initiation sites.....140

LIST OF FIGURES

1.1. Schematic of the typical stress-strain cycle in a blade attachment section of an aircraft turbine disk during a complete take-off to landing cycle 2

2.1. Mean diameter of cooling γ' precipitates versus cooling rate in continuous cool experiments 9

2.2. Mean diameter of cooling γ' precipitates versus transition temperature in interrupted cooling experiments 9

2.3. Frequency of surface initiated failure in LCF tests conducted at 540ºC (1004ºF) in strain controlled tests 15

2.4. Initial normalized stress intensity at an inclusion versus number of cycles to failure for Astroloy 21

2.5. Comparison of predicted and actual lives based on ΔKeff for semielliptic cracks on the surface 22

2.6. Comparison of predicted and actual lives based on ΔK_{eff} for elliptic cracks in the subsurface 23

2.7. Slip band crack initiation mechanisms for an FCC material in response to a tensile force 26

2.8. Probability of failure based on low cycle fatigue results performed at 593ºC and at various stress levels 30

2.9. σ_{max}-N curve showing a divergence of crack initiation mechanisms 31

2.10. Plot of da/dN versus $10^3/T$ at $\Delta K = 33$ MPa*$m^{1/2}$ for several nickel base superalloys 32

2.11. Crack growth rate versus ΔK normalized by yield strength and Young's modulus for alloys with different values of mismatch (δ), APBE (Γ), and V_v γ' 33

3.1. Schematic of the disector probe. Any particle that lies at least partially within the rectangular area is counted if it doesn't intersect a solid line and if it isn't present on the other plane used for analysis 43

3.2. Disector probe applied to images 4 and 5 of the IN100 stack 43

3.3. The running average of the total number of carbides per unit volume plotted against fields of view 45

3.4. Top view of a bore drop received from GE showing how it was divided into slabs for heat treatment and specimen machining 49

3.5. Side view of a bore drop slab demonstrating how low cycle fatigue and tensile specimens were obtained from the material....49

3.6. Schematic of the tensile specimen geometry (units are in centimeters) 50

3.7. Schematic of the specimen used in uniaxial low cycle fatigue experiments 51

3.8. SEM image of a crack initiation region on a low cycle fatigue specimen....52

3.9. Picture of the one arm bandit applied to the low cycle fatigue setup, which uses a lever that rests on the actuator to measure actuator displacement 54

3.10. Stress-strain hysteresis loops obtained in the saturation regime for Rene 88DT with an applied strain range of $\Delta\varepsilon = 0.75\%$, R=-1, and a testing temperature of 650°C 55

3.11. Stress-strain hysteresis loops obtained in the saturation regime for Rene 88DT with an applied strain range of 1.5%, R=-1, and a testing temperature of 650°C 56

3.12. Schematic of the 1/2T C(T) specimen used to determine fracture toughness in microstructure conditions N and O 58

3.13. Schematic of the 1T C(T) specimen used to obtain fatigue crack growth rates for microstructure conditions N and O 60

4.1. Primary γ' size distribution for the three microstructural conditions examined and tested 65

4.2. SEM micrograph of γ' precipitates in the N microstructure 67

4.3. SEM micrograph of γ' precipitates in the O microstructure 67

4.4. SEM micrograph of γ' precipitates in the Ladish microstructure 68

4.5. Distribution of the nearest neighbor distance between the γ' precipitates for the three microstructural conditions 69

4.6. Estimated probability density distribution of the carbide effective diameters in the N and O conditions 71

4.7. Spatial distribution of carbides within the N microstructure 72
4.8. Stress-strain curves for Rene 88DT tested at room temperature, 399°C, and 649°C 74

4.9. Plot of the typical stress range versus number of cycles for conditions N and O tested at Δε=0.66% and 650ºC 77

4.10. Stress range versus cycle number for a specimen from the P condition tested at Δε=0.66% and 650ºC 78

4.11. Bar chart demonstrating the significant difference in cycles to failure between the P and N and O conditions 83

4.12. Plot of the strain range versus number of cycles to failure for the N, O, and P conditions. Data from the Caton *et al.* is also included 84

4.13. Low magnification stereoscope image of the fracture surface of specimen ND-1 tested at Δε=0.66% and 650ºC 86

4.14. Low magnification stereoscope image of the fracture surface of P 233 tested at Δε=0.66% and 650ºC 87

4.15. SEM image of the crack initiation region in specimen ND-1 tested at Δε=0.66% and 650ºC 88

4.16. SEM image of a specimen tested at Δε=0.79% and 650ºC tilted so the exterior surface of the specimen is normal to the electron beam in the vicinity of the crack initiation region 89

4.17. Side view of a polished section around the crack initiation region in specimen OD-5, tested at Δε = 0.75% and 650ºC 90

4.18. Low magnification image of the low cycle fatigue fracture surface from P 222 tested at Δε=0.79% and 650ºC. The oxidation pattern outlines a subsurface crack initiation site 92

4.19. SEM image of a cluster of particles in the initiation region for a specimen tested at Δε=0.79% and at 650ºC. 94

4.20. Higher magnification SEM image of the particle cluster shown in Figure 4.19 94

4.21. a) Baseline EDS spectrum obtained from the matrix of P 144, Δε = 0.79% and
b) Spectrum obtained from a particle amongst the aluminum oxide particle cluster 95

4.22. Plot of distance of the crack initiation site to the surface of the low cycle fatigue specimen versus number of cycles to failure among P condition specimens tested at $\Delta\varepsilon = 0.66\%$ and $\Delta\varepsilon = 0.79\%$ and 650ºC 97

4.23. Plot of load versus actuator stroke, exhibiting partial unloading due to crack "pop-in" during a fracture toughness experiment at 650ºC 101

4.24. One half of the fracture toughness specimen fracture surface tested at 650ºC showing the precrack, crack growth during the fracture toughness experiment, and striations due to crack "pop-in" 101

4.25. Load versus load-line displacement for a fracture toughness experimented conducted on specimen from the microstructure condition N tested at 650ºC.....102

4.26. Crack growth resistance curves and a K-applied curve used to determine an approximate value of K_C.....105

4.27. Loading portion of the cyclic stress-strain curve.....107

4.28. Crack growth data taken at 650ºC plotted on a log-log scale obtained from microstructure conditions N and O and compared to data from Krueger *et al*. [1] and Caton *et al.* [2].....109

4.29. Configuration and parameters for an embedded elliptical crack in a plate.....111

4.30. Configuration and parameters for a surface semi-elliptical crack in a plate.....111

4.31. The Newman and Raju [3] solution for an elliptical crack in a rectangular bar applied to the round bar fatigue specimens from microstructure condition P 113

4.32. SEM image and corresponding prediction of the crack growth shape around the crack initiation region in specimen P 222.....115

4.33. SEM image and corresponding prediction of the crack growth shape around the crack initiation region in specimen P 122R 116

4.34. Crack configuration for a semi-elliptical crack in a round bar 120

4.35. Normalized stress intensity factor versus crack tip location for tension and bending.....122

4.36. Stress intensity versus crack depth at point A using relationships obtained from Carpinteri [4] and Newman and Raju [3] analyses 123

4.37. Cross section of the round bar fatigue specimen. The black points indicate the

focal points for the J-integral and crack growth analysis 125

4.38. Side (left) and cross-sectional (right) image of the finite element models of a semi-elliptical crack in a round bar fatigue specimen 126

4.39. Linear elastic J-integral comparison between values obtained from the Newman and Raju solution and the finite element analysis in this research 127

4.40. Plot of crack aspect ratio versus crack length evolution using the data fit obtained from ABAQUS analysis for various starting values of each parameter.....129

4.41. Fatigue striations on a specimen tested with a strain range of 0.66% at 650ºC.....133

4.42. Fatigue fracture surface from a specimen tested with a strain range of 0.66% at 650ºC.....133

4.43. Comparison of the aspect ratio evolution versus crack depth between experimental results and the data fit prediction obtained from FEA results for P 155 135

4.44. Comparison of the aspect ratio evolution versus crack depth between experimental results and the data fit prediction obtained from FEA results for P 233 136

4.45. SEM image of the crack initiation region of a P condition specimen tested with $\Delta\varepsilon = 0.66\%$.....139

4.46. Aluminum oxide particles in a planar metallographic section from the gage section of P 222 after testing.....141

4.47. Approximate distribution of the Fatemie-Socie parameter for the N and O versus the P conditions with $\Delta\varepsilon=0.66\%$.....149

4.48. Average of the Fatemie-Socie parameter for several strain ranges 150

A.1. Plot of $\Delta\sigma$ versus $\Delta\varepsilon$ for the three microstructure conditions tested with $\Delta\varepsilon = 0.66\%$.....160

A.2. Plot of $\Delta\sigma$ versus $\Delta\varepsilon$ for the three microstructure conditions tested with $\Delta\varepsilon = 0.75\%$ to $\Delta\varepsilon = 0.79\%$.....161

A.3. Plot of $\Delta\sigma$ versus $\Delta\varepsilon$ for the P condition tested with $\Delta\varepsilon = 0.94\%$ 161

A.4. Plot of $\Delta\sigma$ versus $\Delta\varepsilon$ for the P condition tested with $\Delta\varepsilon = 1.15\%$ 162

B.1. Temperature versus time for the heat treatment that was used to produce microstructure condition N 163

B.2. Temperature versus time for the heat treatment that was used to produce microstructure condition O 164

C.1. Crack initiation region in specimen P 155 tested at $\Delta\varepsilon = 0.66\%$ 165

C.2. Subsurface crack initiation region in specimen P 144R tested at $\Delta\varepsilon = 0.75\%$. The inset shows a lower magnification stereoscope image of the specimen 166

C.3. Crack initiation region in an N condition specimen tested at $\Delta\varepsilon = 0.75\%$. The inset shows a lower magnification SEM image of the initiation site 166

C.4. Crack initiation region in an O condition specimen tested at $\Delta\varepsilon = 0.75\%$. The inset shows a lower magnification SEM image of the initiation site 167

C.5. Subsurface particle cluster in specimen P 122R tested at $\Delta\varepsilon = 0.79\%$ 167

C.6. Subsurface particle cluster in specimen P 133 tested at $\Delta\varepsilon = 0.79\%$ 168

C.7. Crack initiation region of specimen P 111 tested at $\Delta\varepsilon = 0.94\%$. A small particle lies at the surface of the specimen 168

C.8. Crack initiation region of specimen P 200 tested at $\Delta\varepsilon = 1.15\%$ 169

C.9. Crack initiation region of an O condition specimen tested at $\Delta\varepsilon = 1.5\%$ exhibiting adjacent crack initiation sites 169

NOMENCLATURE

a	crack length
a_f	final crack length
a_0	initial crack length
a_i	crack length after 'i' cycles
b	plate width for Newman and Raju stress intensity solution
B	compact test specimen width
c	elliptical or semi-elliptical crack width
c_0	initial elliptical or semi-elliptical crack width
c_f	final elliptical or semi-elliptical crack width
C	coefficient of Paris Law crack growth
C(T)	compact test specimen
d	grain size
da/dN	rate of crack growth over number of cycles
DT	damage tolerant
e	effective slip irreversibility factor
E'	effective modulus
EBSD	electron backscatter diffraction
EDS	energy dispersive spectroscopy
F	stress intensity correction factor
FEA	finite element analysis
FIB	focused ion beam
FCG	fatigue crack growth
J-integral	a path-independent integral characterizing stress intensity
k	lattice frictional resistance stress
K_c	critical linear elastic stress intensity parameter
K_I	mode I linear elastic stress intensity parameter
K_{Ic}	mode I critical linear elastic stress intensity parameter
LCF	low cycle fatigue

LEFM	linear elastic fracture mechanics
m	Ramberg-Osgood hardening exponent
M	Taylor factor
m’	cyclic Ramberg-Osgood hardening exponent
n	Paris Law exponent
n_i	number of cycles required to initiate a crack
N	a microstructural condition in this research
N_f	number of cycles for a part to fail
O	a microstructural condition in this research
P	a microstructural condition in this research
P_Q	load used to determine possible K_c
Q	shape factor of an elliptical crack
r	distance from the crack tip
r_y	radius of the plastic zone around a crack tip
R	ratio of the minimum and maximum applied stress
t	thickness of a rectangular bar or diameter of a round bar
v/P	elastic compliance
V_0	initial output voltage
V_i	output voltage at cycle number ‘i’
w	slip band spacing
W	width of a cracked specimen
α	Ramberg-Osgood hardening coefficient
α’	Ramberg-Osgood hardening coefficient
γ	matrix phase in nickel-base superalloys
γ’	strengthening precipitate in nickel-base superalloys
γ_s	surface energy required to open up a crack
γ_p	plastic shear strain within a slip band
ΔJ	range of the J-integral in fatigue conditions
$\Delta J_{elastic}$	elastic part of ΔJ
$\Delta J_{plastic}$	plastic part of ΔJ
ΔK	range of K in fatigue conditions

ΔK_{eff}	effective range of K in fatigue conditions
$\Delta\gamma^{p}_{max}$	maximum plastic shear strain in a slip band
$\Delta\varepsilon$	strain range in fatigue conditions
$\Delta\varsigma$	stress range in fatigue conditions
$\Delta\tau$	shear stress range in fatigue conditions
ε	strain
ε_{min}	minimum strain in fatigue
ε_{max}	maximum strain in fatigue
μ	shear modulus
ν	Poisson's ratio
σ	stress
σ^{c}_{ys}	cyclic yield stress
σ_{max}	maximum stress in fatigue
σ_{min}	minimum stress in fatigue
σ_{n}	normal stress
σ_{y}	yield stress
φ	angle defining location along an elliptical crack front

SUMMARY

Currently, in the aircraft engine industry, materials development time lags design time by several years. Thus, it is necessary to develop models for understanding the life-limiting properties of engine materials, to predict material lifetimes based on structure-property relationships, and to reduce the test matrix and more importantly, time lost, necessary to validate a material for application. In this research, the high temperature fatigue crack initiation and growth mechanisms in the nickel-base superalloy Rene 88DT were studied and physically-based models were developed for fatigue life prediction.

Three microstructural conditions of Rene 88DT, labeled N, O, and P, were characterized and it was found that while the γ' volume fractions and size distributions were similar for the three conditions, the grain size for conditions N and O was approximately a factor of three larger than the grain size for condition P. A large disparity was also observed in the low cycle fatigue lives of specimens from the three conditions tested at 650ºC and with multiple strain ranges; the fatigue lives of the P condition specimens were more than an order of magnitude larger than the fatigue lives of the N and O condition specimens. Additionally, two crack initiation mechanisms were observed: crack initiation from damage accumulated in slip bands on the surface of the specimens and crack initiation from subsurface inclusions, which only occurred at low strain ranges in the P condition specimens.

Analysis of long crack growth was performed using Newman and Raju's solution for an elliptical crack in a square bar to approximate subsurface crack initiation, growth, and shape evolution in the round bar fatigue specimens, and finite element analysis was conducted to estimate the fatigue life and shape evolution of a semi-elliptical surface crack. Though both analyses are able to estimate the crack shape evolution, both predict much lower fatigue lives than those observed in the low cycle fatigue experiments indicating that crack initiation and short crack growth are the life-controlling stages of the total fatigue life and fracture mechanics cannot predict the entire fatigue lifetime.

An attractive approach for predicting the probability of crack initiation from slip band cracking is the Fatemi-Socie parameter because it accounts for shear plastic strain damage accumulation within a slip band and the normal stress to the slip band acting to open the slip band crack and thus, is multiaxial in nature. It was modified to include grain size and orientation and applied to random grain orientations from the N, O, and P conditions. The averages and distributions of the Fatemi-Socie parameter for different grain orientations are much larger in the N and O conditions than they are in the P condition due to the difference in grain size. This implies that slip band cracking is much easier in the N and O conditions because of their larger average grain size, which provides an explanation for the disparity in fatigue lives between the three microstructure conditions. The Fatemi-Socie parameter can also justify why subsurface crack initiation only occurs at low strain ranges and only in the P condition, the microstructure with the smallest grain size. The model does not account for the constraint imposed by the grains

surrounding the crack initiating grain, but further studies into these effects could make the Fatemi-Socie parameter a complete and powerful crack initiation model.

CHAPTER 1

INTRODUCTION

1.1. Background

The aircraft and power generation gas turbine industry is constantly striving to improve the performance of their turbines by raising their operating temperatures and increasing the stresses in their hot-section components such as disks, blades, and vanes. Nickel-base superalloys currently used in engine applications must be modified or new alloys must be developed to achieve this goal. However, there are limits to the extent a material can be modified, and thus the capabilities and performance of gas turbines are ultimately limited by materials that are used in these critical components. Therefore, materials behavior models such as those for predicting the low cycle fatigue behavior and the creep-fatigue crack growth behavior that assist in accurately predicting the in-service behavior of components are extremely useful during the design of gas turbines. Further, the variation in properties as a function of microstructure and an understanding of the microstructural factors that affect crack initiation and propagation life is equally important.

Nickel-base superalloys are chosen for intermediate temperature applications such as in aircraft turbine disks because of their relatively high strength at the anticipated service temperatures that range from 650^0C to 700^0C for sustained periods during normal operation. Since disks are highly stressed during service, fatigue resistance, strength, and toughness are important material properties at these high temperatures. Disk materials are commonly manufactured using powder metallurgy processing to reach the strength

requirements of that application but the process leads to high probability of defects and variability in the microstructure. The typical duty cycle for the disks is modeled as a fatigue stress cycle with a dwell or hold time for the purposes of predicting crack initiation and propagation life as shown in Figure 1.1 [5].

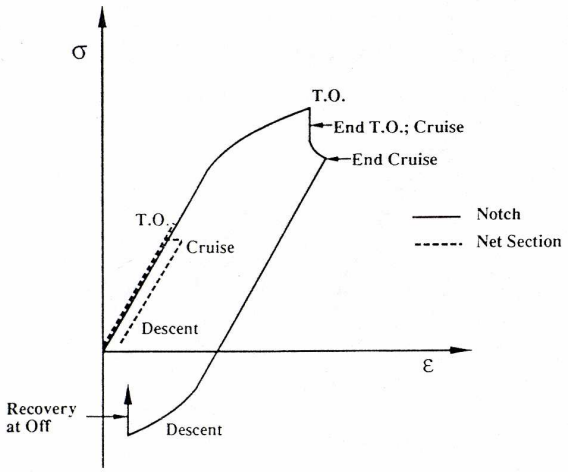

Figure 1.1. Schematic of the typical stress-strain cycle in a blade attachment section of an aircraft turbine disk during a complete take-off to landing cycle [5].

The time required to develop and implement new materials is approximately eight to fifteen years, while the time required to design new turbines is typically half of that [6]. This further underscores the importance and need for materials behavior models that can be used to reduce the time to develop new materials in demanding applications such as the hot-section components of gas turbines. This study was part of an initiative by the Defense Advanced Research Projects Agency (DARPA) and entitled the Accelerated Insertion of Materials (AIM). The AIM objective, involving several organizations including industry and university representatives, was to establish a materials development framework to accelerate the implementation of new materials into service.

Several tasks were defined to contribute to a larger designer knowledge base including searching for effective materials representation techniques, modifying experimental strategies to obtain more data in a shorter time, developing physically-based models for mechanical properties, and applying existing computational models for life prediction. If these tasks were completed, designers would essentially have a library of models, techniques, and computational programs to design and develop high performance, low cost materials. This would also promote new materials development over the existing practice of material modification to address specific needs.

Georgia Tech was charged with the task of computationally, analytically, and experimentally examining creep-fatigue crack initiation and growth interactions in the disk material chosen for the AIM project, Rene 88DT. The combined results of this effort, including the research described in this thesis, should produce a more complete understanding of the microstructural influence on creep-fatigue crack initiation and growth conditions, provide a data set relating processing and microstructure conditions to creep-fatigue properties, and form the foundation for future modeling efforts through the development, validation, and modification of existing analytical and computational models. More specific objectives of this thesis are outlined in the following section.

1.2. Objectives

A turbine disc is commonly subjected to intermediate temperature and cyclic strain as shown in Figure 1.1, which means an understanding of the low cycle fatigue (LCF) properties of disk materials is essential. Scatter in the fatigue life of low cycle fatigue experiments is a common problem; it is speculated that this scatter may be due to factors

ranging from experimental variability when tests are performed in different locations under slightly varying conditions to underlying differences in the physical crack initiation and growth mechanisms in the material due to variations in the microstructure. Thus, this body of work focuses on two main objectives:

1) To determine which microstructural parameters have the greatest influence on the low cycle fatigue properties of a commonly used turbine disk material, Rene 88DT. Since low cycle fatigue stress and strain range are determined by the material's hardening properties, the effects of grain size as well as γ' volume fraction and size distribution on LCF lives is studied. Oxide inclusions may also be present as contaminants in very small volume fractions within the microstructure, but they may have a large influence on LCF lives because cracks area able to initiate easily around the inclusions. Thus, a careful examination of the influence of size and location of inclusions within the microstructure must be conducted.

2) To develop physically based models to predict number of cycles to failure based on the most relevant microstructural and macroscopic material parameters in the crack initiation, short crack growth, and long crack growth regimes of fatigue life.

1.3. Overview of the Thesis

The thesis is organized so that past research on crack initiation and growth mechanisms forms the basis of the understanding and new knowledge discovered in this research. Chapter 2 reviews much of the pertinent literature regarding the microstructural

development of superalloys and then discusses how previous researchers have investigated the microstructural effects on crack initiation and growth properties. Chapter 3 describes the experimental procedure designed to investigate and develop physically-based models for crack initiation and growth; the experiments include microstructural characterization and mechanical testing techniques. The results of the experiments along with analysis and discussion are presented in Chapter 4. The chapter also includes the development of models for crack initiation and growth, which were formulated based on microstructural characterization, fatigue testing, and fracture surface observations. Finally, conclusions and recommendations for future work are offered in Chapter 5.

CHAPTER 2

LITERATURE REVIEW

2.1. Microstructural Evolution in Nickel-Base Superalloys

An understanding of microstructural development is important in relating solidification, powder processing, heat treating, and microstructure to mechanical properties. The volume fraction, size distribution, and chemistry of the strengthening precipitate, γ', plays a major role in tensile strength, creep rupture, and LCF properties. Grain size can be altered to change the yield strength, low cycle fatigue, and fatigue crack growth properties of these alloys. Carbides and borides around the grain boundaries assist in strengthening the grain boundaries, but carbides can be brittle and detrimental to the mechanical properties of superalloys [7]. Ceramic inclusions from the powder processing are also present in extremely low volume fractions and are sometimes responsible for premature failure in low cycle fatigue conditions [8]. The microstructure of Rene 88DT is specifically designed to improve the damage tolerance of the alloy compared to other common turbine disk alloys such as Rene 95 [1].

All nickel-base superalloys have a cubic, austenitic matrix phase, γ, that has an fcc crystal structure. An $L1_2$-type ordered precipitate, γ' ($Ni_3(Al,Ti)$), strengthens the matrix. The volume fraction, size distribution, morphology, and location of γ' in the microstructure is influential in the development of the surrounding microstructure and in the mechanical properties of the superalloy [8]. The lattice parameters of γ and γ' are very similar, so the

matrix and the precipitates are coherent; however, coherency strain is usually not zero and it increases the amount of hardening in the alloy . In Rene 88DT, tungsten is added to increase the lattice parameter of γ, which lowers the mismatch between γ and γ' [1].

Kriege and Baris [9], in an effort to understand the formation characteristics of γ' and how it affects the surrounding microstructure, modified techniques to chemically extract γ' from a matrix so chemical analysis could be performed and lattice parameters measured. They found the amount of γ' is related not only to aluminum content but also to the presence of elements that substitute for aluminum (Ti, W, Mo, Nb, Ta, V, and C) in the alloy. They also observed that the Al/Ti ratio stays the same in the γ' and the matrix.

Typically, there is a distribution of sizes among γ' precipitates due to the nature of the heat treatments. In Rene 88DT, the size distribution is bimodal; larger γ' precipitates, which are labeled secondary γ', form upon slow cooling from the annealing temperature, and smaller "tertiary" γ'precipitates are formed upon aging at intermediate temperatures after the initial heat treatment. The size distribution of γ' and morphology of the secondary γ' is dependent on the cooling rate from the supersolvus anneal. If the cooling rate is sufficiently slow (less than 300^{o}C/minute), two sizes of secondary γ' form, the smaller of which forms at the end of the cooling process and is similar in size to tertiary γ'; to avoid confusion, the larger secondary γ' precipitate will be labeled as primary γ' throughout this document. The secondary γ' has a spherical shape at faster cooling rates and becomes cuboidal at cooling rates slower than 100^{o}C/minute; at even slower cooling rates, its morphology can become dendritic. The tertiary γ' is always spherical. The

diameter of the secondary γ' increases as the cooling rate decreases, while the diameter of the tertiary γ' is more dependent on the aging time after cooling. Never the less, a coherent interface is maintained for all sizes and shapes of γ'. Rene 88DT is damage tolerant because it has the lowest γ'/γ mismatch of any commercial alloy [10].

Mao *et al*. [11] examined the effects of heat treating on the microstructure and resulting mechanical properties in Rene 88. Two different heat treatments were used: a continuous cooling heat treatment and an interrupted cooling heat treatment; in both heat treatments, the first step was to homogenize by holding the material above the γ' supersolvus solution temperature for five minutes. Continuous cooling experiments were performed with several different linear cooling rates. In the interrupted cooling heat treatments, the specimens were cooled at a rate of 55ºC per minute until they reached a transition temperature, which was varied between the heat treatments, and then quenched to room temperature. In the continuous cooling tests, the cooling γ' shape changes from cuboidal to spherical as the cooling rate decreases; simultaneously, the cooling γ' diameter increases as the cooling rate decreases (Figure 2.1); a power-law that relates γ'diameter to cooling rate can be fitted to the data. It was also found that volume fraction decreases with increasing cooling rate but the particle density increases due to the degree of supersaturation. The yield and ultimate tensile strength both increase as a logarithmic function of cooling rate with a corresponding decrease in the mean precipitate diameter. The size of the γ' precipitates increases as the transition temperature is decreased (Figure 2.2), but the shape remains spherical for the range of transition temperatures studied; simultaneously, there is a decrease of the yield and ultimate tensile strength as the

transition temperature is decreased. Without fail, an increase in strength is correlated to decrease in the precipitate sizes in their studies.

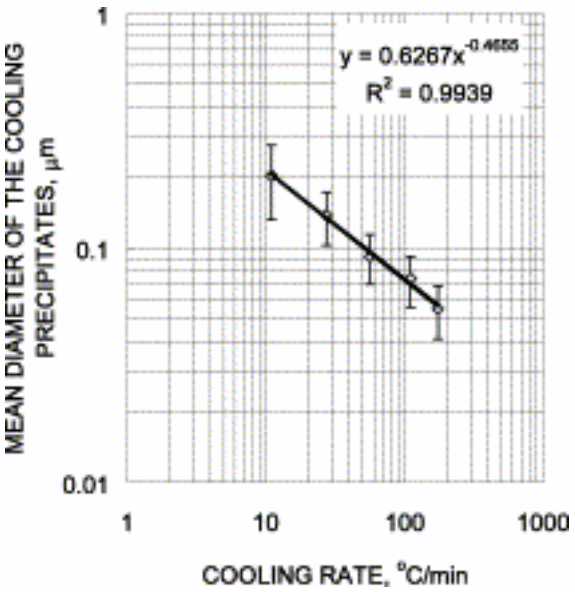

Figure 2.1. Mean diameter of cooling γ' precipitates versus cooling rate in continuous cool experiments [11].

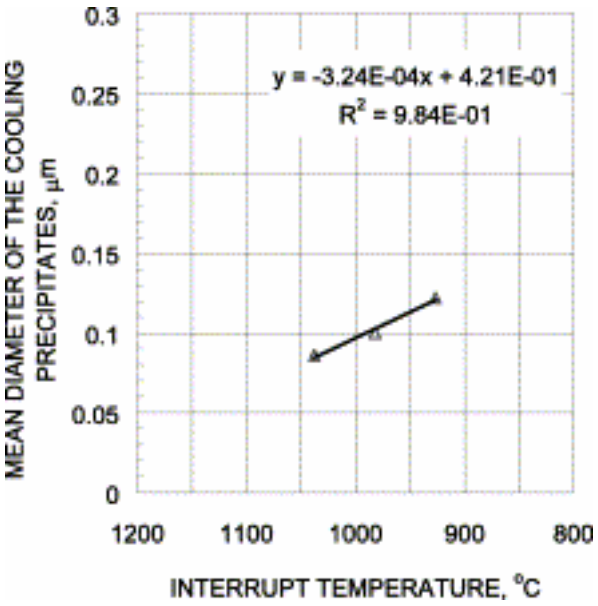

Figure 2.2. Mean diameter of cooling γ' precipitates versus transition temperature in interrupted cooling experiments [11].

As the size of γ' precipitates increases, their shape evolves due to interfacial energy and mismatch with the matrix. The γ' precipitates are present as spheroidal particles when the mismatch is between 0.5 and 1 percent and they become more cuboidal when the mismatch is greater than 1.25 percent [12]. Yeom *et al.* [13] performed isothermal heat treatments on Ni-8 Al at various temperatures and for various times to study how the γ' changed in shape from spherical to cube to octet. Their study was limited to a small temperature range with a moderate nucleation rate because they did not want the elastic interaction of the precipitates to influence their morphology. They found that the diameter values for sphere to cube and cube to octet transformation were 0.1-0.2 μm and 0.6-0.8 μm respectively. They also compared their results to the theory of Khachaturyan, Semenovskaya, and Morris [14] who predict shape and spacing between the γ' using the elastic energy around the precipitates. The results compared reasonably well to the theory except the cuboids were smaller in size than predicted. They concluded that a model that predicts the complete sequence of morphological evolution must consider a large variety of shapes and configurations. Parker and West [15] also studied how elastic strain between particles affected morphology and coarsening as well as alignment of γ'. They found that increasing the interfacial mismatch between γ and γ' increases the tendency to form cuboidal γ'. Elastic interaction between particles at short ageing times and higher mismatch values causes alignment of the precipitates. They also determined that elastic strains and particle distribution do not affect the coarsening rates of γ'.

In addition to γ' precipitates, $M_{23}C_6$ and M_6C carbides are found at grain boundaries of superalloys; the carbon combines with titanium, tantalum, hafnium, and niobium among

other elements to form the carbides, which can also be formed upon prolonged service exposure. $M_{23}C_6$ forms with moderate to high chromium content in the alloy and during lower temperature heat treatment and service. When molybdenum or tungsten is more than six to eight atomic percent, M_6C forms; M_6C is important in controlling the grain size during processing. Carbides and borides, which form when boron segregates to grain boundaries, act to strengthen the grain boundaries. The borides form as blocky, half moon shaped M_3B_2 precipitates [12]. Liu and Sommer [16] observed the solidification and growth behavior of MC carbides. Much of their research focused on directional solidification, which is not how Rene 88 is processed; but in general, they found that there are three controlling factors for carbide growth: 1) the microsegregation levels of carbide forming elements such as Ti, Nb, and C, 2) the morphology of the γ matrix because carbides grow in grain boundary regions, and 3) the solidification time. Since some of the carbon containing precipitates are brittle in nature, it is important to understand their growth kinetics and classify their size location characteristics in the microstructure.

Wlodek *et al.* [10] found several different types of carbides and borides in a Rene 88DT forging that had undergone a typical heat treatment. An MC precipitate was identified that had a significant amount of titanium and a lower amount of niobium. Also, $M_{23}C_6$ carbides formed on grain boundaries after service. They observed a tetragonal M_3B_2 phase that contained a large amount of chromium along with molybdenum and tungsten. A rare tetragonal M_5B_3 precipitate was observed that contained large amounts of Mo and

W plus Cr. The borides and carbides were all equiaxed, 0.1 to 0.5 μm in diameter, and located at grain boundaries.

Garosshen *et al.* [17] studied low temperature continuous carbide (LTCC) precipitation of $M_{23}C_6$ in a nickel base superalloy. They observed the continuous carbide to form intergranularly in the 732ºC to 760ºC (1350ºF to 1400ºF) temperature range. Since one possible decomposition reaction of MC results in the formation of $M_{23}C_6$ and M_6C, the distribution of MC influences the formation of the LTCC phase. The LTCC phase provides an easy, brittle crack propagation path, and they found that the presence of LTCC reduces the stress-rupture life of the alloy. Kotval and Hatwell [18] showed that if there is a high degree of supersaturation in the matrix of carbon, discontinuous precipitation of $M_{23}C_6$ occurs on grain boundaries. The presence of discontinuous precipitation reduces ductility at elevated temperatures, and the precipitates may be sites for crack initiation and subsequent grain boundary failure.

Table 2.1 shows the various effects of alloying elements on the properties of the superalloys. W is added to both Rene 95 and Rene 88 as a carbide former and Nb forms a fine dispersion of Nb, Ti rich precipitates in both Rene 95 and Rene 88 [19]. All of the elements listed in the table except for Ta, Fe, and Re are present in Rene 88. Note that there are a large number of elements that can form carbides and that B and Zr are present as effective inhibitors of carbide coarsening; the carbides studied in this research are approximately the same size as the primary γ'.

Table 2.1. Role of various alloying elements in determining the properties of superalloys. [7].

Element	Matrix Strengthening	Increase in γ' Volume Fraction	Grain Boundaries	Other Effects
Cr	Moderate	Moderate	$M_{23}C_6$ and M_7C_3	Improves corrosion resistance; Promotes TCP phases
Mo	High	Moderate	M_6C and MC	Increases Density
W	High	Moderate		Promotes TCP phases σ and μ (Mo, W)
Ta	High	Large		
Nb	High	Large	NbC	Promotes γ' and δ phases
Ti	Moderate	Very Large	TiC	
Al	Moderate	Very Large		Improves oxidation resistance
Fe		γ'->β, η, γ'' or δ		Decreases oxidation resistance; Promotes TCP phases σ, Laves
Co	Slight	Moderate in some alloys		Raises solidus; May raise or lower solvus
Re	Moderate			Retards Coarsening, Increases misfit
C	Moderate		Carbides	
B, Zr	Moderate			Inhibit carbide coarsening; Improve grain boundary strength; Improve creep strength and ductility

Crompton *et al.* [20] performed various heat treatments on Astroloy above and below the γ' solvus to determine how heat treating affects prior particle boundary (PPB) precipitates; PPB precipitates are generally oxide or carbide precipitates that form on the powder particle surfaces during processing. They found the size of the PPB precipitates was usually 0.02 to 0.3 μm and were either MC cubic carbides, a monoclinic ZrO_2, or an α-Al_2O_3 trigonal phase; the latter two phases are oxide particles formed during atomization of the powder. Heat treatments around the γ' solvus had little affect on the precipitation behavior of the alloy but heat treatments above the γ' solvus resulted in the dissolution and reprecipitation of M_3B_2 on the grain boundaries. They also investigated whether ZrO_2 particles acted as nucleation sites for MC carbides and found that the majority of the MC carbides existed separately from ZrO_2 particles. Like carbides, oxides are brittle and it is necessary to examine whether crack initiation can occur from the interaction of cracked oxides and carbides.

Powder processing results in impurities from contamination that can be detrimental to the mechanical properties of a superalloy. During gas atomization of the powder, there are sometimes transient air leaks in the system that generate oxide particles. Pores can form in the powders as a result of entrapped argon; they usually close during the subsequent processing but can open back up during high temperature exposure. Contamination can produce reactive defects that are also very deleterious to the alloy; they are produced from sources such as cloth, rubber, grease, human hair, and mill scale oxides and often grow during thermal processing due to precipitation of oxides and carbides around the contaminant [21]. Types of defects include: 1) metallic inclusions, 2) reactive nonmetallic inclusions, 3) nonreactive metallic inclusions, and 4) pores and voids. An effort has been made in the past several years to reduce the detrimental effect of these inclusions on LCF properties [22]. This has been accomplished by decreasing the powder particle size and thus decreasing the size of possible inclusions and also by changing processing techniques to decrease the number of inclusions mixed in with the superalloy powder. In fact, the frequency of surface initiated failures associated with inclusions during low cycle fatigue testing has significantly decreased over the past twenty years (Figure 2.3).

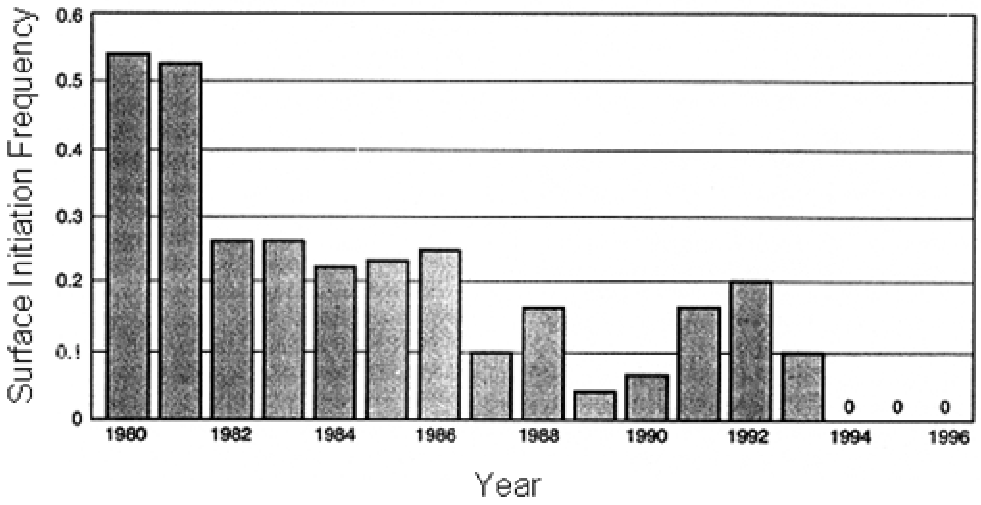

Figure 2.3. Frequency of surface initiated failure in LCF tests conducted at 540ºC (1004ºF) in strain controlled tests [22].

All of these studies demonstrate the importance of understanding the processing-structure-property relationships of superalloys because of the large number of microstructural features and processing parameters that affect strength and fatigue failure properties.

2.2. High Temperature Crack Initiation and Propagation in Nickel-Base Superalloys

The life of a superalloy part may be controlled by the number of cycles required to initiate a crack in the part, the cycles required to propagate an existing crack, or a combination of both fatigue stages. Thus, a thorough understanding of the mechanisms governing both the crack initiation and growth processes is necessary to determine the contribution of each to the total fatigue life. It is also necessary to study short crack growth mechanisms and the portion of fatigue life spent in this stage; previous researchers have combined short crack growth with both crack initiation and long crack growth parameters with varying success [2, 23-25].

2.2.1. Crack Initiation and Small Crack Growth Mechanisms in Nickel-Base Superalloys

Crack initiation in nickel base superalloys is controlled by three main factors: microstructure, temperature, and environment. Furthermore, the microstructural effects are the result of the alloy's powder and processing history because inclusions and pores in the microstructure are often the sites of crack initiation. Grains oriented favorably for slip are prone to slip band cracking and are especially detrimental on the surface. The formation of a dominant crack is primarily a competition between initiation from slip band cracking and initiation from defects such as inclusions or pores.

According to Reichman *et al*., there are four major types of defects that are found at fatigue failure initiation sites: 1) metallic inclusions, 2) reactive nonmetallic inclusions, 3) nonreactive metallic inclusions, and 4) pores and voids [22]. Contamination from the melting crucible, pouring tundish, or atomizing nozzle causes the formation of the first two types of defects. Since they are formed before screening, their maximum size is the mesh size of the powder. Aluminum is the main metallic constituent, but zirconium, magnesium, and calcium can also be present. Type 1 defects are chunky particles while type 2 defects are agglomerates of several smaller particles. Oxygen and carbon can react with a contamination source such as a piece of refractory to form a semicontinuous network of oxides or carbides around the powder surfaces, which are classified as type 3 defects. These defects are generally much larger than type 1 and 2 defects because they are not limited by the mesh size. Type 4 defects are voids formed by entrapped argon from the atomization process. They are approximately the same size as type 1 and 2 defects but can become larger when particle size increases. When these defects are

present at the surface of a part, interaction with the environment makes them more evern more detrimental [21].

Surface defects are more likely sites for crack initiation than subsurface defects in LCF experiments, but the applied strain range influences the location of crack initiation and the subsequent small crack propagation. Hyzak and Bernstein [26] identified three mechanisms of crack initiation at strain ranges above 0.7% that were frequency and temperature dependent: transgranular initiation normal to the loading direction, transgranular initiation 45 degrees to the loading direction, and intergranular cracking. The most common of the three was transgranular initiation normal to the loading direction, but there was no obvious defect associated with these initiation sites though serial sectioning through the specimen cross section exposed cracking in nonmetallic inclusions and carbides near the specimen surface; smaller pores also contributed to initiation. Transgranular cracking at a 45 degree angle to the loading axis occurred on the same fracture surfaces as the transgranular initiation normal to the surface. Intergranular cracking only occurred at 760ºC (1400ºF) and a frequency lower than 0.2 cycles per minute. Below 0.7% strain range, cracks usually initiated at nonmetallic inclusions. They conjectured that a high temperature oxide layer on the surface of a specimen could crack at large applied strain ranges, which could be one reason the initiation mechanism varies with applied strain range. The work of Gell and Leverant [27] is cited, which suggests that at low strain ranges surface oxides could fill surface cracks, preventing crack closure and crack tip resharpening, and thus, increasing the number of cycles to

failure; experiments by Hyzak and Bernstein failed to prove the hypothesis. They found that the percentage of life spent initiating a crack increases as strain range decreases.

Hyzak and Bernstein [26] also report the low cycle fatigue failures originated from the specimen surface or near surface sites above a certain transition strain range in LCF experiments; while below the transition strain range, the failure initiated at an internal defect. At larger strain ranges, cracks initiate quickly and are able to propagate more easily on the surface because of the large stress intensity associated with a surface flaw; at lower strain ranges, cracks only initiate at the defects with the highest stress intensities. The surface-subsurface transition strain range is dependent on the alloy's composition and the size and volume fraction of defects.

Chang *et al.* [19] showed that extruded and forged Rene 95 has far fewer and more dispersed defects than HIPed Rene 95; the result is an improvement in ductility and LCF properties. The Rene 88 studied in this research is processed by extrusion and forging. They also found that most of the defects at the initiation sites of LCF fracture surfaces of the extruded and forged materials were of types 1, 2, or 4; no type 3 defects were found. The size of the type 1 and 2 defects were between 0.0026 mm^2 (4 $mils^2$) and 0.0065 mm^2 (10 $mils^2$) on average. The type 4 defects were less than 0.00065 mm^2 (1 mil^2) on average. Their results for the extruded and forged material are summarized in Table 2.2.

Table 2.2. Summary of defect initiation sites on LCF fracture surfaces from extruded and forged Rene 95 [19].

			Frequency of Defect Type (%)		
Temperature (ºC)	**Δε (%)**	**No. of Surface Failures (%)**	**1**	**2**	**4**
538	0.75	37	75	25	0
538	0.75	4	38	54	8
399	0.75	15	32	39	26

Jablonski [25] intentionally doped a low carbon Astroloy powder with Al_2O_3 or SiO_2 particles at concentrations ranging from 2 to 40 ppm and compared their LCF properties to a clean Astroloy material. The particles simulate reactive and nonreactive inclusions in a powder, where reactive inclusions are reduced by elements in the alloy to form a complex nonmetallic inclusion and a reaction zone around the inclusion; for example, the silicon reacts with aluminum to form an aluminum rich inclusion with a 15 μm layer of ZrO_2 and TiO_2 surrounding it. The inclusions can either crack or debond to initiate a crack during fatigue cycling. A residual tensile stress is found around the inclusions because their coefficient of thermal expansion (CTE) is less than the CTE of the alloy; also, they have a higher modulus of elasticity than the surrounding alloy resulting in an additional stress concentration around the inclusions. He showed through surface replication of specimens performed throughout the LCF experiments that cracks can initiate from persistent slip bands. At 500ºC (932ºF), the highest testing temperature, cracks initiated when subsurface inclusions cracked in half. Cracks initiated at 25ºC (77ºF) when the matrix material debonded from the inclusions. Ceramics did not initiate fracture in the clean material or the material doped with 2 ppm SiO_2. Ceramics initiated fracture at least 50% of the time in the materials doped with 4 ppm Al_2O_3, 40 ppm Al_2O_3,

and 20 ppm SiO_2. Cracks in the SiO_2 doped material originated at granular inclusions that had been enriched by aluminum.

Using fracture mechanics, Jablonski modeled the effect of inclusions on fatigue life. Since the inclusions may crack in half at elevated temperature cycling, the inclusion was simulated by a crack of length equivalent to the diameter of the particle, d, at a distance b from the surface of a semi-infinite body. The upper limit for crack initiation can be calculated for stage I cracking assuming a crack, which initiated from a persistent slip band, is one grain diameter in length and then determine its stress intensity factor. Thus, a cracked ceramic whose diameter is less than or equal to the grain size is no more detrimental than a stage I crack originating in persistent slip bands (PSB). Figure 2.4 plots the stress intensity of an inclusion initiation site versus number of cycles to failure on a semilog graph. The plot clearly shows the number of cycles to failure decreases as the stress intensity of the most detrimental inclusion increases. The cross on Figure 2.4 represents the stress intensity for a stage I crack and the upper limit for fatigue life. The volume of material in which an inclusion must lie to cause crack initiation was determined by calculating the stress intensity factor as a function of distance from the surface of the semi-infinite body. For distances between $3d/2$ and $d/2$, the stress intensity factor increases from $(\pi d/2)^{1/2}$ to $1.59(\pi d/2)^{1/2}$, and it was determined that the inclusion with the highest stress intensity within this volume would initiate fracture. It was also assumed that any inclusion within this volume was exposed to the environment. Thus, the concentration of ceramics necessary to initiate a crack is given by

$$ppm = \frac{\rho_C}{\rho_M}\left[\frac{d^3}{6l}\left\{r_O^2 - \left(r_O - \frac{3d}{2}\right)^2\right\}^{-1}\right] \times 10^6 \qquad (2.1)$$

where ρ_c is the density of the ceramic, ρ_m is the density of the metal, l is the specimen gage length, d is the ceramic diameter, and r_o is the specimen radius. The number of ceramic particles per unit volume and the number of ceramics in the affected volume is considered in the model and simplified to equation 2.1. The equation implies that a lower concentration of less dense ceramic particles is required to initiate a crack. Furthermore, the stress intensity factor of cracked particles on the fracture surface was calculated assuming the crack length is half the inclusion diameter and taking into account the particle's distance from the specimen surface.

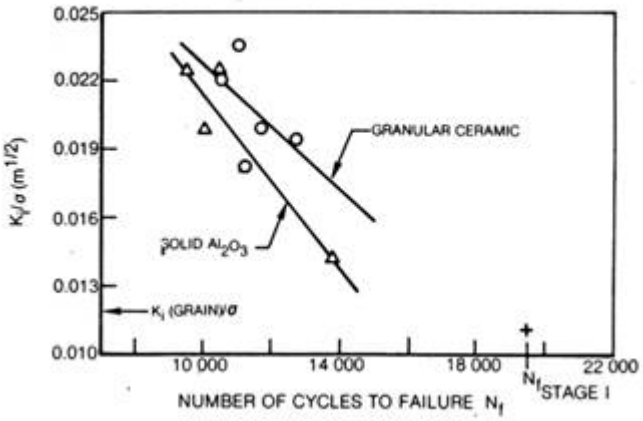

Figure 2.4. Initial normalized stress intensity at an inclusion versus number of cycles to failure for Astroloy [25].

Byrne *et al*. [28] also considered inclusions and groups of inclusions as elliptical shape cracks. Low cycle fatigue tests were conducted at 650°C on Waspaloy material with and without defects. Using ΔK_{eff} values they predicted the growth of the elliptical cracks cycle by cycle until the crack length reached a critical value; while their predictions were

close for both surface and subsurface inclusion clusters, they were all slightly conservative (Figures 2.5 and 2.6).

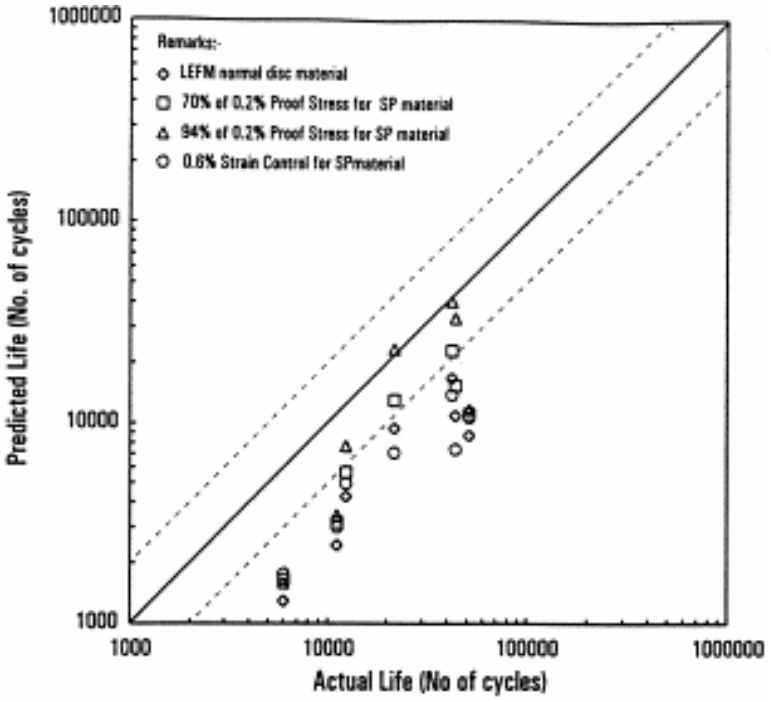

Figure 2.5. Comparison of predicted and actual lives based on ΔK_{eff} for semielliptic cracks on the surface [28].

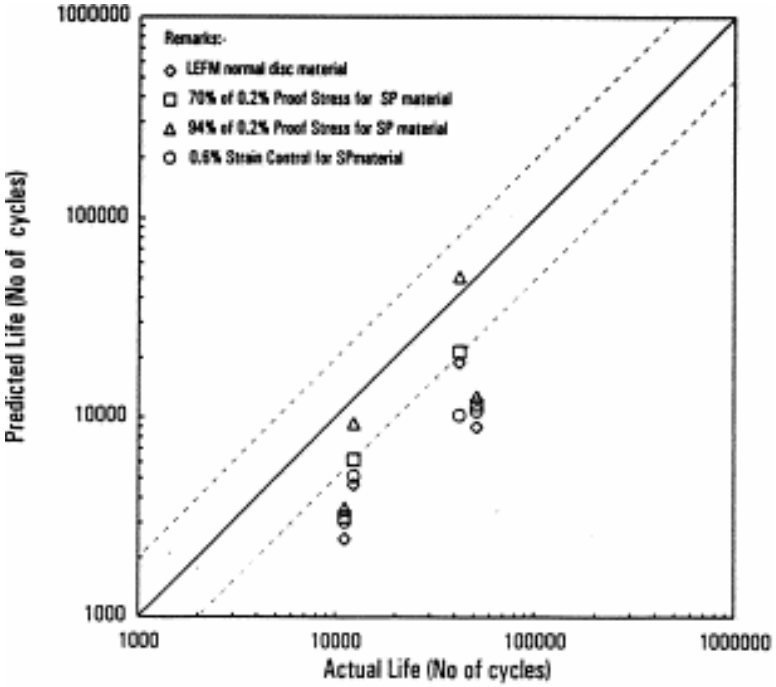

Figure 2.6. Comparison of predicted and actual lives based on ΔK_{eff} for elliptic cracks in the subsurface [28].

Miner and Dreshfield [29] examined the affect of pores on crack initiation and growth. They cited two possible mechanisms for producing pores in the microstructure: atomization producing hollow particles filled with argon and lack of complete evacuation of argon gas from a powder container before consolidation. Leaks in the powder container can also allow penetration of argon gas and result in pores in the material. They produced an excess of pores in Astroloy for their research, roughly fifteen times manufacturer's specifications. They discovered that cracks in the porous material initiated at single sites in the area of closely spaced pores; initiation at small pores (< 5μm) did not significantly reduce life, but a single 25 μm pore did.

Luo *et al*. [30] approached the initiation of a crack on the surface of Udimet 720 four point bend specimens using probability theory. The four point bend tests were performed at room temperature using stress range values from just below the yield stress of the material to well above the yield stress. They discovered that defects and pores in the material were the most likely sites for crack initiation but pores usually initiated the dominant crack because they have sharp corners. At low values of applied stress range, several of the initiation sites were unexplained by inclusions and pores; they may have ignored the possibility of crack initiation due to plastic damage accumulation within a slip band. Since they lacked a viable small crack growth law, they used a Paris-Erdogan law for small crack growth and based the constants on experimentally determined log-normal distributions.

Miner and Gayda [31] studied the influence of grain size on the low cycle fatigue behavior in Rene 95 that had been extruded and forged, HIPed, or cast and wrought. The extruded and forged and HIPed material had average grain sizes that were five and eight microns respectively, while the cast and wrought material had an average grain size of 150 microns. The number of cycles to failure for the cast and wrought low cycle fatigue specimens fall well below the cycles to failure for specimens from the other two processing conditions for every applied strain range at 540ºC. The disparity in low cycle fatigue lives between the three processing conditions is largely due to differences in strength and ductility based on the grain size produced during processing [31].

The volume fraction of inclusions and pores in the microstructure is very small and therefore, the probability of the presence of a critically sized inclusion, pore, or inclusion cluster within a critical area of the microstructure is low. Because of this low probability, slip band cracking along grains oriented favorably for slip must be considered as a competing crack initiation mechanism. Boyd-Lee and King [23] performed four point bend fatigue tests on AP1 superalloy at room temperature and found that cracks initiated either from intense dislocation activity in mode II slip bands and twin boundaries or from brittle titanium carbides; the majority of the initiation facets formed from intense dislocation activity were associated with twin boundaries. The maximum shear stress is on planes oriented 45º to the tensile axis, which means dislocation activity will be heaviest on those planes. Experimentally, Boyd-Lee and King observed that the peak of the orientation distribution of surface facets resided at approximately 40º. There are two extreme conditions shown in Figure 2.7 for nucleation from an appropriately oriented grain; they concluded experimentally that nucleation is more likely to occur in the manner shown in schematic (a). Once a crack forms on the surface, it grows in a semicircular manner due to the ΔK variation around the crack front; for short cracks, ΔK is very dependent on orientation of the grain adjacent to the crack tip and both mode I and II values of stress intensity are important. They asserted that the uniformity of γ' can influence slip band initiation and thus fatigue cracking; a uniform distribution of γ' means there are no weak spots within the microstructure where a lower resolved shear stress is required to form a slip band. After slip band crack formation, the crack becomes important to fatigue life only if it can grow into surrounding grains; high angle grain boundaries arrest cracks because they retard dislocation activity. Once the stresses

around the slip bands exceed the bond strength of the material, a ligament of the material unzips and a crack initiates or grows further into the microstructure.

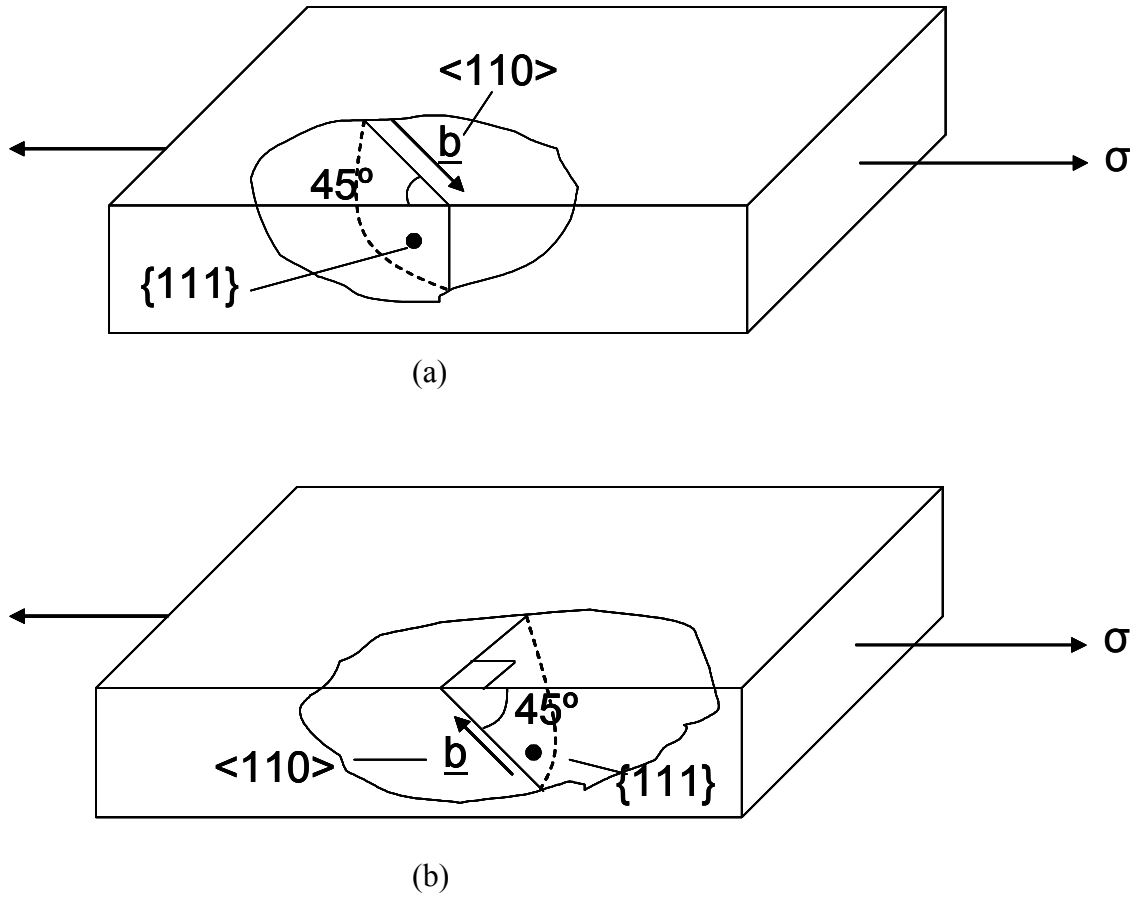

Figure 2.7. Slip band crack initiation mechanisms for an FCC material in response to a tensile force [23].

In subsequent work [24], Boyd-Lee conducted four point bend high cycle fatigue tests on Waspaloy and found that slip band initiation was much more likely than initiation from TiC precipitates and the associated lives are also 1-8 times longer. It was also discovered that the short crack area around the initiation site is faceted if the size of the plastic zone is small compared to the grain size; otherwise, the short crack region is striated. In a

statistical analysis of number of crack arrests and fatigue crack growth in the short fatigue crack regime, she found that irregular and high angle boundaries were the most effective crack arrest locations. In follow-up work [32], Boyd-Lee and King developed a statistically based model for short fatigue crack growth using the probability of four independent events occurring on any crack front: a) a proportion of the cracks continue to be arrested, b) the proportion of those arrested become free and grow during the next increment, c) cracks that grow do so according to the determined distribution, d) a proportion of the growing cracks will become arrested by the end of the increment. The predictions from their model agree well with the experimental fatigue data on Waspaloy.

Healy *et al*. [33, 34] performed short fatigue crack growth tests in Waspalloy at room temperature and at 500°C with R = -1 and R = 0.1. Cracks primarily initiated in large grains and at 30 to 60 degrees from the tensile axis, and so it was concluded that the cracks may be initiating on <110> slip systems. The subsequent short fatigue crack growth mechanisms seemed very dependent on grain orientation and R; a fairly flat, facetted fracture surface was observed at both temperatures for initiation in the vicinity of grains with similar orientation and/or for specimens tested with R = -1. Limited measurement of crack growth rates versus ΔK showed that crack growth rate is too dependent on neighboring grain orientation in the short crack regime for ΔK to be an effective characterizing parameter.

Albrecht [35] performed LCF experiments on Udimet 720 LI with varying grain sizes at 600°C and with σ_{max} values well above the material's yield stress. Because of the large

applied stress range, the grain size had little influence on the microcrack propagation rate possibly because the stress concentration in front of the crack tip was very large; thus, grain boundaries were relatively weak barriers because there were a large number of slip systems available to help propagate the microcrack due to the large stress concentration. Variation of the γ' size distribution between the different microstructures tested had little influence on LCF lives.

Alexandre *et al*. [36] also studied how grain size affects crack initiation mechanisms in different heat treatments of Inconel 718. The grain size in the materials tested ranged from 5 to 150 μm, and the tests were conducted at 600°C with applied strain ranges between 0.7% and 1.7%. In the small grain size material, the initiation sites were consistently associated with second phase particle cracking; however, in the largest grain size material, crack initiation was purely from intense slip bands. The initiation mechanism in the 40 μm grain size material was found to be dependent on the grain size; for small grains, particle cracking is more likely to cause crack initiation while slip band cracking is more likely for large grain materials. Fatigue initiation life can then be predicted by using a proportionality law that predicts cycles to initiate a crack based on grain size or by predicting the crack growth rate for small particle cracks less than the grain size. Subsequently, the crack growth rate law can be used to predict the cycles to failure from a grain size crack to a critical size crack. The model does not consider a distribution of particle size or interaction of short fatigue cracks.

Bennett and McDowell [37] computationally simulated the fatigue characteristics of a polycrystalline material similar to 4340 steel to determine the likelihood of finding grains oriented favorably to form a slip band crack. The distribution as a function of stress state and stress amplitude of three fatigue crack initiation parameters (FIPs) was analyzed. The parameters compared are the normalized cyclic microplasticity parameter, the Fatemi-Socie multiaxial fatigue parameter, and the Mohr-Coulomb parameter; the latter two parameters contain a term that accounts for the normal or hydrostatic stress applied to the initiated crack, and thus, incorporate a measure of driving force for the propagation of the small crack. The Fatemi-Socie parameter seems to be the best fit to experimental data, and its distribution suggests that a larger number of grains have a high value of the parameter than the other two distributions. The FIPs were then incorporated with elastic-plastic fracture mechanics to form a small crack propagation law.

Most of the studies described in this section on crack initiation in superalloys imply there are two main crack initiation mechanisms and they attempt to determine the conditions where each mechanism becomes dominant. The divergence of crack initiation mechanisms in Rene 88DT was recently studied by Caton *et al* [2]. They performed fatigue tests at 593ºC and at various stress levels (σ_{max}). Analysis of the fracture surfaces indicated that the critical cracks initiated in the subsurface of the specimens except for one test with σ_{max} equal to 1400 MPa. A possible explanation for this is that the tests were all conducted below the transition strain range defined by Hyzak and Bernstein [26]. It was discovered that the variability in fatigue life increased as the applied stress level decreased. The probability of failure for tests conducted at various stress levels is plotted

in Figure 2.8. The slope of the function decreases as stress level decreases indicating greater variability at lower stress levels; also, there is seemingly a step function for σ_{max} equal to 940 MPa which may imply a divergence of initiation mechanisms at this stress level. Analysis of the fracture surfaces showed that the crack initiation derived from either a subsurface inclusion or more likely, from a crystallographic facet. An S-N plot is shown in Figure 2.9 that distinguishes between initiation from an inclusion and initiation from a crystallographic facet. It shows that the number of cycles to failure diverges to a greater extent at low stress levels for the two different initiation mechanisms.

As a followup to the LCF analysis, Caton *el al*. used Newman and Raju's solution for an elliptical crack in a square bar to estimate fatigue lives based on the starting crack sizes observed on the fatigue fracture surfaces. The analysis predicted small variability in the crack growth lives and very conservative predictions of fatigue life; thus, the authors assert that the variability in fatigue life is not due to crack growth mechanisms. A similar analysis will be presented later in this study with similar conclusions based on a linear elastic and J-integral analysis of subsurface and surface cracks originating from different crack initiation mechanisms.

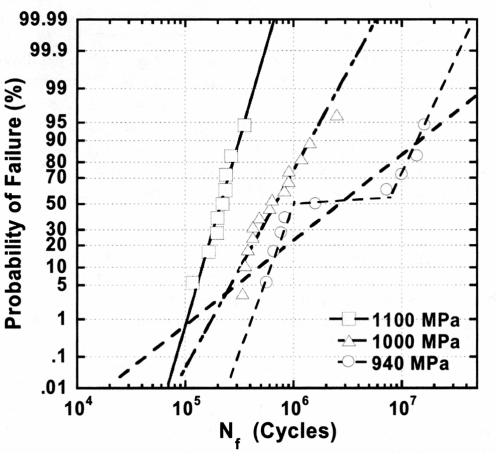

Figure 2.8. Probability of failure based on low cycle fatigue results performed at 593ºC and at various stress levels [2].

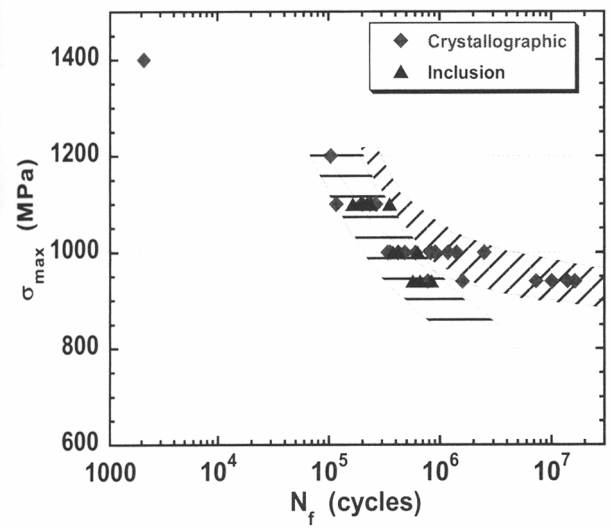

Figure 2.9. σ_{max}-N curve showing a divergence of crack initiation mechanisms [2].

2.2.2. Long Fatigue Crack Propagation Mechanisms for Nickel-Base Superalloys

The influence of microstructure and temperature is important to consider in the mechanisms of crack growth. Often, these factors are interrelated and their individual contributions to crack growth cannot be separated. It has been shown that crack growth rates become more dependent on microstructure as temperature increases [8]. Figure

2.10 shows that for several nickel base superalloys the scatter band of da/dN versus 10^3/T at $\Delta K = 33$ MPa*$m^{1/2}$ broadens as temperature increases and the crack growth rate becomes controlled by time-dependent factors and microstructure. The fatigue crack growth rates of nickel base superalloys fall into one scatter band at intermediate temperatures.

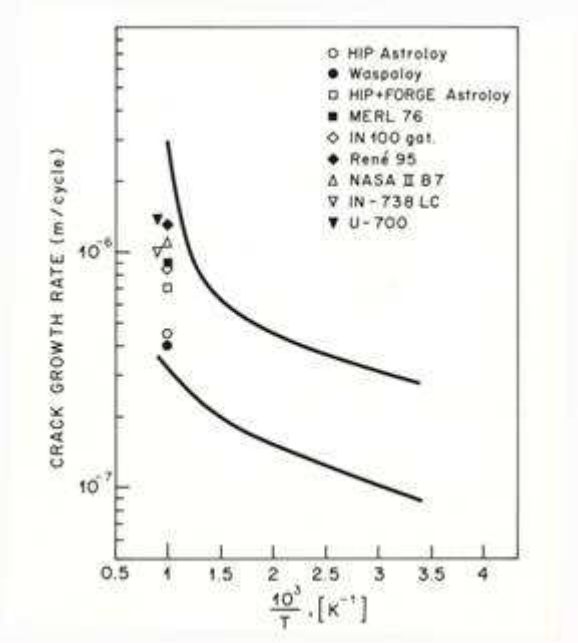

Figure 2.10. Plot of da/dN versus 10^3/T at $\Delta K = 33$ MPa*$m^{1/2}$ for several nickel base superalloys [8].

The volume fraction and size distribution of γ' can be altered to achieve strength or ductility requirements in nickel base superalloys. The precipitates can also influence crack growth due to their interaction with dislocations. Antolovich [38] varied γ-γ' mismatch, anti-phase boundary energy (APBE), and volume fraction and performed fatigue crack growth tests to determine the effect of each on fatigue crack propagation rates. Alloys with low mismatch values, APBE, and volume fraction exhibited lower fatigue propagation rates. If the imposed plastic strain is more easily accommodated

during a fatigue crack growth test, then there is less damage accumulation and fatigue crack growth is slower as a result. A high mismatch value inhibits dislocation movement and forces them to bypass the precipitate; the number of dislocation tangles then increases and damage accumulates quickly. Similarly, a high APBE keeps the dislocations from moving through a precipitate and dislocations pileup and tangle around the precipitates. If there is a low volume fraction of precipitates, there is a larger mean free path between the precipitates and dislocation movement is easier; thus, the imposed plastic strain is accommodated more easily. Figure 2.11 shows how da/dN is affected by mismatch, APBE, and volume fraction.

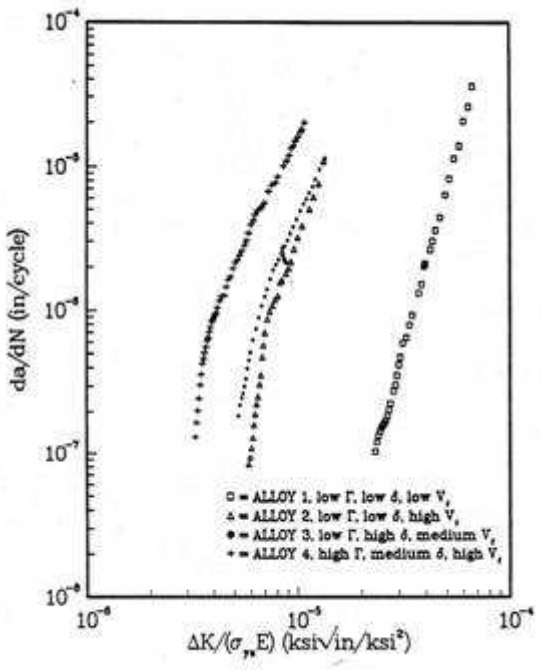

Figure 2.11. Crack growth rate versus ΔK normalized by yield strength and Young's modulus for alloys with different values of mismatch (δ), APBE (Γ), and V_v γ' [38].

Dennison *et al.* [39] studied the creep and fracture behavior of cast IN100. They performed creep tests, where several of the tests were interrupted, so the specimen could be annealed and the original γ' size distribution attained. By doing this, they negated the effects of γ' coarsening on the creep deformation and subsequent fracture mechanism of the specimen. Since deformation behavior of the alloy can be correlated to time to fracture, anything that minimizes the deformation behavior is beneficial to the life of the specimen. Increasing the size and spacing between γ' particles accelerates the creep rate, so the annealing process used caused the crack propagation rate to be associated with the original particle size distribution instead of the higher rate observed for coarser particles.

Miner and Gayda [31] conducted fatigue crack propagation (FCP) tests on HIP and extruded and forged powder metallurgy (P/M) Rene 95 and on cast and wrought (C&W) Rene 95 in order to determine the affect of grain size on crack propagation rates. The HIP and extruded and forged P/M alloys had very fine grain sizes, while the grain size for the C&W product was relatively coarse. At low values of applied ΔK, cracks grew slower in the C&W alloy than in the fine-grained P/M alloys. A fine grain size is conducive to intergranular crack growth due to oxidation of the grain boundaries, so its FCP resistance is lower. Intergranular fracture was the dominant mechanism in the P/M alloys, but transgranular failure was dominant in the C&W alloy.

The combined effects of the environment and grain boundary diffusion during high temperature fatigue cracking were addressed by Floreen [40]. Air and sulfur environments were found to increase the rates of creep and creep fatigue cracking compared to tests performed in a vacuum or in an inert environment. One possible

reason for the detrimental influence of the environment is that the active element in the environment diffuses into grain boundaries ahead of the crack tip. Then, oxygen may form CO bubbles with the carbon from grain boundary carbides. Oxygen and oxides may suppress grain boundary sliding, so it is more difficult to relieve local stresses during creep. If carbides and γ' are oxidized intergranularly or intragranularly, bonds between the particles can be destroyed, creating cavities in the material. Boron can be added to the material to reduce the effects of environment on the grain boundaries.

Pineau [27] summarized observations of the influence of metallurgical factors and oxidation on fracture mechanisms of superalloys in fatigue crack growth. The frequency of FCG tests conducted on Inconel 718 was varied and it was discovered that a transition from intergranular fracture to transgranular fracture occurred as test frequency increased. It was found that at low testing frequencies in alloy 718, the fatigue crack growth rate is inversely proportional to frequency, which implies time-dependent behavior. At high frequencies, the crack growth rates are independent of frequency. Microstructure and environment have a much larger effect at low frequencies at 650ºC (1200ºF) when time dependent behavior is dominant; for example, lower rates of crack growth correspond to larger grain sizes.

It was also discovered that crack growth rates decrease with an increase in γ' size in both the bulk and the skin microstructures of alloy N18 [41]. At lower frequencies, the environment, specifically oxidation, is very active at the crack tip in both short and long range diffusion processes. In the short range process, an oxide layer forms at the crack

tip and may eventually form a wedge shaped inclusion that results in high stresses at the crack tip. The wedges can also rupture, accelerating intergranular growth rate. Oxygen uses short circuit paths such as grain boundaries and slip bands in the long range diffusion process, and internal oxide sites, cavities, or solute segregations can form.

Kang *et al.* [42] researched how oxide formation relates to the crack propagation process in IN718. They found a niobium oxide grain boundary film on fracture surfaces of creep crack growth tests performed at 650ºC (1200ºF) and speculated that the film may have derived from the formation of niobium oxides from NbC particles at the grain boundaries. Also, the δ phase (Ni_3Nb) precipitates at the grain boundaries, which may also form oxide particles. They suggested that high stresses around the crack tip accelerate the driving forces for diffusion of oxygen and niobium along the grain boundaries, which then react with each other to form brittle niobium oxides and oxide layers on the grain boundaries.

2.3. Literature Review Summary

The processing conditions of superalloys, including Rene 88DT, are very pertinent to the alloys' microstructural development and resulting mechanical properties. Specifically, γ' characteristics, including volume fraction and size distribution, can strongly influence mechanical properties such as strength, creep resistance, and crack growth. The grain size has also been shown to have an effect on the rate of crack growth and crack growth mechanisms. Defects, such as oxide inclusions, are often found in superalloys that have undergone powder metallurgy processing; these defects have a deleterious effect on

fatigue life because they are natural sites for crack nucleation. Slip band cracking has also been observed as another dominant crack initiation mechanism. Researchers have investigated mechanisms of short crack growth after crack initiation and studied environmental, microstructural, and grain orientation effects. The rest of this thesis will be dedicated to exploring methods to study crack initiation, short crack growth, and long crack growth mechanisms. Models, based on observations, will be developed to predict fatigue life based on the underlying physical mechanisms of each fatigue stage of fatigue.

CHAPTER 3

EXPERIMENTAL PROCEDURE

3.1 Material

Rene 88DT was developed by General Electric Aircraft Engines in 1988 because of the need for an improved turbine disk material [1]. The microstructure and composition was tailored so that it has improved fatigue crack growth rates and creep strength compared to Rene 95 with less than a 10% reduction in ultimate tensile strength compared to Rene 95. Table 3.1 shows the approximate composition of Rene 88; one significant alteration from Rene 95 is a larger Ti/Al ratio in Rene 88.

Table 3.1. Chemical composition of Rene 88DT. Values are in weight percent.

Co	Cr	Mo	W	Al	Ti	Nb	B	C	Zr	Ni
13	16	4	4	2.1	3.7	0.7	0.015	0.03	0.03	Balance

Three bore drop samples of Rene 88 were received from General Electric Aircraft Engines for testing and their chemical composition is shown in Table 3.1. Bore drops are material removed from the central region of the disk to form a bore in the center of the disk that then connects the disk to the rotor hub. Thus, bore drops are cylindrical in shape with a diameter of approximately 150 mm and a length equal to the thickness dimension of the disk, approximately 100 mm. The bore drop material is heat treated with the disk but due to very different thermal masses, the temperature profile of the disk and bore drops are not the same. Heat treatments based on procedures from literature [43] were attempted to generate different γ' size distributions and designations described here

(Table 3.2) are used in this document to represent the heat treatments. The heat treatment procedure was not completely successful in its implementation, which will be described in the results chapter section on microstructural characterization.

Table 3.2. Description of the heat treatments performed on the bore drop material.

	First Step Cooling Rate	Second Step Cooling Rate	Transition Temperature	Aging Temperature
N	30 F/minute	350 F/minute	1900 F	1400 F
O	7 F/minute	350 F/minute	2000 F	1400 F
P	As-received from GE			

3.2 Microstructural Characterization

The desired structure-property relationships for fatigue crack initiation and growth are obtained by performing careful analysis and characterization of various microstructural features in conjunction with the mechanical tests. The potentially important microstructural parameters include grain size and distribution, γ' volume fraction and size distribution, inclusion and pore size distribution and volume fraction, and carbide size distribution and volume fraction.

3.2.1 Grain Size Determination

The LCF life of a superalloy has a strong dependence on grain size [19, 36]; thus, careful measurement and consideration of the grain size is important in understanding the microstructural influence in the crack initiation and growth processes. The bore drop material was ground to 800-1200 grit using silicon carbide paper and then polished with 6

μm and 1 μm diamond suspension; the final polishing step was performed using colloidal silica. The specimens were etched using 95 parts HCl + 3 parts H_2O_2 + 2 parts HNO_3 and a systematic sampling of images was acquired from the specimens using a Leica optical microscope and Image Pro acquisition software. The grain size was measured by manual intercept counts, which were performed until the running average and standard deviation of the grain size reached a constant value.

3.2.2 γ' Precipitate Volume Fraction and Size Distribution

To characterize the γ' precipitates, the specimens were ground and polished in a similar manner to that used for the grain size measurements. Two different etchants were used that preferentially attack γ' precipitates: Walker's etch which consists of 50 ml HCL + 10 ml H_2PO_3 + 10 ml HF + 30 ml HNO_3 + 50 ml H_20 + 20 ml $CHCO_2H$ + 15g FeCl and a glycerol based etch which consists of 3 parts glycerol + 3 parts HCl + 1 part HNO_3 + 1 part HF. Systematic sampling of images and montages were acquired in a LEO 1530 Thermally-Assisted Field Emission SEM, which permitted the acquisition of very high resolution images to characterize the primary γ'. KS400 software was used to transform the images into binary images and then to calculate the γ' volume fraction and 2-D size distribution based on image pixel counts. The tertiary γ' could be resolved in the SEM images but not well enough to accurately obtain sizes and volume fractions. The objective of the heat treatments was to produce a larges difference in the primary γ' size distribution, so an accurate characterization of the primary γ' distribution is more crucial than characterizing the tertiary γ' size distribution. The software was also used to obtain

the center of gravity of each precipitate so the first nearest neighbor distribution could be obtained.

3.2.3. Carbide Characterization Methods

In the early stages of this research, it was thought that carbides may play a major role in crack initiation and growth processes. Though carbides are useful in enhancing the creep resistance of nickel-base superalloys, there are some carbide phases that are very brittle in nature [7]. Combined with their affinity to heterogeneously nucleate on grain boundaries, which are also susceptible to crack nucleation and growth, a study of carbides within the microstructure was undertaken to ascertain their essential microstructural parameters and importance in the crack initiation and growth process. A disector probe method was developed to quantify the number of carbides per unit volume and grain boundary carbides per unit volume; several other descriptive microstructural parameters may be extracted from these quantities using stereological relationships.

A series of stacked images was received of fine-grained, subsolvus IN100. The composition of IN100 is listed in Table 3.3. It is expected that $M_{23}C_6$ and MC are the most prominent carbide types within this microstructure.

Table 3.3 Nominal composition of IN100.

C	Cr	Co	Ti	Al	Mo	B	Zr	V	Ni
0.18	10	15	4.5	5.5	3	0.014	0.06	1	balance

The images were obtained using a dual-beam focused ion beam (FIB), where an ion beam erodes away a layer of specified thickness and an electron beam is used to image the new

surface. There are 268 total images in the stack, and there are 100 nanometers between each image.

D.C. Sterio developed a procedure using the disector probe, a planar and unbiased counting frame of known area, A (Figure 3.1), for the unbiased estimation of the number and size of particles. The probe is placed in the same location on parallel planes which are a known distance apart. The distance between planes, h, must be less than the height of any particle perpendicular to the planes of the disector to obtain a completely unbiased result. Then, the number of particles that are present within the probe in the first plane but not present in the second plane, Q^+, and the number of particles that are present within the probe in the second plane but not in the first plane, Q^-, are counted. Any particle which intersects one of the solid edges of the probe is excluded from the count. Then, the number of particles per unit volume can be calculated.

$$N_v = \frac{\left(Q^+ + Q^-\right)}{2Ah} \tag{3.1}$$

In this study, the method was used to determine both the total number of carbides per unit volume and the number of carbides per unit volume that lie on a grain boundary. An example of the disector probe applied to the IN100 images is shown in Figure 3.2.

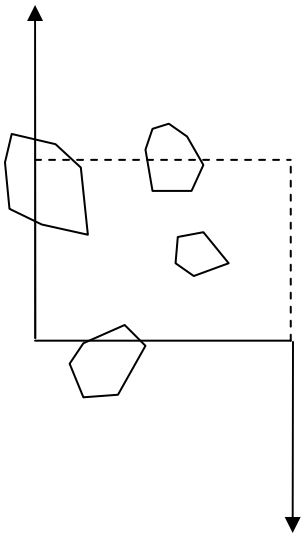

Figure 3.1. Schematic of the disector probe. Any particle that lies at least partially within the rectangular area is counted if it does not intersect a solid line and if it is not present on the other plane used for analysis.

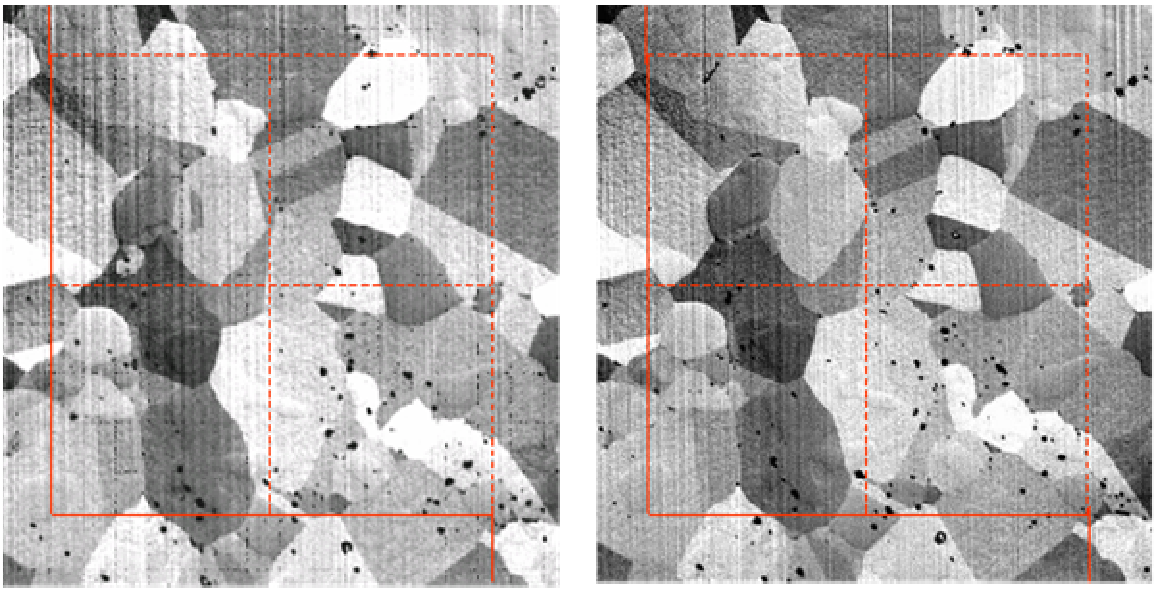

Figure 3.2. Disector probe applied to images 4 and 5 of the IN100 stack.

Pairs of images were analyzed with the disector probe with the goal that the standard deviation and average of the total number of carbides per unit volume, grain boundary

carbides per unit volume, and ratio of the grain boundary carbides to total carbides reach a plateau when plotted versus the number of pairs of images analyzed. A plateau in the plot would indicate that the average value obtained is not going to change with any statistical significance by analyzing additional fields of view. The series of stacked images was analyzed systematically by choosing pairs of images that were approximately 1000 nm apart.

The total number of carbides, the number of carbides that lie on the grain boundaries, and the ratio of the number of carbides that lie on the grain boundaries to the total was calculated using the disector method. However, when the standard deviation and average are plotted against number of fields of view for the total number of carbides and the number of carbides that lie on grain boundaries, a plateau is never attained (Figure 3.3). The carbides may be distributed non-uniformly throughout the microstructure, which could affect the standard deviation. However, the standard deviation of the ratio of the number of grain boundary carbides to the total number of carbides is low, approximately 10% of the average value. A summary of the data obtained from the disector probe method is tabulated in Table 3.4. The high ratio of the number of grain boundary carbides to the total number of carbides suggests the carbides do have an affinity for the grain boundaries in their nucleation and growth histories.

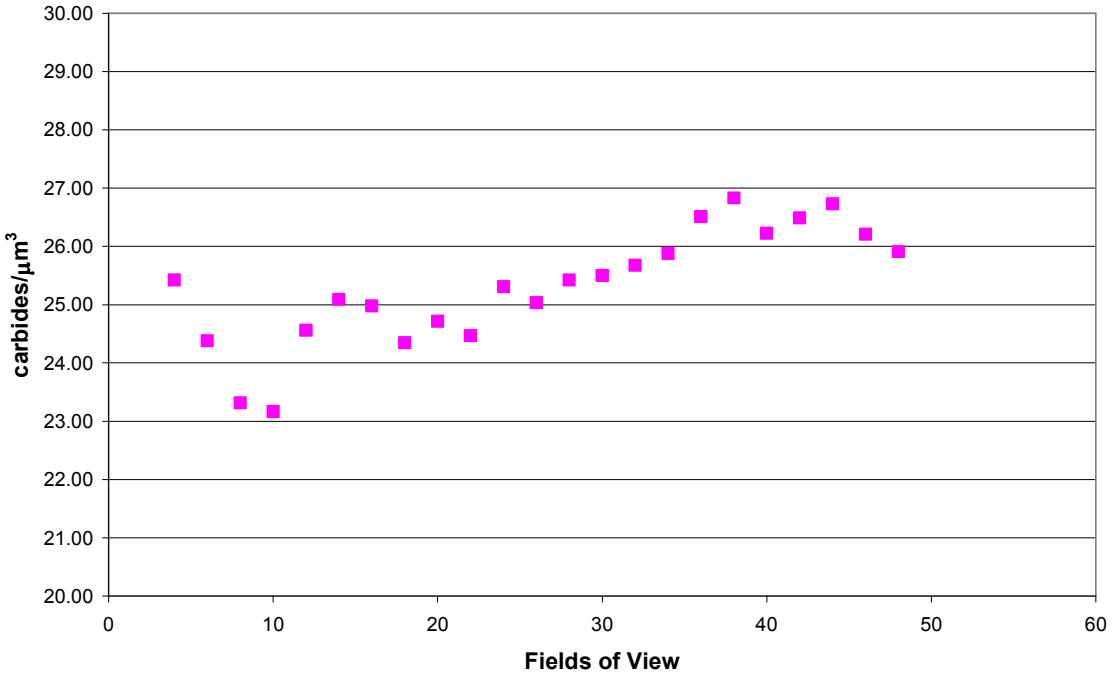

Figure 3.3. The running average of the total number of carbides per unit volume plotted against fields of view.

Table 3.4. Total and grain boundary carbide number per unit volume averages and standard deviations.

Total Number of Carbides per Unit Volume	Standard Deviation	Number of Grain Boundary Carbides per Unit Volume	Standard Deviation	Grain Boundary Carbides/Total Carbides	Standard Deviation
26/μm^3	+/- 6.2/μm^3	11.7/μm^3	+/- 2.9/μm^3	0.45	+/- 0.044

Additional calculations were performed to determine the volume fraction of carbides, the surface area per unit volume of the grain boundaries, the surface area per unit volume of the carbide/matrix interfaces, and the surface area per unit volume of the carbide/carbide interfaces. The results are tabulated in Table 3.5. There are large standard deviations in several of the measurements, which may be attributable to the low volume fraction of the carbides.

Table 3.5. Tabulated data on the carbide stereological parameters.

Volume Fraction	Standard Deviation	Surface Area/Unit Volume Grain Boundary	Standard Deviation	Surface Area/Unit Volume Carbide/Matrix	Standard Deviation	Surface Area/Unit Volume Carbide/Carbide	Standard Deviation
0.035	+/- 0.015	2.76/μm^3	0.43/μm^3	1.69/μm^3	0.61/μm^3	0.14/μm^3	0.1/μm^3

From the microstructural features quantified, several parameters can be calculated. Using the volume fraction and the total number per volume of carbides, the average volume of the carbides is determined to be 0.0014 μm^3. Knowing the number of carbides per unit volume on the grain boundaries and the surface area per unit volume of the grains, the number of carbides per surface area of grain boundary is calculated to be 4.24/μm^3. The contiguity of the carbides can be calculated knowing the surface area per unit volume of the carbide/matrix interface and the carbide/carbide interface using the following equation:

$$C = \frac{2[S_v]_{carbide/carbide}}{2[S_v]_{carbide/carbide} + [S_v]_{carbide/matrix}} \tag{3.2}$$

In this case, C = 0.14, which means that 14% of the total carbide surface area is touching another carbide, implying the carbides have some affinity for nucleating and growing on each other.

The surface area average diameter of the carbides can be calculated using the volume fraction of the carbides and surface area per unit volume of the carbide/matrix interface. The average diameter is calculated to be 124 nm, a result that brings the validity of the disector method applied to these stacked images into question. Since the images are space 100 nm apart and the size of the smallest particle is likely smaller than 100 nm,

some of the particles between successive images will be missed. Additionally, some of the carbides that are counted in one field of view and lie close to the grain boundary may actually touch a grain boundary above or below the field of view being analyzed; in order to account for this, the fields of view immediately surrounding the pair of images used for the disector method must be examined to determine if an intragranular carbide on one image actually touches a grain boundary in a vertically adjacent image. An accurate three-dimensional profile of the carbide cannot be obtained with 100 nm sections, making it often unclear whether a carbide touches a grain boundary above or below the field of view being analyzed. Therefore, the disector method applied to these images is not completely accurate and would be more valid if the images were spaced 10-20 nm apart, less than the diameter of the smallest particle.

Similar measurements to those obtained for the γ' precipitates were obtained for the carbides and borides using planar images and KS400 software. Because carbides and borides are on a sub-micron scale, montages of SEM images for each microstructural condition were created to quantify aspects of the particles. To highlight the carbides within the microstructure, methods were employed to transform all the carbide pixels into white and the rest of the microstructure pixels black; then, the carbide distribution on two dimensional sections could be observed and the relevant size dimensions of the carbides characterized. The etching characteristics of the P condition were different than for the N and O conditions, and it was difficult to obtain the same contrast between the carbides and the matrix rendering the acquisition of carbide size and shape data difficult in the P

condition. The observed carbides in the P condition were approximately of the same size and shape as those observed in the N and O conditions.

Carbides were not observed in significant area fractions on the fracture surfaces of low cycle fatigue specimens, so they were not considered as microstructural features that strongly affect the crack initiation and growth in the N, O, and P conditions. Their quantification could be important for other strength properties such as creep resistance, which was not addressed in this study.

3.3. Mechanical Testing

All of the mechanical testing was oriented towards the goal of predicting fatigue life of Rene 88 at an elevated temperature (649°C) under mode I loading starting from the initiation of a crack, progressing to short and long crack growth, and finally reaching a critical crack size for failure. Microstructural characterization was concurrently performed to develop structure-property relationships for the crack initiation and growth process. The mechanical tests were conducted at Georgia Tech and the University of Arkansas on two microstructural conditions and data for a third microstructure was made available by GEAE.

Schematics displaying how specimens were obtained from the bore drop material are shown in Figures 3.4 and 3.5. The bore drop was cut into slabs slightly larger than 1.27 cm (0.5 inches), which were heat treated according to the previously described

conditions. Then, Metcut Research Inc. machined specimens of chosen geometry and size from the slabs.

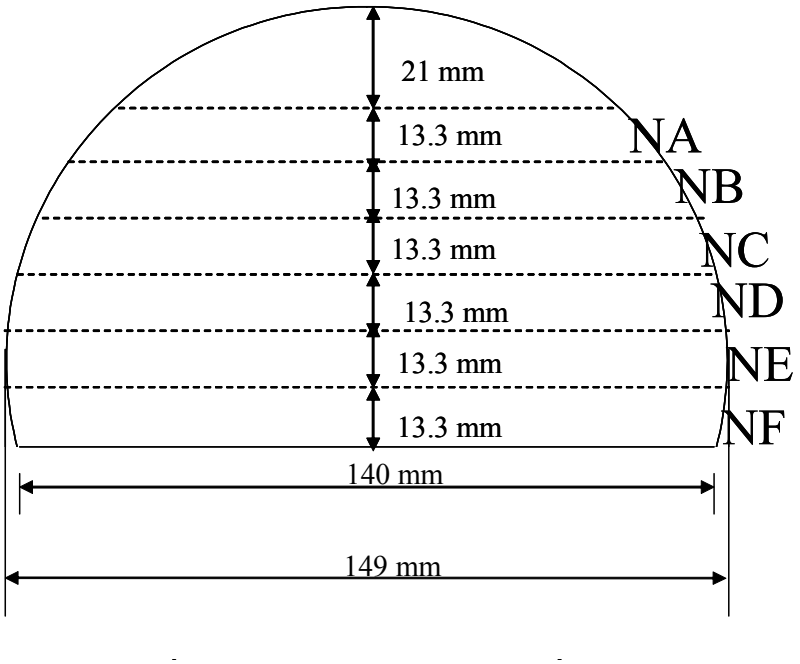

Figure 3.4. Top view of a bore drop received from GE showing how it was divided into slabs for heat treatment and specimen machining.

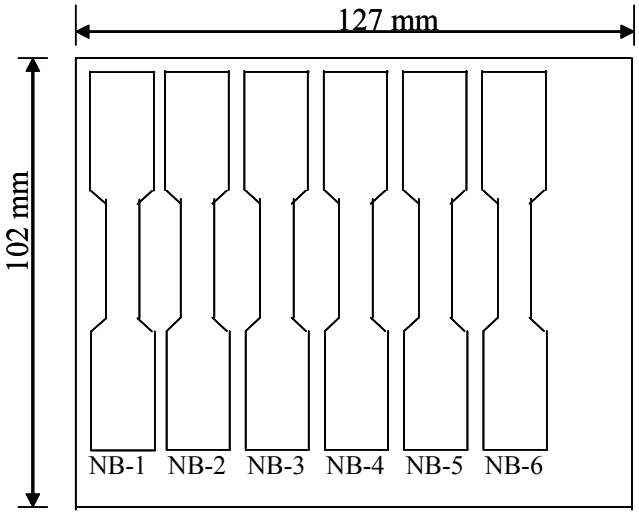

Figure 3.5. Side view of a bore drop slab demonstrating how low cycle fatigue and tensile specimens were obtained from the material.

3.3.1 Tensile Testing

Tensile tests were conducted at room temperature and at 649°C according to ASTM standard E8 [44] on tension testing of metallic materials. Deformation was measured using crosshead displacement and a high temperature extensometer placed on the specimen. The purpose of the tensile tests was to obtain stress-strain relationships such as yield stress and strain, ultimate tensile strength, and Ramberg-Osgood hardening coefficients for a microstructural condition of Rene 88 with a similar grain size but slightly smaller average primary γ' diameter than microstructure conditions N and O; another objective was to observe how these properties varied from room temperature to 650ºC. A schematic of the tensile specimen is shown in Figure 3.6. The specimen has threaded ends with a 0.406 cm (0.16 inch) diameter reduced cross-section in the 2.54 cm (1 inch) gage length.

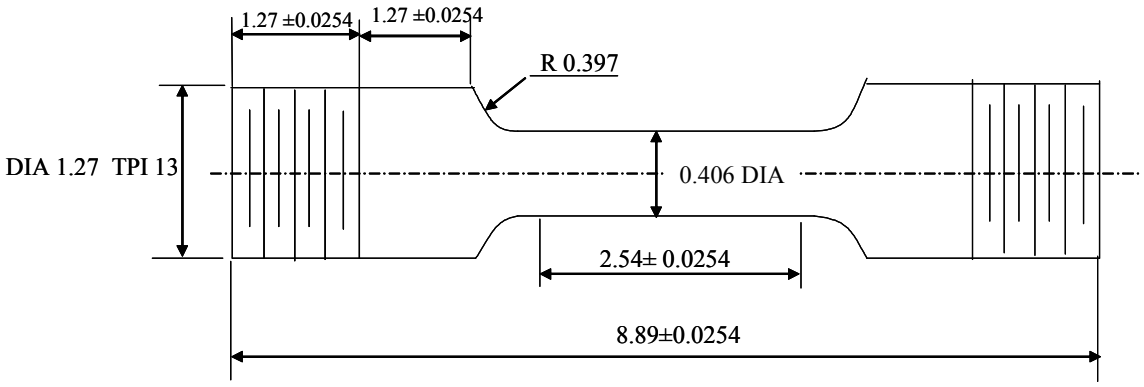

Figure 3.6. Schematic of the tensile specimen geometry (units are in centimeters).

3.3.2 Low Cycle Fatigue Testing

Low cycle fatigue tests were conducted to study crack initiation. The fatigue tests were performed at 649ºC in air with R=-1 and applied strain ranges of 0.66%, 0.75%, and 1.5% and met the requirements of ASTM standard E606 [45] on strain-controlled fatigue testing; the applied strain rate was approximately 0.5-0.75%/s. The experiments were generally stopped after a five percent load range drop from the saturation load range. The specimens were then fractured under high cycle fatigue conditions in load control at room temperature, so the crack initiation sites could be easily identified on the fracture surfaces. Data such as the saturation stress range, stress range at half life, and the number of cycles to a five percent drop from the saturation stress range are compared in the different microstructural conditions. A schematic of the low cycle fatigue specimen is shown in Figure 3.7. The specimen has a 0.635 cm (0.25 inch) diameter reduced cross section in a 1.27 cm (0.5 inch) gage length.

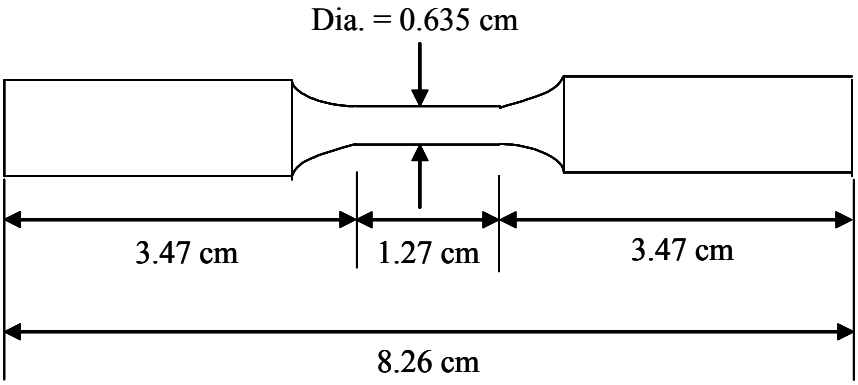

Figure 3.7. Schematic of the specimen used in uniaxial low cycle fatigue experiments.

It was discovered that all of the original specimen failures were artificially induced by cracking around the high temperature extensometer dimples or thermocouple welds (Figure 3.8) and thus had lower than expected lives. Therefore, an experimental setup was designed that eliminated the possibility of cracking from the tools measuring strain and temperature.

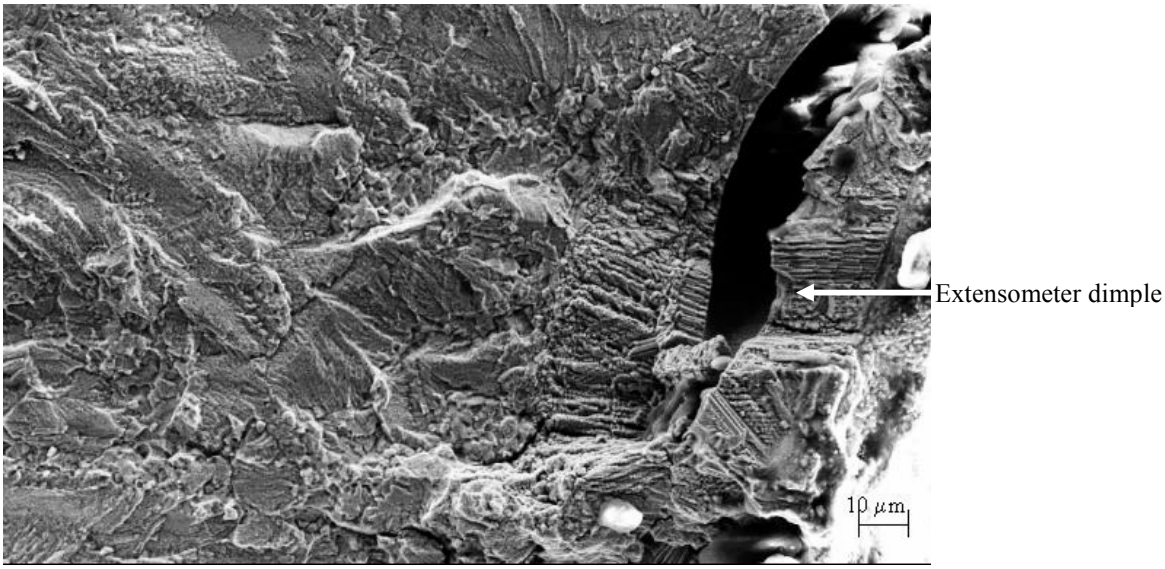

Figure 3.8. SEM image of a crack initiation region on a low cycle fatigue specimen.

ASTM standard E606 [45] states that strain should be measured directly on the gage length of the specimen using either a contacting extensometer or a digital imaging system, but it also notes that caution should be exercised in using an extensometer that has direct contact with the fatigue specimen because of possible damage that could arise in the specimen from the conical points or knife edges of the extensometer. The standard also suggests using epoxy where the extensometer contacts the specimen to protect the specimen from direct contact with the extensometer knife edges and to help the knife

edges remain seated on the specimen. However, it may be difficult to use either a digital imaging system or epoxy for high temperature fatigue testing; the furnace or induction coils used to heat the specimen may obstruct the digital imaging system and the epoxy melts at a low temperature (155-195°C).

To avoid using a conical extensometer and to accurately measure strain, an MTS model 632.06 displacement gage, or "one arm bandit", was used in a modified experimental setup. The one arm bandit measures load line displacement on the test actuator (Figure 3.9), so a dummy specimen was used to linearly calibrate the maximum and minimum values of the desired strain ranges measured by the extensometer to the corresponding displacement values measured by the one arm bandit on the actuator. In addition to the one arm bandit, a single thermocouple placed in the fillet of the LCF specimen was calibrated to the desired gage length temperature and monitored temperature during the LCF testing.

Figure 3.9. Picture of the one arm bandit applied to the low cycle fatigue setup, which uses a lever that rests on the actuator to measure actuator displacement.

Using the one arm bandit to measure strain in a fatigue specimen has obvious limitations with regard to the accuracy of the strain measurements. It measures displacement of the actuator which incorporates not only the displacement in the gage length of the specimen but also includes displacement of the gripped sections of the specimen and the machine compliance. Thus, it was initially thought that the one arm bandit could only be calibrated so the maximum and minimum values of the applied strain range would correspond to certain displacement values in the one arm bandit, but strain could not be accurately measured between those limits. However, a comparison of the hysteresis loops obtained in the saturation regime of low cycle fatigue testing with an applied strain range of $\Delta\varepsilon = 0.75\%$ shows that the strain data obtained by the one arm bandit is very similar to the data obtained by the extensometer in independent experiments on N and O condition specimens (Figure 3.10). This implies the strain measured in the gage length of

the specimen is very similar to the strain measured over the whole testing apparatus and that the compliance of the testing apparatus is negligible with a moderate applied strain range less than the cyclic yield strain.

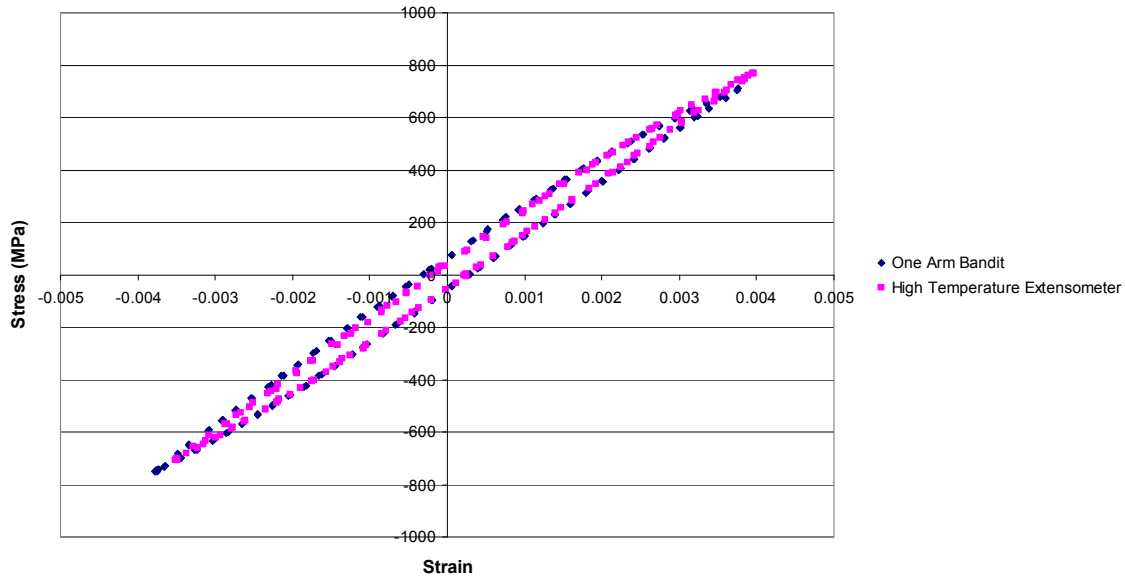

Figure 3.10. Stress-strain hysteresis loops obtained in the saturation regime for Rene 88DT with an applied strain range of $\Delta\varepsilon = 0.75\%$, R=-1, and a testing temperature of 650°C.

The one arm bandit was also calibrated to the high temperature extensometer for a strain range of $\Delta\varepsilon = 1.5\%$, but the resulting hysteresis loops from the two measurement devices did not compare as well (Figure 3.11). The hysteresis loops for the one arm bandit demonstrate much less plastic strain than the hysteresis loops obtained by the high temperature extensometer, which shows that the compliance of the testing apparatus is skewing the strain obtained by the one arm bandit. Since the calibration of the one arm bandit is based on a linear relationship between the stress and strain within the strain

range limits, the one arm bandit can still be used to accurately control the test for a large strain range; this is also demonstrated in Figure 3.11.

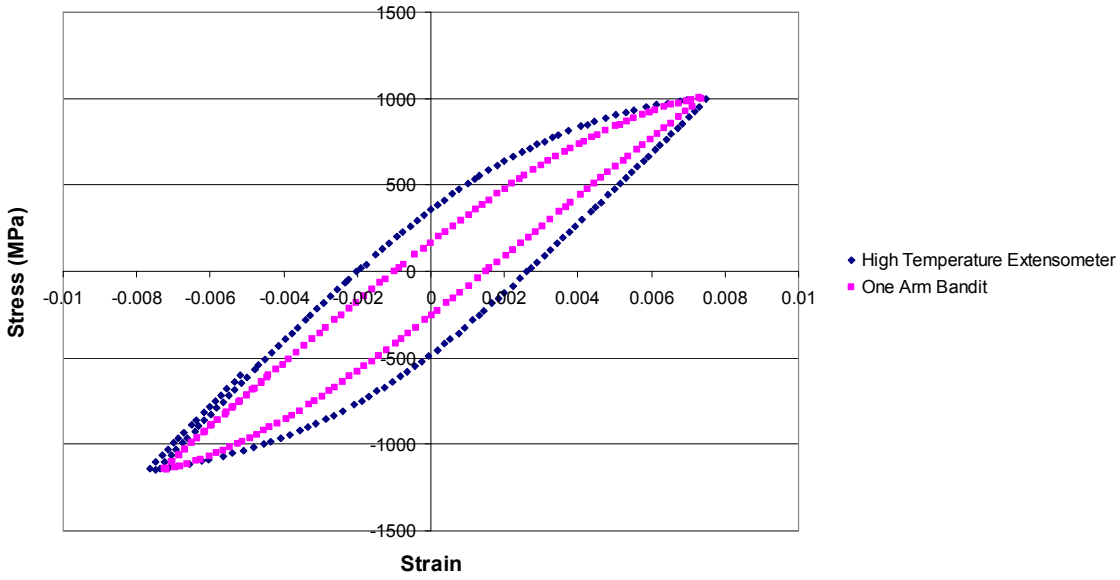

Figure 3.11. Stress-strain hysteresis loops obtained in the saturation regime for Rene 88DT with an applied strain range of 1.5%, R=-1, and a testing temperature of 650°C.

3.3.3 Fracture and Crack Analysis

The fracture surfaces of the all the LCF specimens were analyzed in an SEM to determine the crack initiation mechanism. Low magnification and a series of high magnification images around the crack initiation site were acquired. If the crack initiation appeared to originate at an inclusion, energy dispersive spectroscopy was performed to qualitatively determine the components of the second phase particle. Stereoscope pairs were generated by acquiring images of the same field of view at 0° tilt and at 10-15° tilt to aid in the analysis of the crack initiation and short fatigue crack growth.

One half of each fracture surface was mounted so that the initiation site was exposed; they were then ground and polished using the same procedure described above so that surface cracks and a cross section of the crack initiation region could be examined. The specimens may also be etched using one of the aforementioned etchants to determine how the secondary cracks move through the microstructure; or, electron backscatter diffraction (EBSD) analysis may be performed to understand how grain orientation affects the site of crack initiation and subsequent crack growth, especially when the initiation is due to slip band cracking on the surface.

Low magnification images of the fracture surfaces were acquired using a Leica MZ6 stereoscope. Vertical montages were obtained with the goal of imaging the fatigue striations surrounding the initiation site. These were used in conjunction with the finite element modeling to predict crack growth and morphology change.

3.3.4 Fracture Toughness Testing

Fracture toughness experiments were conducted on microstructure conditions N and O in the Engineering Research Center at the University of Arkansas. The specimen and tests were in accordance with ASTM standard E1820 on the fracture toughness testing of metallic materials [46]. A schematic of the specimen, a ½T compact type (C(T)) specimen, is shown in Figure 3.12; the original crack length was 1.14 cm. The specimen was small because of limited material availability and because nonlinear elastic-plastic fracture mechanics methods can be used for fracture toughness determination, if necessary. The specimens were fatigue precracked at room temperature in a 50 kN

servohydraulic test frame, fabricated by Test Resources. These machines were subsequently used to perform the fracture toughness experiments at 650°C. The load-line displacement was measured using a high temperature extensometer made by Epsilon Gages; the temperature was monitored directly on the specimen using thermocouples spot welded to the specimen and temperature fluctuations were less than +/- 3ºC. The objective of the experiments was to obtain a critical stress intensity factor for unstable crack growth that could be used in the finite element simulations that are described in the Results and Discussion chapter.

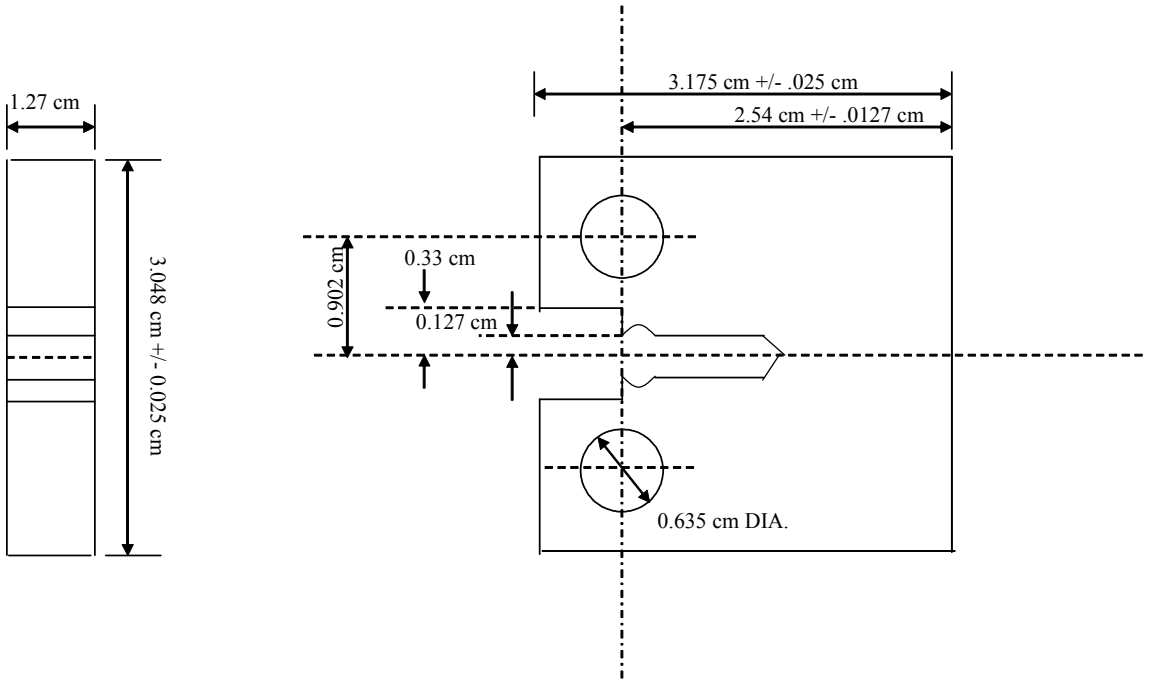

Figure 3.12. Schematic of the 1/2T C(T) specimen used to determine fracture toughness in microstructure conditions N and O.

The experiments were conducted in displacement control with an approximate displacement rate of 0.127 cm/min. Four experiments were completed. The first

experiment was loaded past the maximum load, cooled to room temperature, and subsequently fractured. Based on observations in the experimental data and fracture surface of the first specimen, which will be expounded in the Results and Discussion section, the loading of the remaining specimens was stopped short of or approximately at the peak load. The precrack length was measured by obtaining low magnification images of the fracture surface and then performing digital measurements of the precrack length.

3.3.5 Fatigue Crack Growth Testing

Fatigue crack growth experiments were performed on microstructure conditions N and O at 650°C using an MTS servohydraulic test machine; temperature was monitored using thermocouples welded directly to the specimen and fluctuations were limited to +/- 2ºC. The tests were conducted in accordance with ASTM standard E 647 on the standard practice for the measurement of fatigue crack growth rates [47]. A schematic of the specimen, with planar dimensions of a 1T C(T) specimen but only 1.27 cm (0.5 in) thick , is shown in Figure 3.14; the original crack length was 2.29 cm. A frequency of 10 Hz with an R ratio of 0.05 was used throughout the experiments. The specimens were precracked at high temperature in the initial phase of the crack growth. The objective of the experiments was to obtain the a Paris type relationship between crack growth rate and stress intensity in the form of

$$da/dN = C\Delta K^n \tag{3.3}$$

where da/dN is the crack growth rate, ΔK is the applied stress intensity range, and 'C' and 'n' are constants. This relationship is used for the finite element analysis simulations that are described in the Results and Discussion chapter.

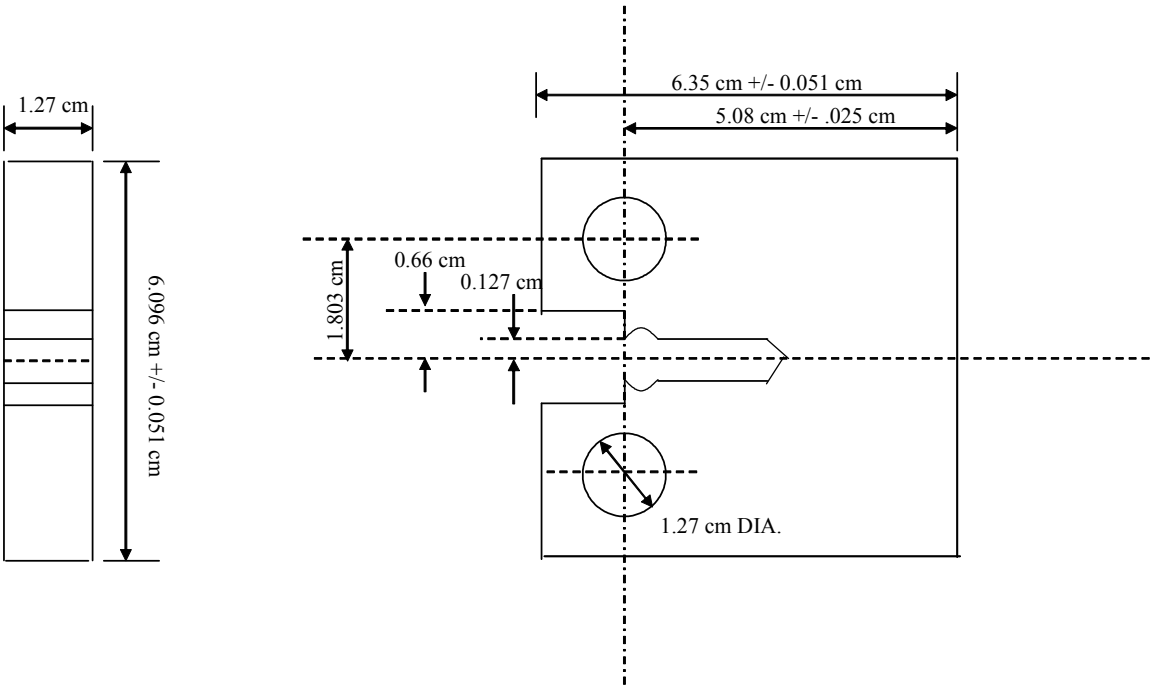

Figure 3.13. Schematic of the 1T C(T) specimen used to obtain fatigue crack growth rates for microstructure conditions N and O.

Three experiments were carried out, two on microstructure condition O and one on condition N. The crack length was measured using the electric potential drop technique outlined in the ASTM standard [47] and a constant input current source. Current is input and output at precise locations on the specimen, defined in studies by Saxena [48]; the output voltage is amplified and recorded at specified intervals. As the crack grows through the specimen, the resistance in the specimen decreases, and the output voltage becomes larger. The output voltage also increases due to thermal voltage, which can be

measured when the current input is switched off. The thermal voltage depends on the voltage generated due to a metallurgical junction between dissimilar materials at the lead connection locations, resistance heating within the leads, and intermediate testing temperatures; thermal voltage increases throughout an experiment and typically stabilizes but it must be carefully accounted for and subtracted from the output voltage measurements. Johnson's formula provides a relationship between the output current and crack length, which is very dependent on input and output lead location, and takes the form

$$a_i = \frac{2W}{\pi}\arccos\left(\frac{\cosh(\pi y/2W}{\cosh\left[\frac{V_i}{V_0}\arccos h\left(\frac{\cosh(\pi y/2W}{\cos\left(\pi a_0/2W\right)}\right)\right]}\right) \tag{3.4}$$

where a_0 is the original crack length, a_i is the instantaneous crack length, y is the vertical distance between the input leads, V_0 is the reference voltage measured at the beginning of the experiment, and V_i is the instantaneous voltage continually measured throughout the test.

The experiments were conducted in load control. In order to generate a precrack, ΔK = 27.5 MPa*m$^{0.5}$ was initially applied. The MTS program controlling the applied load and data acquisition was set up so that the applied ΔK reduced by 2-3 MPa*m$^{0.5}$ for every 0.05 mm increment of crack growth; this is an approximate value of crack length increment because there were often "spikes" in the voltage readings that prematurely

advanced the MTS program to the next increment of applied ΔK. Once a precrack of approximately 2.54 cm developed, the load was reduced further to ΔK ~ 20 MPa*$m^{0.5}$ and the rest of the experiment was carried out. The MTS program also featured a command that stopped the test once the crack reached a length slightly smaller than the crack size where specimen failure would occur. The specimens were loaded in fatigue at room temperature until they failed. The final crack length from the high temperature fatigue loading was measured from the fracture surface; the oxidation outlined the region of high temperature crack growth. If the final crack length differed from the predicted final crack length using Johnson's formula, a crack correction was applied to all measured crack lengths using a linear distribution of error.

3.4. Experimental Procedure Summary

Experiments were conducted in order to characterize the microstructure of three different conditions of Rene 88DT and then to study how the microstructures influenced intermediate temperature mechanical properties, with an emphasis on low cycle fatigue behavior. The experimental results were used to develop predictions for intermediate temperature crack initiation and growth behavior for different microstructural conditions.

CHAPTER 4

RESULTS AND DISCUSSION

4.1. Materials Characterization

One objective of the research was to relate stereological parameters of the microstructure to mechanical properties, specifically low cycle fatigue stress-strain behavior and crack initiation mechanisms. In order to accomplish this task, it was necessary to produce different microstructural conditions of the material for comparison. Two bore drops (Figures 3.4 and 3.5) were received from GE and subjected to heat treatments that are described in Table 4.1, which were based on heat treatments on Rene 88DT previously utilized by Kissinger [43]. Slabs machined from the bore drop were heated past the γ' solvus temperature (2100ºF) to homogenize the material but maintain the grain size. The grain size was kept constant between the two conditions. Then, the slabs were cooled in a two-step process where the first step cooling rates and transition temperature between the first and second cooling steps were varied; the goal of these heat treatment variations was to produce γ' size distributions similar to those listed in Table 4.2. A third microstructural condition was received from GEAE in the form of fractured LCF specimens with the approximately the same γ' precipitate size distribution from Ladish Co.; the heat treatment from this condition is proprietary and unknown and this microstructure condition will henceforth be called condition 'P'. Results in this section will show that the grain size in this condition was significantly finer than for the N and O conditions.

Table 4.1. Summary of the target heat treatments performed on Rene 88DT bore drop material.

	First Step Cooling Rate	Second Step Cooling Rate	Transition Temperature	Aging Temperature
N	16.5ºC/minute (30ºF/minute)	194ºC/minute (350ºF/minute)	1038ºC (1900ºF)	760ºC (1400ºF)
O	3.9ºC/minute (7ºF/minute)	194ºC/minute (350ºF/minute)	1093ºC (2000ºF)	760ºC (1400ºF)
P	As-received from GE			

Table 4.2. Expected γ' size distributions from heat treatments described above [43].

	Primary γ' Vv	Primary γ' size	Secondary γ' Vv	Secondary γ' size	Tertiary γ' Vv	Tertiary γ' size
N	0.16	0.351 um	0.163	0.071	0.06	0.015
O	0.28	0.15 um	0.0985	0.0217	--	0.01

The actual γ' size distributions obtained from the heat treatments were significantly different from the results of these heat treatments published in literature. It was found that the transition temperature of the heat treatments conducted by Bodycote Thermal Processing in this study was not varied; the transition temperature for both heat treatments was 1038°C. Also, the first step cooling rate for condition N did not reach 16.5ºC/minute; the maximum cooling rate during the step was approximately 8ºC/minute. A summary of the actual heat treatments is listed in Table 4.3 and temperature versus time curves are shown in APPENDIX B. The discrepancies between the desired and actual heat treatments significantly affected the resulting microstructures. In the work cited previously by Mao *et al.* [11], it was shown that the transition temperature in a two

step cooling process is an important parameter in the resulting primary γ' size. The approximate probability density distributions for the primary γ' size based on histogram data for the three microstructural conditions are shown in Figure 4.1; the results were obtained by acquiring high resolution SEM images and then using KS400 software to acquire data for the γ' precipitates.

Table 4.3. Actual heat treatments for microstructural conditions N and O.

	First Step Cooling Rate	Second Step Cooling Rate	Transition Temperature	Aging Temperature
N	8.3°C/minute (15°F/minute)	194°C/minute (350°F/minute)	1038°C (1900°F)	760°C (1400°F)
O	3.3°C/minute (6°F/minute)	194°C/minute (350°F/minute)	1038°C (1900°F)	760°C (1400°F)

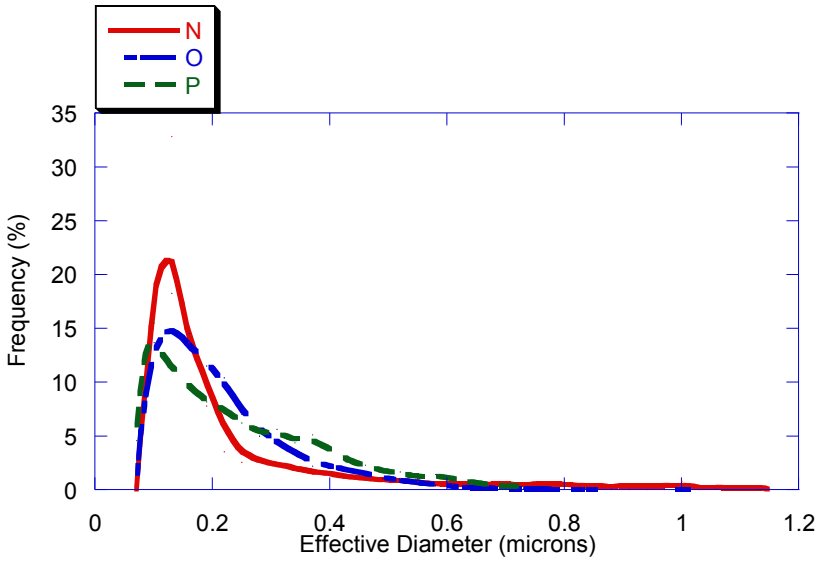

Figure 4.1. Primary γ' size distribution for the three microstructural conditions examined and tested.

The average effective diameter distributions of the γ' precipitates for the three microstructural conditions are very similar; the peak of the condition P size distribution is

at a slightly lower value than the peaks for conditions N and O, but the distributions around the peaks are comparable. The effective diameter is calculated by obtaining the two-dimensional area of the precipitate and then calculating the diameter of a circle with the same area. SEM images of the microstructure are shown in Figures 4.2 through 4.4. Though the effective diameters are similar for the three conditions, the observed shapes of the primary γ' are very different. The material from the P condition contains precipitates that are very square in shape. All of the precipitates that were observed in 2-D images were either square or triangular, depending on the grain orientation. These shapes imply a quicker cooling rate was used during the heat treatments than the cooling rates for the N and O conditions. There are square or triangular precipitates in conditions N and O, but the edges are not sharply defined; additionally, there are several larger precipitates that appear dendritic in nature. The difference in shapes of the precipitates between the conditions means there is probably at least a slight difference in the coherency strains between the primary γ' and the γ matrix, which could result in differences in stress-strain behavior, but this trend is not observed in the low cycle fatigue experiments described later in this chapter. The larger values of diameter at the tail of the γ' size distributions are due to γ' that nucleate and grow on the grain boundaries.

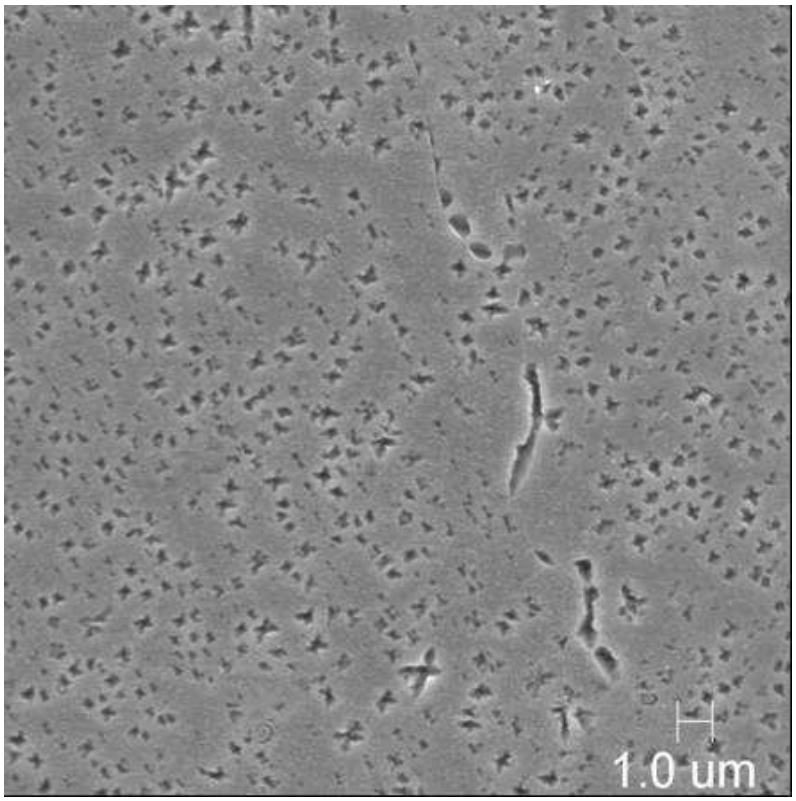

Figure 4.2. SEM micrograph of γ' precipitates in the N microstructure.

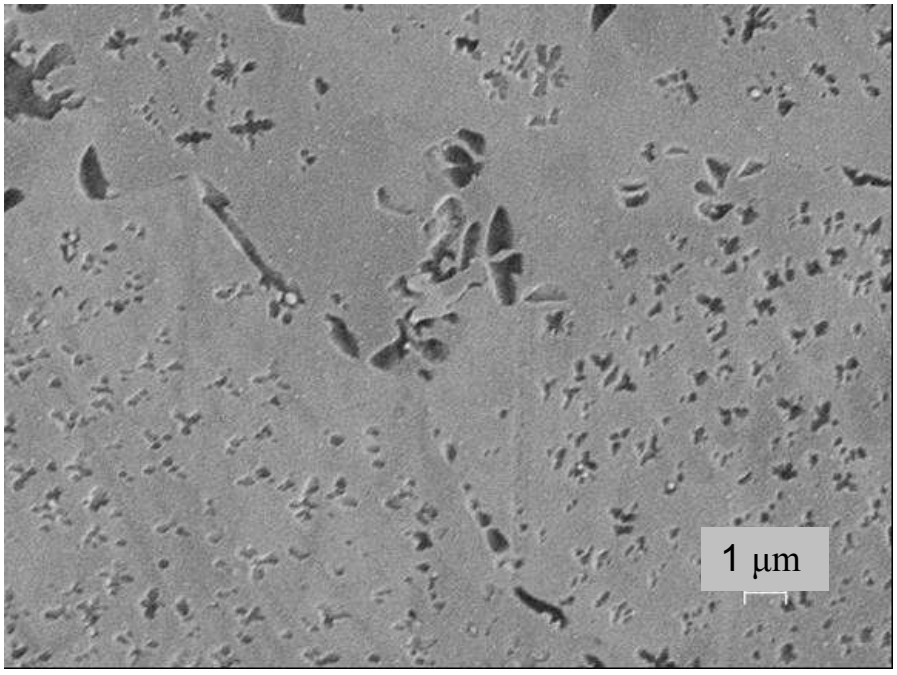

Figure 4.3. SEM micrograph of γ' precipitates in the O microstructure.

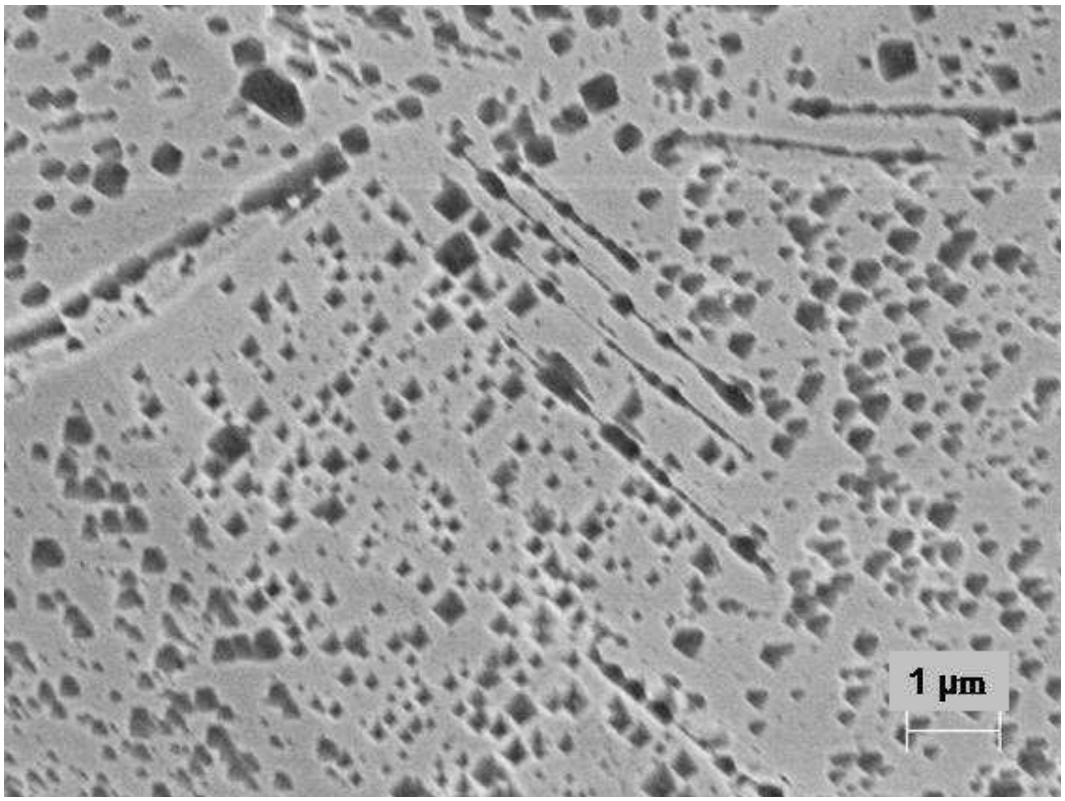

Figure 4.4. SEM micrograph of γ' precipitates in the P microstructure.

There are small differences in the nearest neighbor distance distribution of the primary γ' (Figure 4.5), which is also based on histogram data. The nearest neighbor distance distribution was calculated by determining the distance between the mathematical centers of gravity for each precipitate. The peak value of the O condition is smaller than the P condition and the N condition has a greater deviation in its spread. The nearest neighbor distribution is potentially important because it describes the shortest path a dislocation travels before it encounters another primary γ' obstacle; this could affect the flow stress and hardening properties of the material as well as affect the rate of short crack growth.

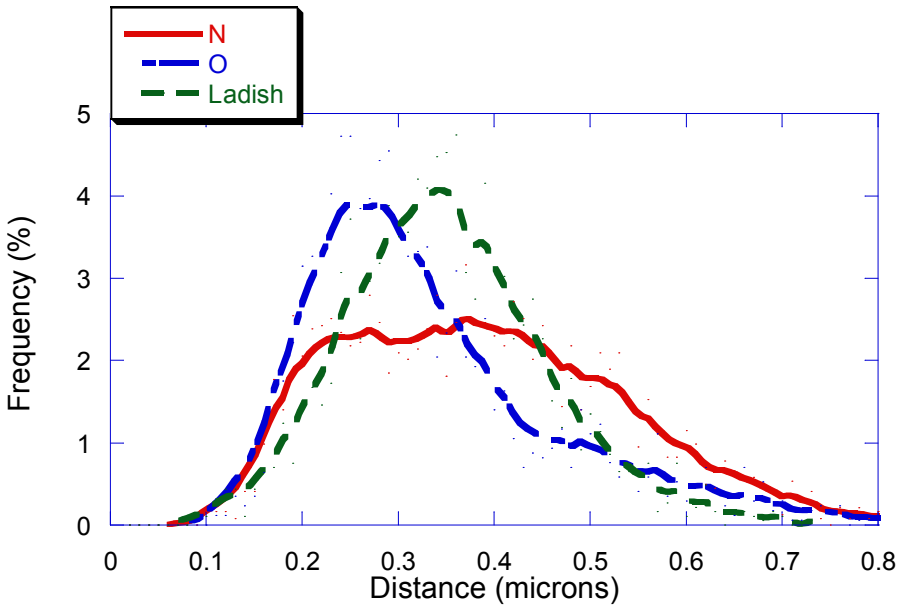

Figure 4.5. Distribution of the nearest neighbor distance between the γ' precipitates for the three microstructural conditions.

The grain sizes for conditions N and O were measured to be between 20 and 21 μm, so the goal of keeping grain size constant for these heat treatments was achieved. The grain size for the P condition was measured as 6 μm. The smaller grain size in the P condition may result in different fatigue crack initiation and growth behavior as reported by Miner and Gayda [31] who concluded that small grains retard crack initiation but promote crack growth. The microstructures are summarized in Table 4.4.

Table 4.4. Summary of the grain size and γ' characteristics for the three microstructures.

	Grain Size (μm)	Secondary γ′ Volume Fraction	γ' Average Diameter (μm)	γ′ Average NND (μm)
N	21	21%	0.258	0.383 +/-0.148
O	20	20%	0.28	0.342 +/- 0.156
P	6	22%	0.27	0.345 +/- 0.106

Because microstructures N and O are so similar in γ' size distribution, it is uncertain whether any differences should be observed between their monotonic stress-strain, cyclic stress-strain, and fatigue crack initiation and growth behavior. The shapes of the precipitates are very different between conditions N, O, and P, and the relationship between precipitate coherency, shape, and stress-strain behavior is unknown, so throughout this thesis the conditions have been labeled separately. Results presented later in the mechanical properties section indicate that precipitate shape differences in these microstructures has little influence on stress-strain characteristics. Similarity in the γ' size distribution and stress-strain behavior between all three conditions means that any fatigue crack initiation and growth behavior probably cannot be attributed to differences between precipitate characteristics in this study; however, as will be shown later, grain size plays a pivotal role in the fatigue crack initiation mechanisms and lives among the three conditions.

Some additional analysis was performed to determine carbide sizes for the N and O conditions. As described in Chapter 3, the etching characteristics for the P condition are different than the N and O condition, and it was difficult to obtain adequate contrast to accurately calculate carbide size parameter. The average effective diameter of the carbides in the N condition was approximately 0.31 μm, while the average effective diameter in the O condition was approximately 0.26 μm. Borides in the microstructure are larger in all three conditions, approximately 0.5-1 μm, in diameter. Figure 4.6 shows an estimated probability density distribution based on histogram data for the effective diameters for the N and O conditions; the distributions are approximately the same but the N condition carbides are slightly larger.

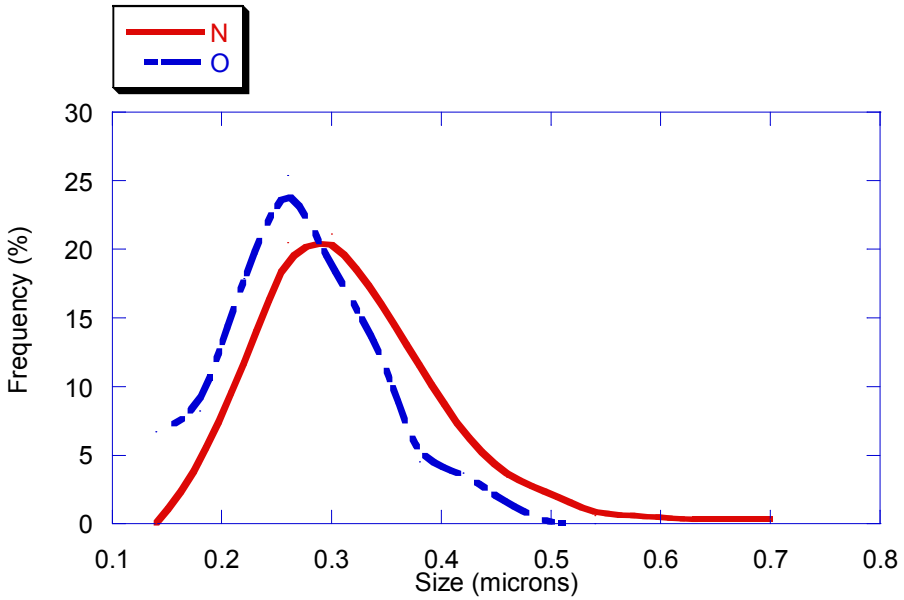

Figure 4.6. Estimated probability density distribution of the carbide effective diameters in the N and O conditions.

There is evidence, as described in the section discussing the disector method applied to carbide characterization, that the carbides are preferentially located around grain

boundaries; though no firm evidence is provided for the N and O conditions. Figure 4.7 shows a plot of the spatial locations of the carbides within the N condition microstructure. There are large areas void of carbides with diameters close to the grain size of the material (20 μm) and of similar morphology as the grain boundaries, implying that the carbides may be located on or around grain boundaries. This type of data along with the size distribution data could be valuable as input into microstructurally-based computer models.

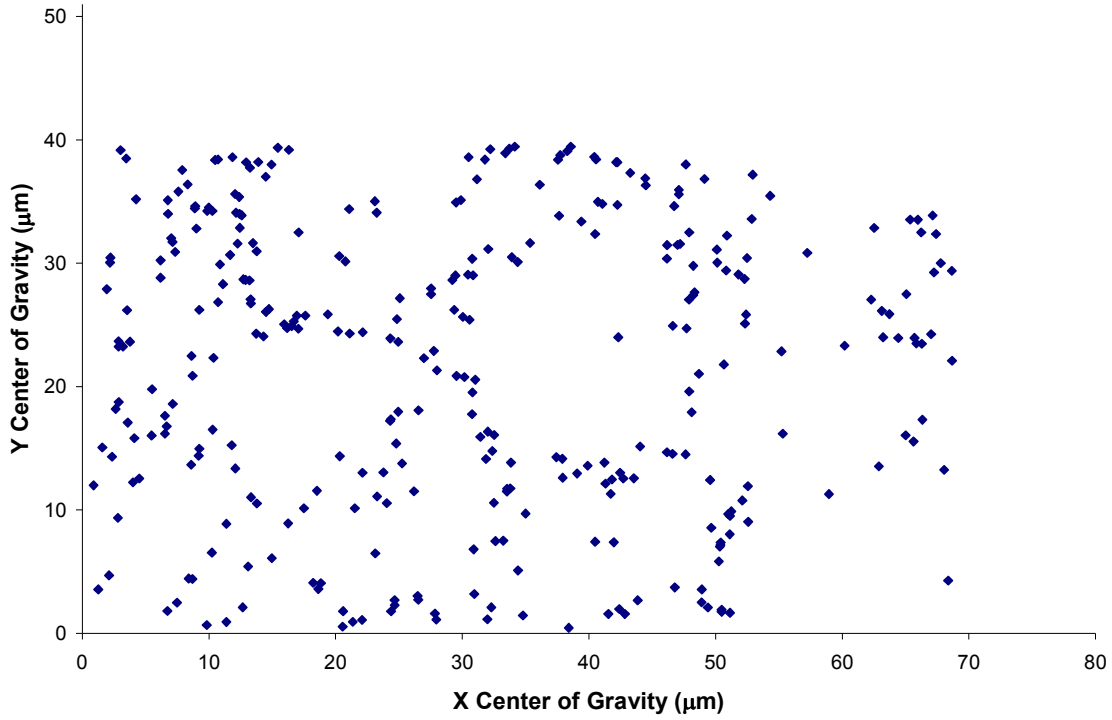

Figure 4.7. Spatial distribution of carbides within the N microstructure.

4.2. Mechanical Testing

Mechanical tests were performed on specimens from the three microstructures with an emphasis on determining the stress-strain behavior of the material and fatigue crack

initiation and growth mechanisms in the alloys. Tensile, low cycle fatigue, fracture toughness, and fatigue crack growth testing were performed on material conditions N and O to meet these objectives. Material from the P condition was received as fractured low cycle fatigue specimens, and material was not available to fabricate tensile, fracture toughness, and fatigue crack growth specimens for this condition. Therefore, only the LCF crack initiation behavior can be compared between the N, O, and P conditions. All of the mechanical testing was conducted at 650°C, which is a common temperature for turbine disk materials in application and in research.

4.2.1. Tensile Testing

Tensile tests were performed on a microstructural condition of Rene 88 that is similar in grain size to conditions N and O but has a slightly smaller average primary γ' size; the average grain size is 16.5 μm and the average diameter of the primary γ' is 0.135 μm. This microstructural condition is expected to have similar tensile properties to conditions N and O. Figure 4.8 shows the stress-strain curves for the specimens tested at room temperature, 399°C, and 649°C; Table 4.5 gives a summary of the results including the yield and tensile strengths and Ramberg-Osgood hardening coefficients. The specimen tested at a temperature of 399°C had the largest value of yield strength (1075 MPa); this anomalous yield strength behavior, where the yield strength increases with increasing temperature up to a certain point, is to be expected in nickel-base superalloys because of the strengthening characteristics of the ordered γ' precipitates. The specimen tested at room temperature had the largest value of ultimate tensile strength (1875 MPa). All three specimens exhibited significant plastic hardening, the Ramberg-Osgood hardening

exponent ranges between 4 and 6 for the three temperatures, which plays an important role in fracture toughness behavior described later in this section.

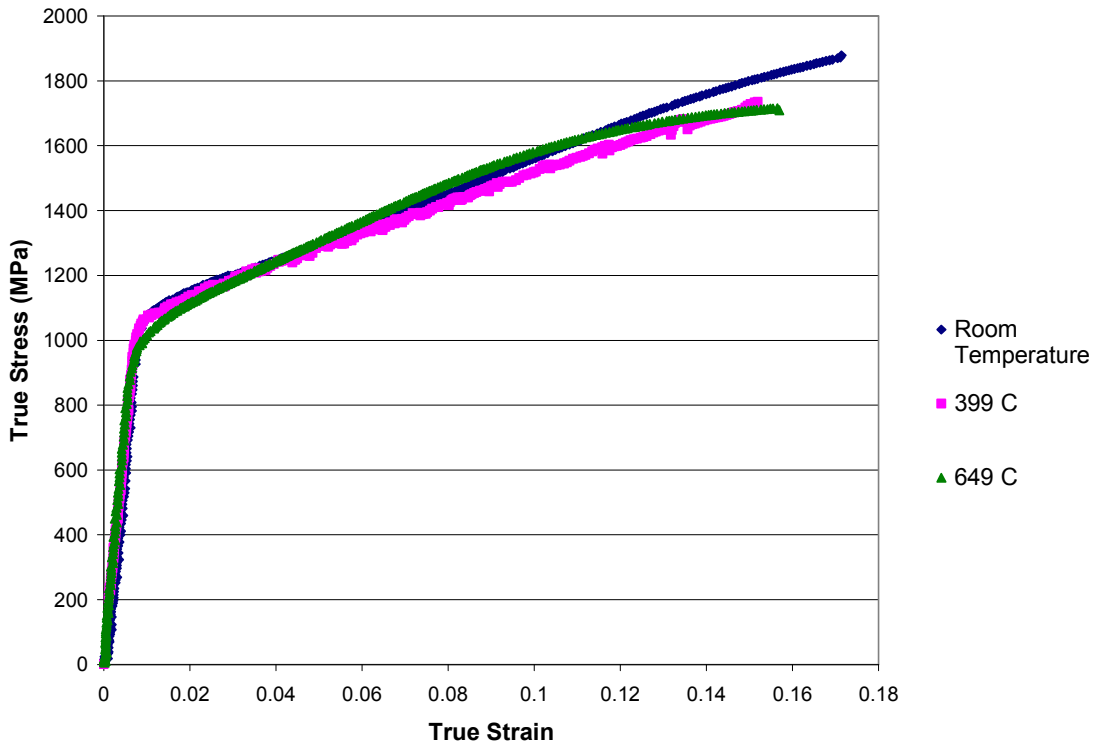

Figure 4.8. Stress-strain curves for Rene 88DT tested at room temperature, 399°C, and 649°C.

Table 4.5. Summary of the tensile properties for the experiments shown in Figure 4.8.

Temperature	σ(ys)	σ(UTS)	α	m
room temp	1048 MPa (152 ksi)	1875.4 MPa (272 ksi)	0.0147	4.356
399 C (750 F)	1075.6 MPa (156 ksi)	1737.5 MPa (252 ksi)	0.0168	4.996
649 C (1200 F)	989.4 MPa (143.5 ksi)	1716.8 MPa (249 ksi)	0.0065	5.738

4.2.2. Low Cycle Fatigue Testing

The objective of the low cycle fatigue (LCF) testing was to compare cyclic stress-strain behavior between the three microstructural conditions and to observe the relationship

between applied strain range, crack initiation mechanisms, and resulting fatigue lives; the experiments and the analysis were performed with this in mind. The objectives were achieved by conducting fatigue tests at strain ranges below and well above the cyclic yield strain at 650°C. The experimental setup and the test matrix are described in the experimental procedure section, but the matrix is also described in Table 4.6 for completeness.

Table 4.6. Test matrix for low cycle fatigue property comparison.

Condition	Δε (%)	R	number of specimens
N	0.66	-1	3
	0.75	-1	2
	1.5	-1	1
O	0.66	-1	3
	0.75	-1	2
	1.5	-1	2
P	0.66	0	3
	0.79	0	3
	0.95	0	2
	1.15	0	2

The major microstructural difference between the three conditions is the grain size: the average grain size in the P condition is approximately 6 μm while the average grain size in conditions N and O is approximately 20-21 μm. This difference in grain size could lead to a difference in the cyclic yield strength and the hardening properties between the three material conditions. Since the primary γ' size distribution and nearest neighbor distances are so similar among the three microstructures, these γ' sizes are not expected to produce any significant differences in the cyclic stress-strain behavior. The only major difference between the precipitates in the three conditions is their shape; the P condition

precipitates are more cuboidal in nature while the N and O precipitates range from cuboidal to dendritic.

The stress range was monitored for each test during strain cycling. A plot of the stress range versus number of cycles is shown in Figure 4.9. During the initial cycles of the fatigue experiments with conditions N and O, which were conducted with R=-1, the material cyclically softens as is expected from a high strength FCC material [49]. Subsequently, the majority of the test life is spent in a regime where the stress range is stable; this is called the saturation stress range and is seen as the plateau region in Figure 4.9. A true saturation stress range was rarely observed in the experiments, a behavior that is consistent with other precipitate hardening materials. In reality, the stress range during this "quasi-saturation" region decreased slightly over the range of cycles. This may be a manifestation of constant softening of the material or one could argue that the stress range decrease is due to crack initiation and short crack growth during this regime; multiple cracks may have initiated causing damage accumulation within the material and resulting in a macroscopic softening affect. Finally, the stress range decreases rapidly as a dominant crack begins to grow. The experiments were stopped and the LCF life was assumed to be exhausted when a 5% drop in load range was detected from the saturation load range.

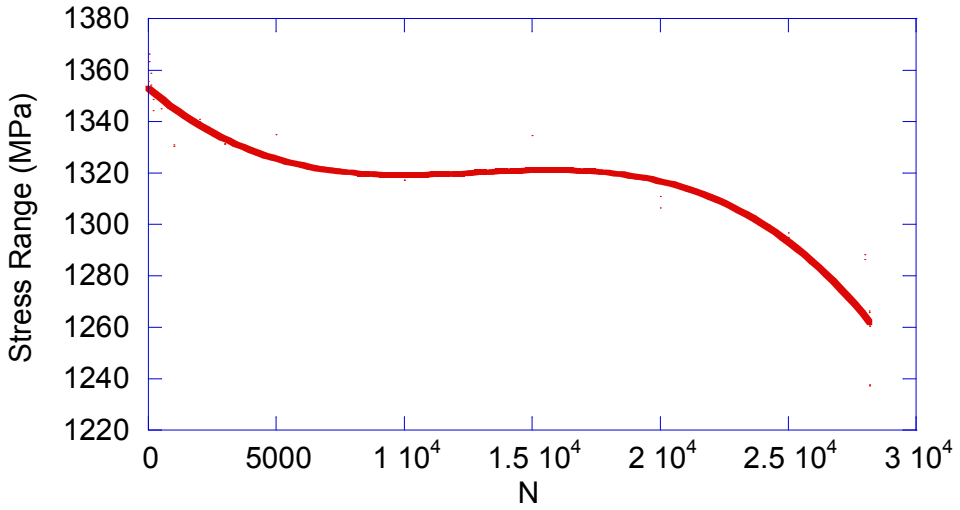

Figure 4.9. Plot of the typical stress range versus number of cycles for conditions N and O tested at $\Delta\varepsilon$=0.66% and 650ºC.

The P condition specimens were subjected to similar strain ranges but the tests were conducted with R=0. At all the strain ranges except $\Delta\varepsilon$=1.15%, the specimens cyclically hardened during the initial fatigue cycles. Because these experiments were conducted at R=0, there was a mean tensile stress throughout the test. This could induce more plastic hardening during the initial cycles than in the N and O conditions, or the smaller grain size in the P condition results in more hardening during the initial fatigue cycles. A plot of the stress range versus number of cycles for the strain ranges applied to the P condition is shown in Figure 4.10.

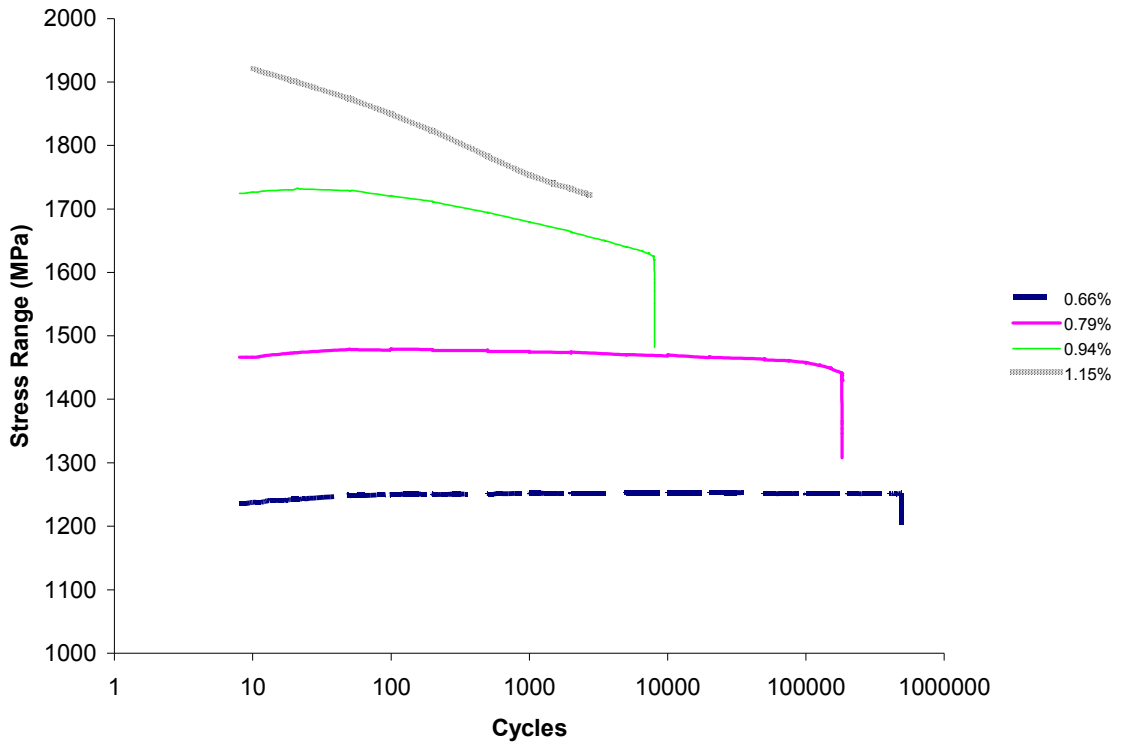

Figure 4.10. Stress range versus cycle number for a specimen from the P condition tested at $\Delta\varepsilon$=0.66% and 650ºC.

The $\Delta\sigma$ versus $\Delta\varepsilon$ behavior of the N and O condition is very similar, but the P condition material tested at similar strain ranges seems to exhibit slightly softer $\Delta\sigma$ versus $\Delta\varepsilon$ behavior (Figures A.1 and A.2) during the saturation stage of the fatigue test which could be due to the different R value used in the P condition experiments. There are some differences in the stress-strain behavior among the N and O conditions tested with $\Delta\varepsilon$ = 0.66%; but the microstructure is homogeneous throughout the material and furthermore, the low cycle fatigue specimens were removed from similar locations of the N and O bore drop sections so the differences are not due to microstructural effects. The disparity may be due to slight differences in compliance of the individual specimens from small cracks initiating in the material. The P condition $\Delta\sigma$ versus $\Delta\varepsilon$ behavior may be softer

because of the imposed mean tensile stress during the test contrary to zero mean stress in the N and O conditions during the fatigue experiments. The P condition experiments performed with $\Delta\varepsilon = 0.94\%$ and $\Delta\ \varepsilon = 1.15\%$ also exhibit some variation in the stress-strain response at each strain range (Figures A.3 and A.4). Again, this may be due to differences in compliance in the specimens from cracks initiating at different cycle numbers for each specimen; different initiation mechanisms may also contribute to variations in compliance. The P condition specimens tested at $\Delta\varepsilon = 1.15\%$ also had multiple initiation sites and exhibited the possibility of demonstrating slightly different $\Delta\sigma$ versus $\Delta\varepsilon$ behavior due to differences in compliance. Accurate comparisons cannot be made between the fatigue stress-strain behavior of the N and O specimens tested with $\Delta\varepsilon = 1.5\%$ because of the limitations of acquiring accurate strain values using the one arm bandit when substantial plasticity is present throughout the experiment as mentioned previously in the chapter on Experimental Procedure.

Table 4.7 is a summary of the low cycle fatigue results for the three conditions including strain range, saturation stress range or stress range at half life if it is more appropriate, and cycles to failure.

Table 4.7. Summary of low cycle fatigue results from the N, O, and P conditions.

Specimen	Strain Range	Cycles to Failure	Stress Range at Half Life (MPa)
ND-1	0.0066	58550	1241
ND-2	0.0066	22210	1276
ND-4	0.0066	25000	1324
OD-4	0.0066	98475	1351
OE-1	0.0066	16915	1358
OE-4	0.0066	44070	1310
P 233	0.0066	491180	1255
P 144R	0.0066	928420	1248
P 155	0.0066	977060	1241
NC-4	0.0075	4680	1448
NC-5	0.0075	5500	1462
OD-3	0.0075	11075	1475
OD-5	0.0075	5080	1510
P 133	0.0079	139150	1448
P 122R	0.0079	182200	1455
P 222	0.0079	197570	1448
P 211	0.0094	8040	1641
P 111	0.0094	58330	1579
P 200	0.0113	2750	--
P 100	0.0115	2860	1724
ND-3	0.015	171	2199
OE-2	0.015	122	2324
OE-3	0.015	175	2199

The white and grey shaded areas of the table compare experiments performed at similar strain ranges. The summary demonstrates a noticeable difference between the number of cycles to failure for specimens from the P condition and the number of cycles to failure for conditions N and O. For example, at $\Delta\varepsilon = 0.66\%$, the number of cycles to failure for the N and O conditions varies between 16,915 and 98,475; the corresponding number of

cycles to failure at $\Delta\varepsilon = 0.66\%$ in the P condition varies between 491,180 and 977,060. There is an order of magnitude difference in the cycles to failure between the P and the N and O conditions. A similar trend is observed for the specimens tested between $\Delta\varepsilon = 0.75\%$ and $\Delta\varepsilon = 0.79\%$. For N and O, the number of cycles to failure ranges from 4,680 to 11,075, while the number of cycles to failure in the P condition varies between 139,150 and 197,570, which is more than an order of magnitude difference. The saturation or half life stress ranges for these conditions, on the other hand, are very similar. For $\Delta\varepsilon = 0.66\%$, the stress ranges are between 1,241 and 1,358 MPa for N and O and are between 1,241 and 1,255 MPa for the P condition. At $\Delta\varepsilon = 0.75\%$ to $\Delta\varepsilon = 0.79\%$, the limits of the stress ranges are 1,448 and 1,510 MPa for N and O, while the stress range is between 1,448 and 1,455 MPa for the P condition.

The similarity in the saturation stress range values and the $\Delta\sigma$ versus $\Delta\varepsilon$ behavior for the three conditions indicates the microstructural differences between them do not result in significantly different cyclic stress-strain properties. There is obviously a difference, though, in the crack initiation and growth resistance between the materials. Figure 4.11 compares the cycles to failure at $\Delta\varepsilon = 0.66\%$ for the three conditions and makes obvious the magnitude of the difference in cycles to failure. These results point to the conclusion that the cyclic stress-strain behavior is perhaps uniquely dependent on the γ' size distribution and volume fraction, which was not different among the N, O, and P conditions, while the differences in grain size and γ' morphology do not appear to significantly affect stress-strain behavior.

As described in the Experimental Procedure chapter, there is a difference in the geometries of the N and O specimens compared to the P specimens. The gage diameter of the N and O specimens is 6.35 mm while the gage diameter in the P specimens is 10.08 mm. If there was no difference in the microstructures of the three conditions, then the LCF specimen size difference should result in longer fatigue lives for the smaller diameter specimens. The larger diameter specimens, used for material condition P, have a larger volume which increases the probability that deleterious defects are present within the gage section. Increasing the diameter also decreases the stress gradient across the diameter and increases the volume of material that is highly stressed. The P condition specimens have much longer fatigue lives despite having larger diameters than the N and O condition specimens, which supports the assertion that there is a microstructural difference in the three conditions that is significantly influencing the observed fatigue lives.

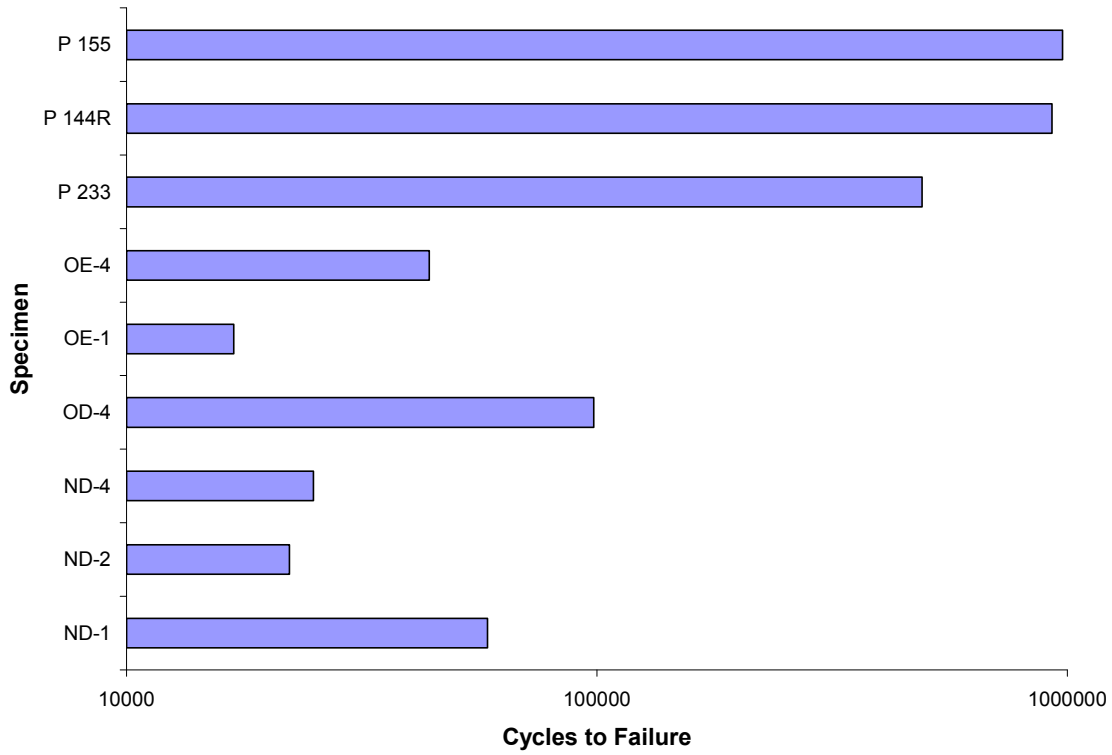

Figure 4.11. Bar chart demonstrating the significant difference in cycles to failure between the P and N and O conditions for tested at $\Delta\varepsilon$=0.66% and 650ºC.

Figure 4.12 shows a plot of the applied strain range versus the number of cycles to failure for the N, O, and P conditions. Four data points from work by Caton *et al.* [2] are also included for comparison, though those experiments were conducted at 593°C. The diagram shows there is a large amount of scatter in the data at all the applied strain ranges. Even amongst the P condition data, there is significant scatter; for example at $\Delta\varepsilon$ = 0.66%, the number of cycles to failure ranges from 491,180 to 977,060, which is a factor of two difference. It is also obvious that the strain range versus cycles to failure follows an almost identical trend between the N and O conditions and this trend is below the trend observed for the P condition over all the applied strain ranges. One of the main objectives defined in the early stages of this research was to determine the mechanisms

behind the variability in fatigue life, which is easily observed in Figure 4.12. The results also help define another important objective: to determine the reason the cycles to failure in the P condition far exceeds the cycles to failure in conditions N and O. These objectives can be completed at least partly through fractographic analysis of the fatigue initiation mechanisms, which will be described in the following section. Models will also be introduced based on the LCF results and the fracture surface images to help explain this variability in fatigue life.

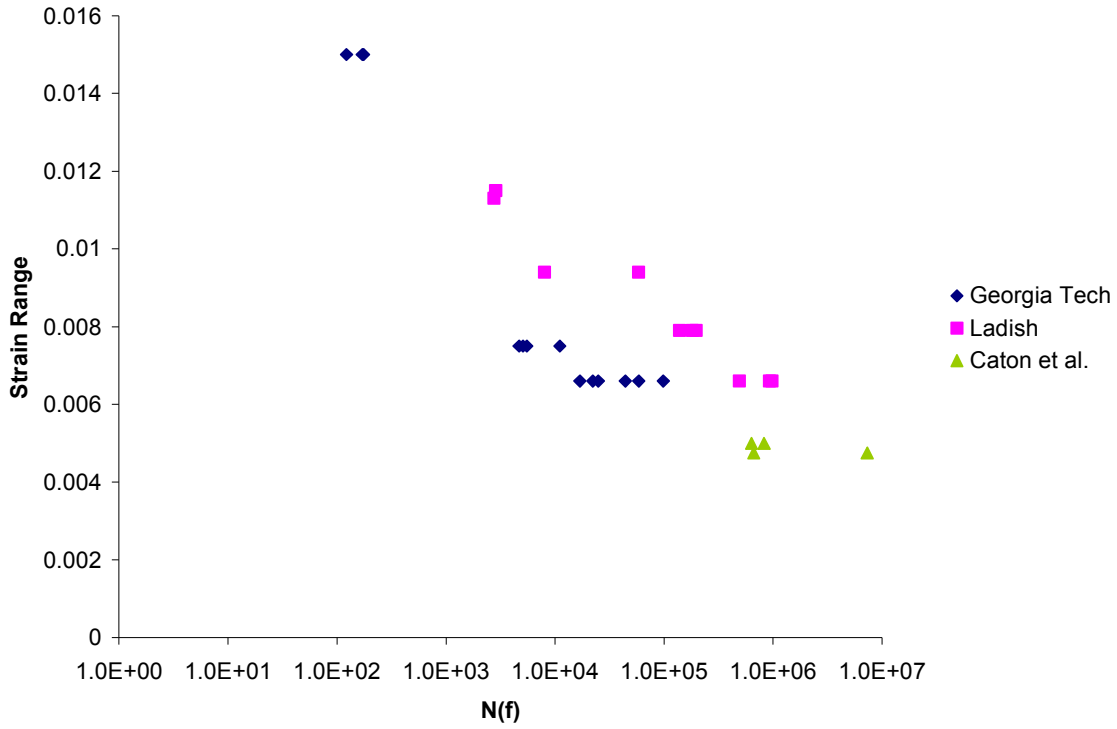

Figure 4.12. Plot of the strain range versus number of cycles to failure for the N, O, and P conditions. Data from the Caton *et al.* is also included.

Fracture surface analysis was performed on the low cycle fatigue specimens using low and high magnification (~40x-1000x) optical microscopes and high magnification

electron microscopes (~50x-15000x); imaging methods were developed with the intent of observing the crack initiation, short crack growth, and long crack growth regimes of the fatigue life. Lower magnification optical microscopes were utilized to observe macroscopic features such as oxidation patterns that relate to crack initiation and growth on the fracture surface and also fatigue striations. Scanning electron microscopes were used predominantly to observe local crack initiation and short crack growth features. The objective was to trace the fatigue crack initiation sites on each fracture surface and determine the mechanisms associated with each crack initiation. It was found that the initiation was dominated by two different mechanisms: cracks initiating due to plastic damage accumulation in slip bands on the surface of the specimens and cracks initiating around inclusions in the surface or subsurface of the specimen. A comprehensive set of fracture surface images is shown in Appendix C.

All of the specimens tested exhibit obvious oxidation patterns outlining the shape of the crack and the direction of crack growth; this helped in identifying crack initiation and short crack growth regimes on the fracture surfaces. Figure 4.13 shows a low magnification image of specimen ND-1 acquired from an optical stereoscope, tested with $\Delta\varepsilon = 0.66\%$, where the fracture surface and oxidation pattern indicates the dominant crack initiated on the specimen surface. A similar fracture surface image of P 233, also tested with $\Delta\varepsilon = 0.66\%$, shows the dominant crack initiated in the subsurface of the specimen (Figure 4.14); the oxidation pattern this time forms a circular pattern around the crack initiation site. The fracture surface is damaged where the opposite fracture surface

may have crushed into the surface in a small area where the crack could be defined as a long fatigue crack.

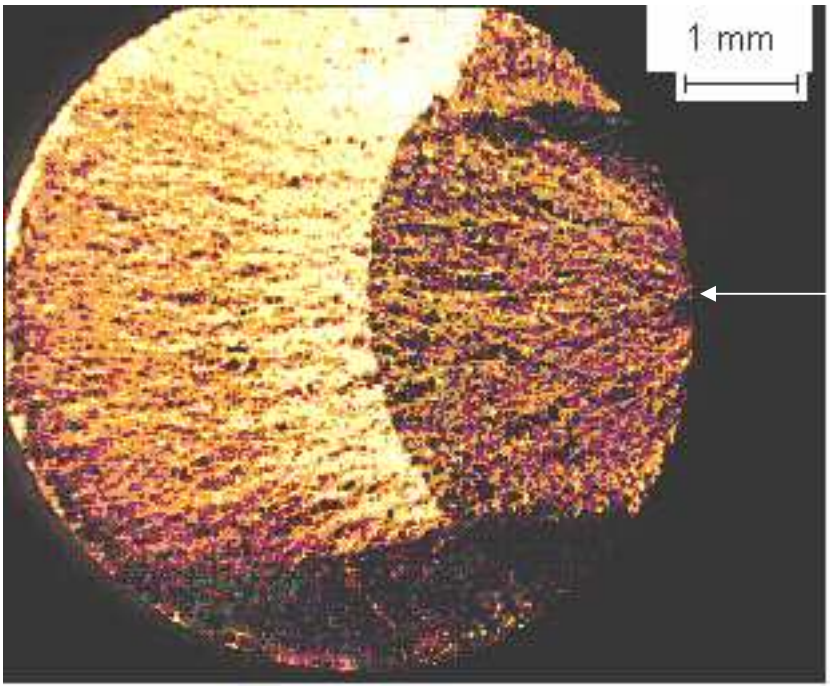

Figure 4.13. Low magnification stereoscope image of the fracture surface of specimen ND-1 tested at $\Delta\varepsilon$=0.66% and 650ºC.

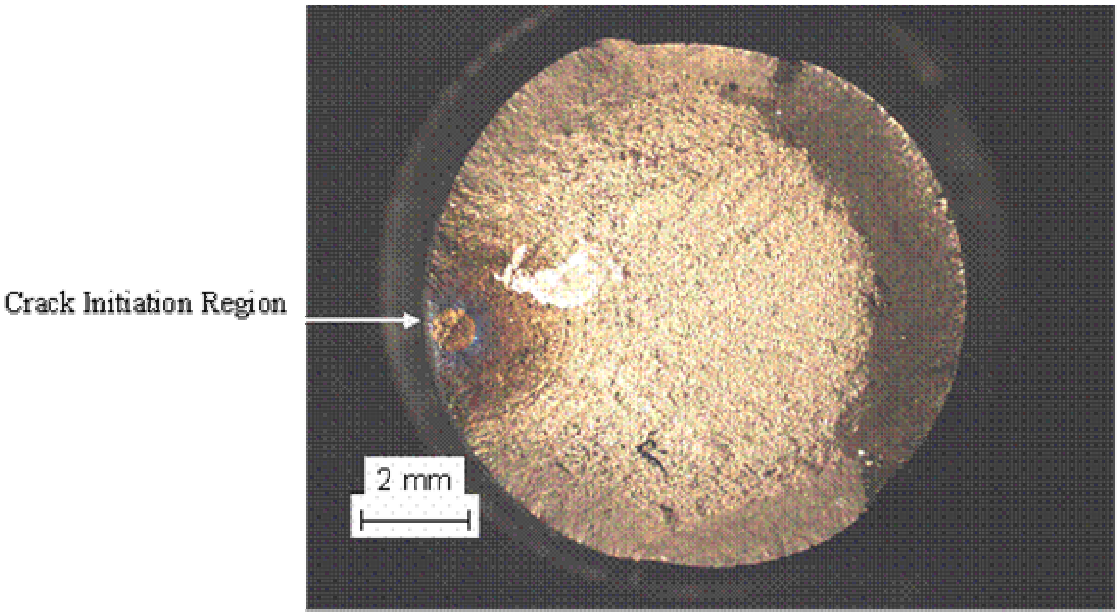

Figure 4.14. Low magnification stereoscope image of the fracture surface of P 233 tested at $\Delta\varepsilon$=0.66% and 650ºC.

Whether crack initiation occurs on the surface or subsurface of the fatigue specimens appears to be indicative of the two different initiation mechanisms; in general, cracks initiating from the surface of the fatigue specimens originate from slip band cracking due to plastic damage in a local region of grains, while cracks initiating in the subsurface of the fatigue specimens started at an inclusion particle or cluster of inclusion particles. The region around the initiation site of specimen ND-1 is shown in Figure 4.15, an intermediate magnification SEM image. Radial lines, or a river pattern points back to the initiation area, which is a small approximately 20 μm wide area on the surface of the specimen. There is a larger region defining a short "thumbnail" crack and consisting of very facetted fracture along different grain orientations. Outside of this region, the fracture exhibits more ductile or tearing type characteristics. A similar initiation region is shown in Figure 4.16 of a specimen tested with $\Delta\varepsilon$ = 0.75% and demonstrating similar crack initiation characteristics. In this SEM image, however, the specimen is tilted 90º so

the electron beam is normal to the exterior surface of the round bar in the vicinity of the crack initiation region. It shows the initiation site is oriented 30-45º from the loading axis and it appears to be composed of slip bands spaced approximately 1 μm apart. Thus, the most probable initiation mechanism demonstrated by these specimens is initiation from slip band cracking. Boyd-Lee and King [23, 24, 32], Healy *et al*. [33, 34], and Alexandre *et al*. [36] have also concluded slip band crack initiation is likely in fatigue conditions in nickel-base superalloys. The orientation of the crack initiation site in Figure 4.16 with respect to the specimen is consistent with the mechanism proposed by Boyd-Lee and King as favorable for producing slip band crack initiation. Similar observations and analysis was performed in this study to assert the possibility of slip band cracking.

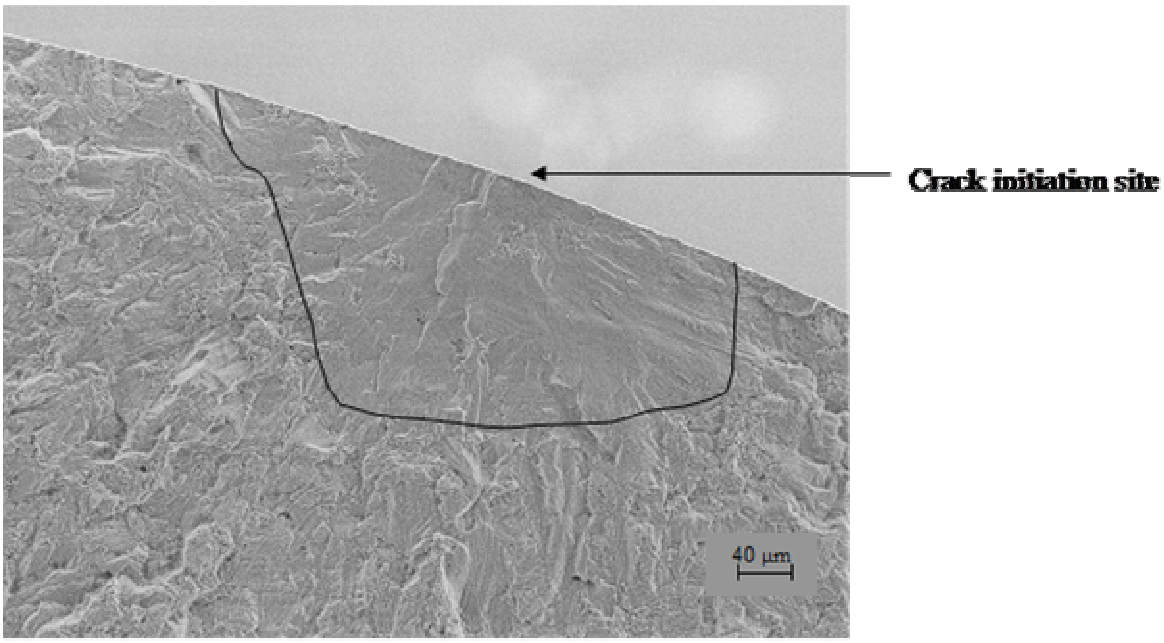

Figure 4.15. SEM image of the crack initiation region in specimen ND-1 tested at Δε=0.66% and 650ºC.

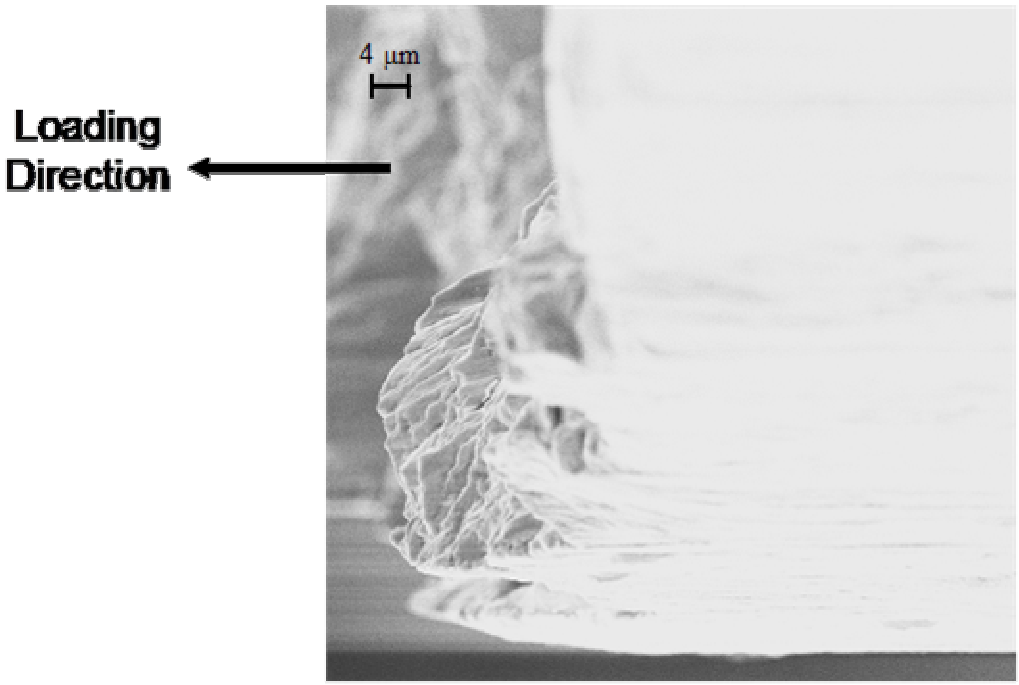

Figure 4.16. SEM image of a specimen tested at Δε=0.79% and 650ºC tilted so the exterior surface of the specimen is normal to the electron beam in the vicinity of the crack initiation region.

Evidence of slip band cracking is also present on optical microscope images of the side surfaces of the round bar specimens in the proximity of the crack initiation region. To obtain these images, one half of the low cycle fatigue specimen was mounted in transparent epoxy with the gage section on its side and so the crack initiation region was exposed to the surface of the mount. It was then lightly polished to produce a small flat area on the side of the gage section exposing cracks in the region of the initiation site. Figure 4.17 shows one such image taken from specimen OD-5, which was tested with Δε = 0.75%. The image clearly shows a large crack that has initiated and grown between 30 and 60 degrees from the loading direction and intersects the fracture surface in the crack initiation region. Additionally, side branches emanate perpendicular to the major crack and the lowest branch becomes a crack of comparable size with another large crack

extending from it. The orientation of these cracks with respect to the loading direction and the orthogonal nature of the major cracks and side branches provides evidence of slip band cracking on orthogonal primary slip systems such as the {111}<110> family, which would be the most favorable slip system in Rene 88DT. Cracks that were oriented 30º-60º to the loading axis were present in almost every N and O condition specimen.

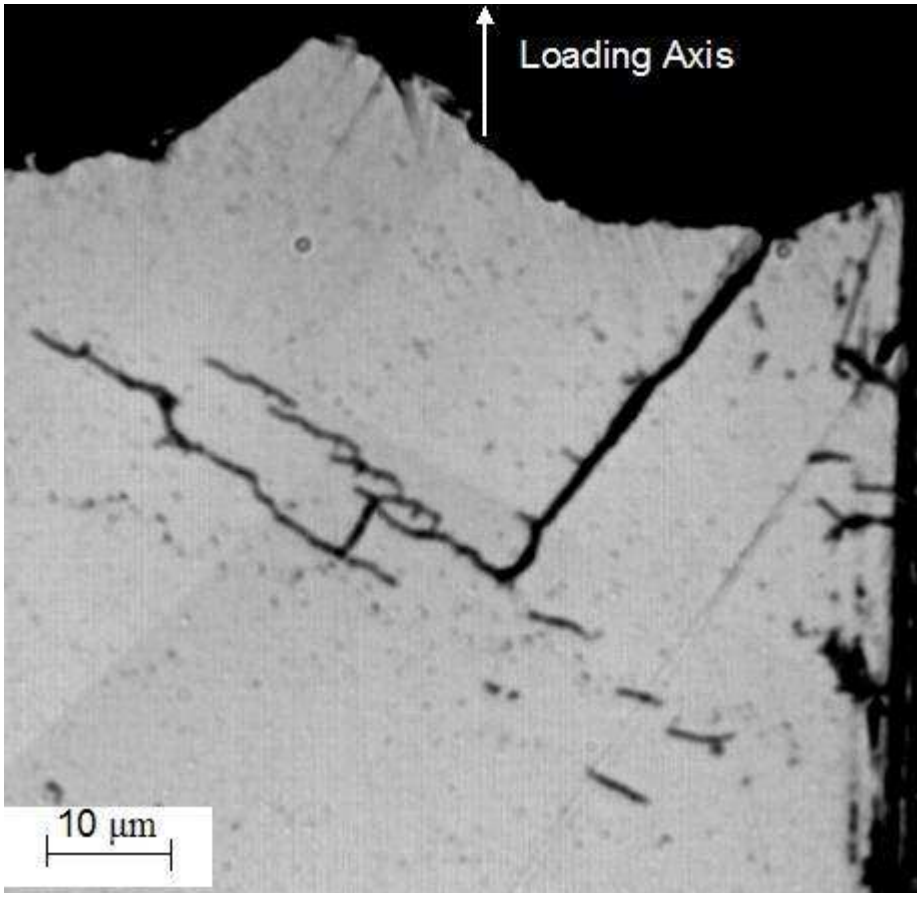

Figure 4.17. Side view of a polished section around the crack initiation region in specimen OD-5, tested at $\Delta\varepsilon = 0.75\%$ and 650ºC.

The other prominent initiation mechanism involved cracks initiating from inclusion particles in the material. These inclusion particles most likely are type 1 or 2 defects [19]

and contaminate the material during the powder processing stages. Their size and subsequently, their deleterious affect on fatigue properties, is limited by the mesh size used during the powder processing. Cracks are likely to nucleate around inclusion particles because they generally have a different coefficient of thermal expansion than the Rene 88 material and they are natural stress concentration sites as brittle phases in the matrix. Inclusion cracking was only found in the P condition in this research, but several other researchers have investigated inclusion crack initiation in Rene 88 and other nickel-base superalloys [1, 19, 25, 26, 28, 36]. Powder processing has been refined over the years to limit the volume fractions and sizes of these inclusions [1].

In the P condition, inclusions or particles initiated cracks in five of the ten specimens tested. All of the specimens tested above $\Delta\varepsilon = 0.94\%$ had a dominant crack that initiated due to slip band cracks except one, where the crack initiation started at a small surface particle (Figure B.7). Crack initiation from inclusions was never observed in specimens from the N and O material. This mechanism was most prominent in the P condition specimens tested with $\Delta\varepsilon = 0.79\%$, where all three specimens had cracks originating at inclusion clusters. However, it cannot be immediately concluded that $\Delta\varepsilon = 0.79\%$ provides an optimal strain range for inclusion cracking to prevail over initiation from slip band cracking; there is also the possibility that the three specimens tested with $\Delta\varepsilon=0.79\%$ came from a similar region of the bulk material which had a higher volume fraction of inclusions.

Figure 4.18 shows a low magnification optical image of a P specimen fracture surface tested at $\Delta\varepsilon = 0.79\%$ where the dominant crack initiated from a cluster of inclusions; the loading direction is orthogonal to the image. Oxidation forms a circular pattern around the initiation site with shades of blue forming approximately concentric rings around the internal initiation site. Looking carefully, one can see the region of short crack growth, which forms in an almost perfect circle around the particle cluster. Oxidation patterns indicate the internal crack burst through the surface of the specimen at some point and became an edge crack, the shape of which can also be observed through the oxidation patterns.

Figure 4.18. Low magnification image of the low cycle fatigue fracture surface from P 222 tested at $\Delta\varepsilon=0.79\%$ and 650ºC. The oxidation pattern outlines a subsurface crack initiation site.

An intermediate magnification SEM image reveals that the initiation site is a cluster of particles (Figure 4.19). A river or radial pattern on the fracture surface points back to the particle cluster, indicating that the dominant crack did indeed start there. A higher

magnification image of the particle cluster (Figure 4.20) shows the cluster is made up of individual particles that have conglomerated. Energy dispersive spectroscopy (EDS) analysis was performed on the particles; EDS can only be used to produce semi-quantitative results because the penetration depth into the specimen of the sampling beam is unknown. The resulting EDS peaks show the presence of strong aluminum and oxygen peaks compared to an EDS spectrum from the matrix material (Figure 4.21). Literature sources have stated the possible presence of aluminum oxide particles in the material is due to defects from the powder processing [19, 25], and the EDS analysis implies the particles present on the P condition fracture surfaces are aluminum oxide particles. These particles, though present in extremely low volume fractions, can be very detrimental to fatigue life because they have a different coefficient of thermal expansion than the matrix and they are very brittle phases. In fact, the K_{Ic} fracture toughness value for Al_2O_3 lies between 2.7-4.2 MPa*$m^{0.5}$ [50]. Assuming, a small 1 μm flaw is present in one of the particles and the maximum stress applied during cycling is 1400 MPa, which is close to the stress applied during the $\Delta\varepsilon = 0.66\%$ tests, the stress intensity in the particle is approximately 2.48 MPa*$m^{0.5}$; this value shows cracking can easily occur in the particle cluster on the first cycle. The region around the cluster is very facetted extending into a circular ring around the crack initiation site as shown previously in Figure 4.18. Outside of this region, the crack growth displays more of a ductile, tearing type mechanism.

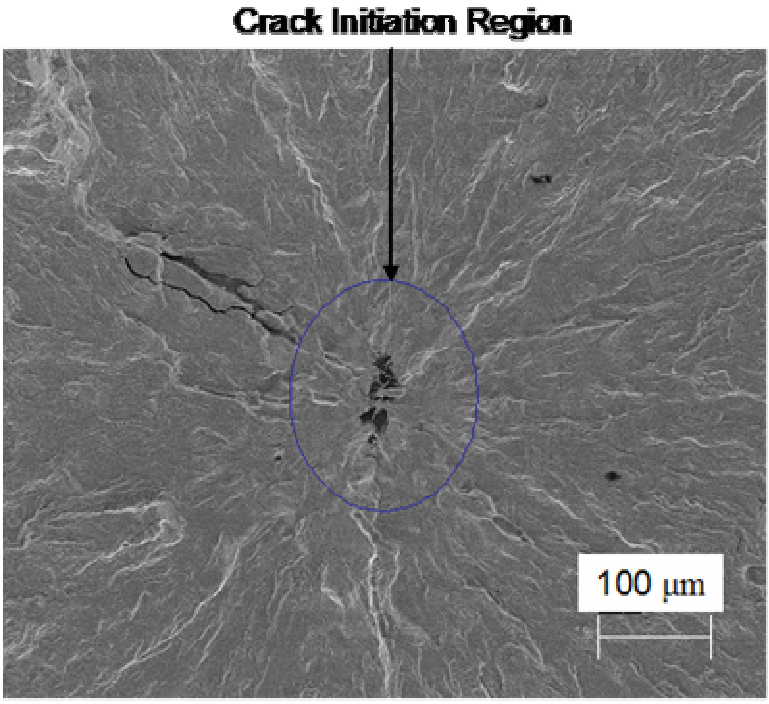

Figure 4.19. SEM image of a cluster of particles in the initiation region for a specimen tested at Δε=0.79% and at 650ºC.

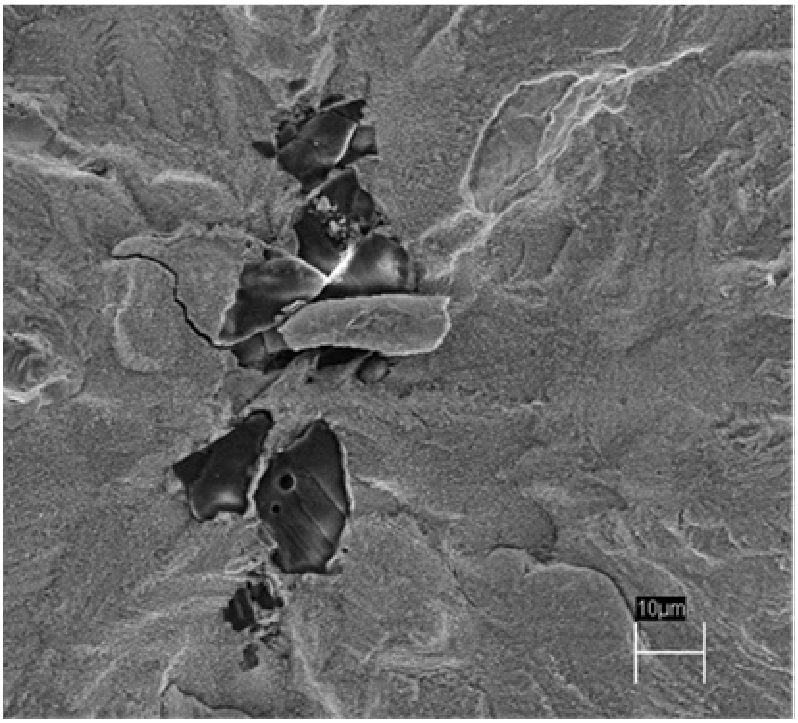

Figure 4.20. Higher magnification SEM image of the particle cluster shown in Figure 4.19.

a)

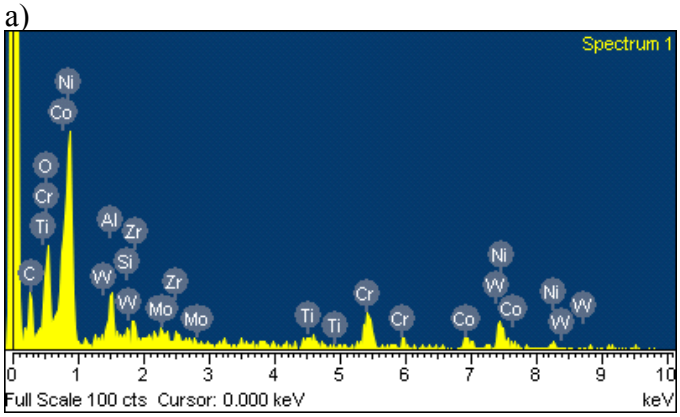

b)

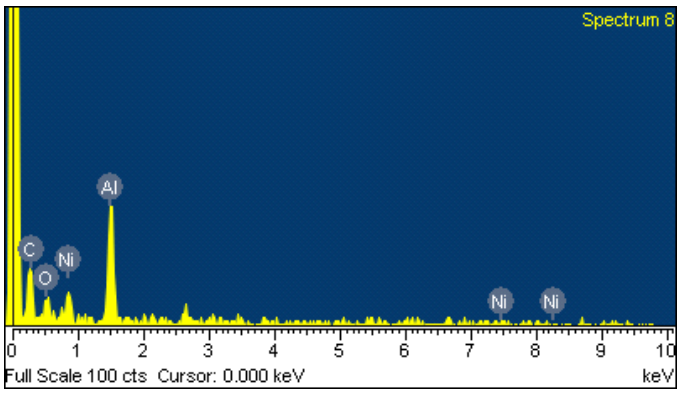

Figure 4.21. a) Baseline EDS spectrum obtained from the matrix of P 144, $\Delta\varepsilon = 0.79\%$, and
b) Spectrum obtained from a particle amongst the aluminum oxide particle cluster.

The fracture surface observations reveal that there are two very different crack initiation mechanisms contributing to the low cycle fatigue failures: slip band cracking and crack initiation from oxide inclusions. The dominance of one crack initiation mechanism over the other may help explain scatter in fatigue life. For example, Figure 4.22 shows a plot of the distance of the initiation feature to the low cycle fatigue specimen surface versus number of cycles to failure for P condition specimens tested with $\Delta\varepsilon = 0.66\%$ and $\Delta\varepsilon = 0.79\%$. The P condition specimens tested with $\Delta\varepsilon = 0.79\%$ exhibit a definite trend in this plot where the cycles to failure increases as the distance of the initiation feature to the

surface decreases. This decrease in life with increasing depth of the inclusion cluster may be explained because a crack initiated in the subsurface eventually forms an edge crack, the depth of which is dependent on the distance of initiation site to the specimen surface; deeper cracks have larger stress concentrations and will fail more quickly than shallower cracks. Also of note is that all three specimens tested at $\Delta\varepsilon = 0.79\%$ had cracks that initiated at an oxide inclusion. Two of the specimens tested at $\Delta\varepsilon = 0.66\%$ had crack initiation regions that originated at sites close to the specimen surface, while inclusion cracking was responsible for crack initiation in the third specimen. There is not a well-defined trend between these three data points as there is in the specimens tested with $\Delta\varepsilon = 0.79\%$, and this may be because there are two different mechanisms responsible for the crack initiation in the three specimens tested with $\Delta\varepsilon = 0.66\%$. Thus, it is necessary to explore models that can predict the likelihood and the cycles to failure associated with each mechanism.

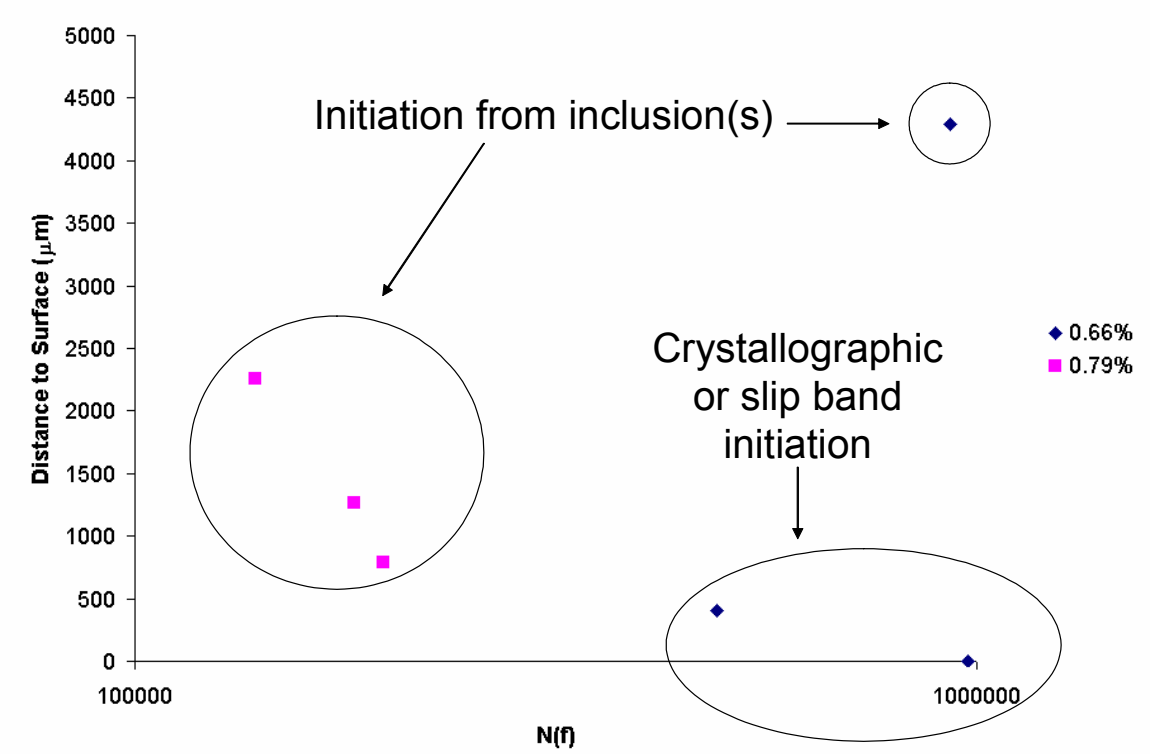

Figure 4.22. Plot of distance of the crack initiation site to the surface of the low cycle fatigue specimen versus number of cycles to failure among P condition specimens tested at $\Delta\varepsilon = 0.66\%$ and $\Delta\varepsilon = 0.79\%$ and 650ºC.

As described in the literature review section, Hyzak and Bernstein defined a transition strain range, above which surface initiation is more likely and below which subsurface nucleation becomes more likely. Again, their explanation is that surface initiation is more likely at higher strain ranges because of the high stress intensity associated with surface flaws and at low strain ranges, the highest stress intensity will be at the critical defect or "weakest link" of the material. An alternative explanation is that slip bands predominantly form on surface grains; so if the applied strain is not sufficient to cause significant damage during slip band formation, subsurface or inclusion crack initiation mechanisms become more probable. Caton *et al*. [2] conducted stress controlled fatigue experiments on Rene 88DT with maximum stress values ranging from 940 MPa to 1400

MPa and R=0.05, which is approximately equivalent to $\Delta\varepsilon = 0.5\%$ to $\Delta\varepsilon = 0.65\%$, and found that all failures except for one specimen tested with $\sigma_{max} = 1400$ MPa occurred in the specimen subsurface. These observations combined with the observations in this research where subsurface failures were observed up to $\Delta\varepsilon = 0.79\%$ suggests there is some validity in Hyzak and Bernstein's analysis applied to Rene 88DT and furthermore, that the transition strain range must be in the proximity of $\Delta\varepsilon = 0.66\%$ to $\Delta\varepsilon = 0.79\%$.

Caton *et al*. [2] also discovered that different trends fit the data for σ_{max} versus number of cycles to failure for failures originating from inclusions and from crystallographic planes. The failures from crystallographic planes exhibited longer lives than failures from inclusions; additionally, failures related to crack initiation from inclusions were only observed for maximum applied stress levels less than or equal to $\sigma_{max} = 1100$ MPa based on limited tests. If the transition strain range defines the likelihood of surface and subsurface crack initiation and also relates to slip band cracking versus inclusion cracking, then the data from the experiments performed by Caton *et al.* complements the data obtained from material conditions N and O in this research. Only slip band crack surface failures were observed in the N and O conditions, which were tested at higher strain ranges; this is consistent with the transition strain range. The P condition grain size is much smaller than the grain size of the N, O, and the material used by Caton *et al.*, making the formation of surface slip bands and subsequent slip band cracking more difficult; this could explain why subsurface inclusion failures are observed at relatively high strain ranges ($\Delta\varepsilon = 0.79\%$) in the P condition specimens. Thus, it may be concluded that the transition strain range and the competition in initiation mechanisms between

inclusion cracking and crystallographic or slip band cracking is dependent on the grain size. Models are explored to develop this concept and described later in this chapter.

In summary, low cycle fatigue tests were conducted with applied strain ranges varying between $\Delta\varepsilon = 0.66\%$ and $\Delta\varepsilon = 1.5\%$ on the three different material conditions. It was found that the there is a large amount of scatter in the fatigue cycles to failure and that the P condition specimens have longer lives than the specimens from conditions N and O. Two different crack initiation mechanisms were observed on the fracture surfaces of the specimens: initiation from plastic damage accumulation in slip bands on the specimen surface and initiation from inclusion clusters. Inclusion cracking was never observed in the N and O condition. The two different mechanisms may help explain the scatter in the low cycle fatigue lives. Models will be introduced in subsequent sections to associate the microstructural differences between the three conditions, namely the grain size, to crack initiation mechanisms and fatigue lives. The applied strain range must also be considered in these models.

4.2.3. Fracture Toughness and Fatigue Crack Growth Testing

A total of four fracture toughness experiments were conducted, 2 each on microstructure conditions N and O. Analysis of the data obtained during the first experiment on an O condition specimen revealed that slight unloading occurred throughout the test, and the load-displacement curve had a large degree of nonlinearity. The limits of the extensometer were reached shortly after the peak load of the experiment. A plot of load versus stroke (Figure 4.23) actually showed repeated loading and unloading during the

test more clearly than a plot of load versus crack tip opening displacement. Typically, unloading during the test is due to "pop-ins", where the crack extends a short distance and then arrests. Beach marks are present on the fracture surface (Figure 4.24), that coincide with a series of "pop-ins" and crack arrest events that occurred during the experiment. The fracture surface is also very flat and the entire surface is in the same plane as the starter notch; this is partly due to the presence of side grooves but is also an indication of negligible plasticity. The fracture surface observations supplement the argument that the crack repeatedly grows in an unstable manner and then arrests; it is not believed that stable crack growth occurs during the experiments. Figure 4.25 shows obvious partial unloading during the remote unloading of the specimen. However, unloading-loading occurred throughout the tests, which is observed after the linear region of the load versus load-line displacement diagram. In fact, it is speculated that this "pop-in" and the resultant crack growth behavior contributes to the nonlinear load versus load-line displacement behavior (Figure 4.25). In other words, the nonlinearity is due to crack growth and not due to plasticity in the specimens.

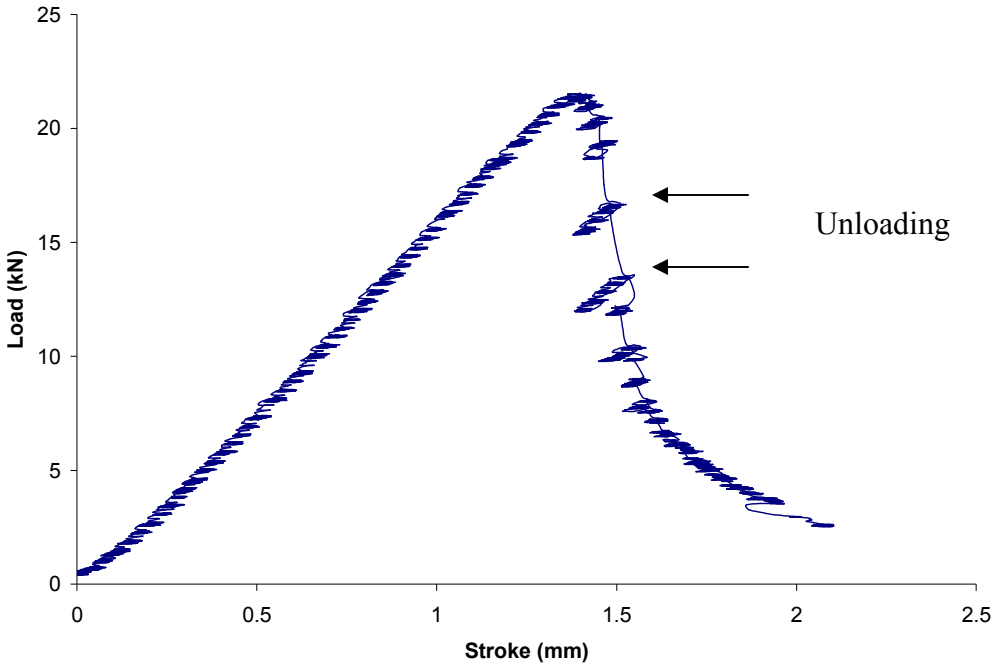

Figure 4.23. Plot of load versus actuator stroke, exhibiting partial unloading due to crack "pop-in" during a fracture toughness experiment at 650ºC.

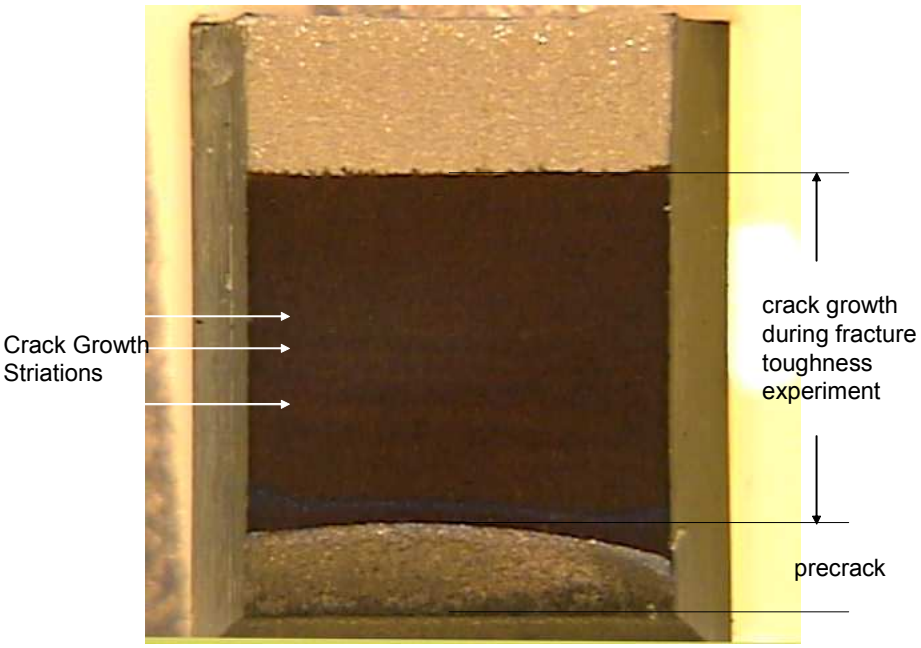

Figure 4.24. One half of the fracture toughness specimen fracture surface tested at 650ºC showing the precrack, crack growth during the fracture toughness experiment, and striations due to crack "pop-in".

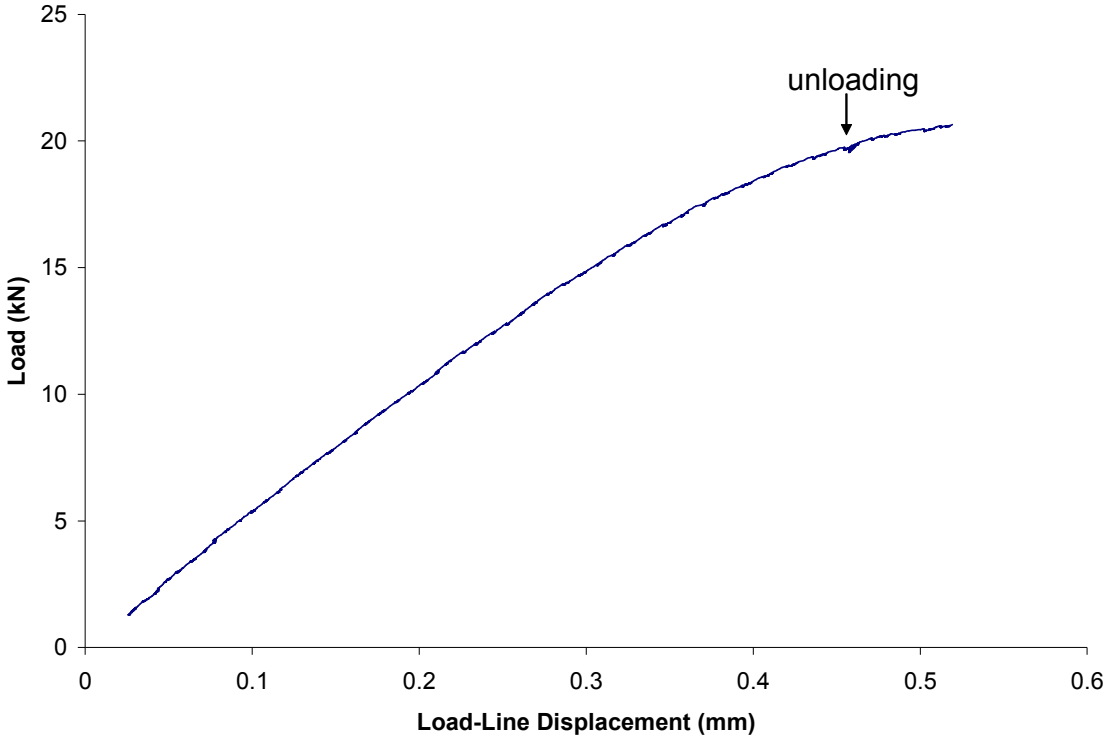

Figure 4.25. Load versus load-line displacement for a fracture toughness experiment conducted on a specimen from the microstructure condition N tested at 650ºC.

The subsequent fracture toughness specimens also exhibited "pop-in", and a series of clicking sounds were heard throughout the experiments, which were due to the crack propagating and then arresting. The repeated unstable crack growth and arrest during the experiments may be due to the hardening properties of the material. The tensile test results described previously exhibit a large degree of plastic hardening. This ability to harden can aid in arresting cracks as the stress and strain fields develop around the crack tip and result in a series of unstable crack growth and crack arrest increments as observed in these fracture toughness experiments.

After the initial experiment, which supplied the data for Figures 4.23-4.25, the rest of the tests were stopped short of or approximately at the maximum load. One experiment, performed on a specimen from the O microstructure condition, was stopped when the first clicking sound was heard; the specimen was then fractured at room temperature and the fracture surface was observed at low magnifications. There was no discernible high temperature crack growth on the fracture surface, but the final load was approximately the value of P_Q for other fracture toughness specimens so it is possible that the pop-ins were localized events that are not captured on low magnification photomicrographs, which did not provide sufficient resolution to reveal small amounts of localized crack extension along the crack-front.

ASTM Standard E 561 [51] on the standard practice for R-curve determination was used to develop crack growth resistance curves for the N and O fracture toughness specimens. A line was drawn on the load versus load-line displacement diagrams with a slope equal to 95% of the slope of the linear portion of the load versus load-line displacement curve. The intersection of this line with the curve provided the load value speculated to correspond to the precrack length; these values were used to calculate an effective modulus, E', from the value of E'Bv/P value corresponding to the known precrack length, where B is the effective specimen thickness and v/P is the compliance. The ASTM standard [51] states that E' should vary by no more than 10% from the actual value of the modulus; however, two of the tests resulted in E' values that were roughly twice the value of the actual elastic modulus. Further analysis showed that the compliance for these tests was twice the compliance of the other two experiments; it is

possible that a systematic error such as inconsistent extensometer voltage gains or excitation caused these unrealistic values. The load-line displacement data for these two experiments was corrected so the linear portion of the diagram had a slope similar to the other two data sets. R-curves, using crack lengths calculated from compliance measurements from various points on the load versus load-line displacement plots, were generated for three of the tests; the other test, which was stopped when the first click was heard, did not produce enough data to generate an R-curve. In order to determine a critical stress intensity value, K_C, constant load curves of stress-intensity versus crack length were drawn on the R-curve plot. When one of these K-applied curves has tangency with the R-curves, it defines a critical value of load and K_C that causes unstable fracture. Using this method, the value of K_C for both conditions N and O was determined to be approximately between 155-165 MPa*$m^{1/2}$ (Figure 4.26). This value was used to determine the number of cycles to reach a critical crack length or stress intensity in the finite element simulations described later in this section.

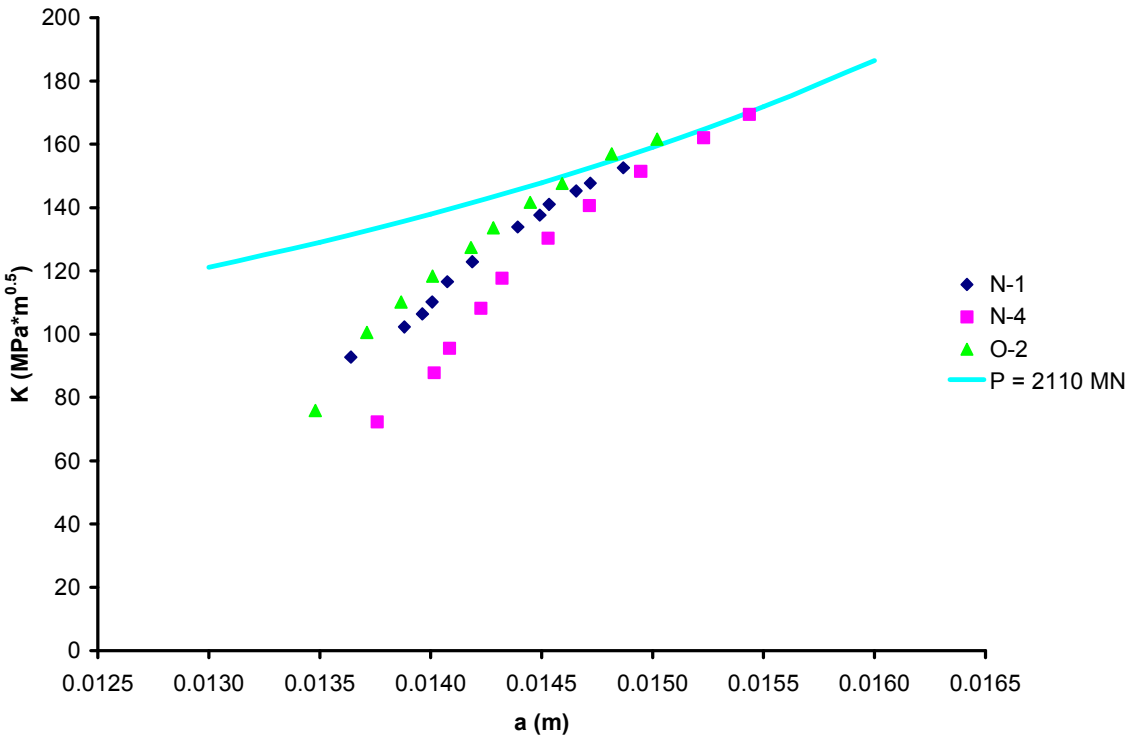

Figure 4.26. Crack growth resistance curves and a K-applied curve used to determine an approximate value of K_C.

The fatigue crack growth rates were measured at 650ºC in microstructure conditions N and O; once again, the behavior was very similar for the two conditions. In the initiation and short crack growth regimes of a fatigue crack, the rate and mechanism of the propagation is strongly related to the surrounding microstructure. When the crack becomes several times the size of the microstructure, the microstructure does not directly influence the crack propagation mechanism but the linear elastic or elastic-plastic properties of the material can be used to model stress concentrations around the crack tip and fatigue crack growth.

The parameter ΔK, the stress intensity range, has been established for characterizing crack growth rate in a material when the cyclic loading and crack geometry is such that the plastic zone around the crack tip is small compared to the elastic field in the rest of the part. The parameter ΔK is defined as the difference between the maximum and minimum stress intensity values during fatigue loading [49]. Then, the Paris Law can be used as a measurement and comparison of crack growth rates. However, when the size of the cyclic plastic zone is on the same order as the crack and part size, which can occur in high temperature testing or with large applied stress or strain ranges, ΔK cannot be used as a valid crack tip parameter. The J-integral, a path independent integral that accounts for large scale plasticity around the crack tip in monotonic loading, can be extended to fatigue conditions by considering only the loading portion of the fatigue cycle [52] (Figure 4.27). The following relationships, analogous to the Ramberg-Osgood relationship in monotonic conditions, may be used to define the relationship between cyclic stress and cyclic strain.

$$\Delta\sigma = \sigma_{max} - \sigma_{min} \tag{4.1}$$

$$\Delta\varepsilon = \varepsilon_{max} - \varepsilon_{min} \tag{4.2}$$

$$\frac{\Delta\varepsilon}{2} = \frac{\Delta\sigma}{2E} + \alpha'\left(\frac{\Delta\sigma}{2\sigma_o^c}\right)^{m'} \tag{4.3}$$

Then, ΔJ can be defined as

$$\Delta J = \int_{\Gamma} \Delta W dy - \Delta T_i \frac{\partial \Delta u_i}{\partial x} ds \tag{4.4}$$

$$\Delta W = \int_0^{\Delta\varepsilon_{ij}} \Delta\sigma_{ij} d\left(\Delta\varepsilon_{ij}\right) \tag{4.5}$$

where Γ is a counterclockwise path independent contour beginning on the lower crack surface and ending on the upper crack surface.

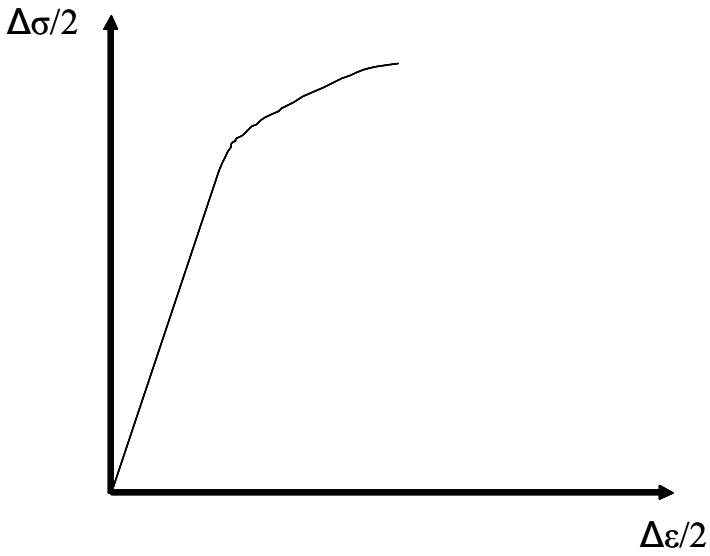

Figure 4.27. Loading portion of the cyclic stress-strain curve.

A relationship can be derived between ΔJ and the crack tip stress and strain range fields in a similar manner to the relationship derived between J and crack tip stress and strain fields. Also, ΔJ can be equated to the linear elastic parameter, ΔK, for linear elastic conditions using the relationship

$$\Delta J_{elastic} = \Delta K^2/E \qquad (4.6)$$

Since ΔJ includes both elastic and plastic components, it should be able to characterize fatigue crack growth rates for elastic and elastic-plastic conditions [52].

Thus far, ΔJ has not been widely used in fatigue crack growth relationships in nickel-base superalloys because of their high yield strengths even at elevated temperatures.

However, it will be shown later that ΔJ is an important and effective parameter for characterizing fatigue crack growth shape and direction. Methods of determining ΔJ using finite element methods will also be discussed.

The objective of the fatigue crack growth experiments was to determine a Paris Law fit for the da/dN versus ΔK relationship to be implemented in finite element analysis for semi-elliptical surface crack growth in round bars described later in this section. Tests were conducted at 650ºC with a frequency of 10 Hz. The data were analyzed using an incremental polynomial method, which is described in Annex X.1 in ASTM standard E647 [47], which utilizes a second-order polynomial to fit sets of seven or nine data points. The equation used in this research takes the form

$$a_i = b_0 + b_1 N_i + b_2 N_i^2 \tag{4.7}$$

where a_i and N_i are the instantaneous crack length and cycle number respectively, and b_0, b_1, and b_2 are regression parameters determined from a least squares fit to the data point sets. Figure 4.28 shows the results and compares them to literature data with R = 0.05 in a laboratory environment from Krueger *et al.* [1] and Caton *et al*. [2].

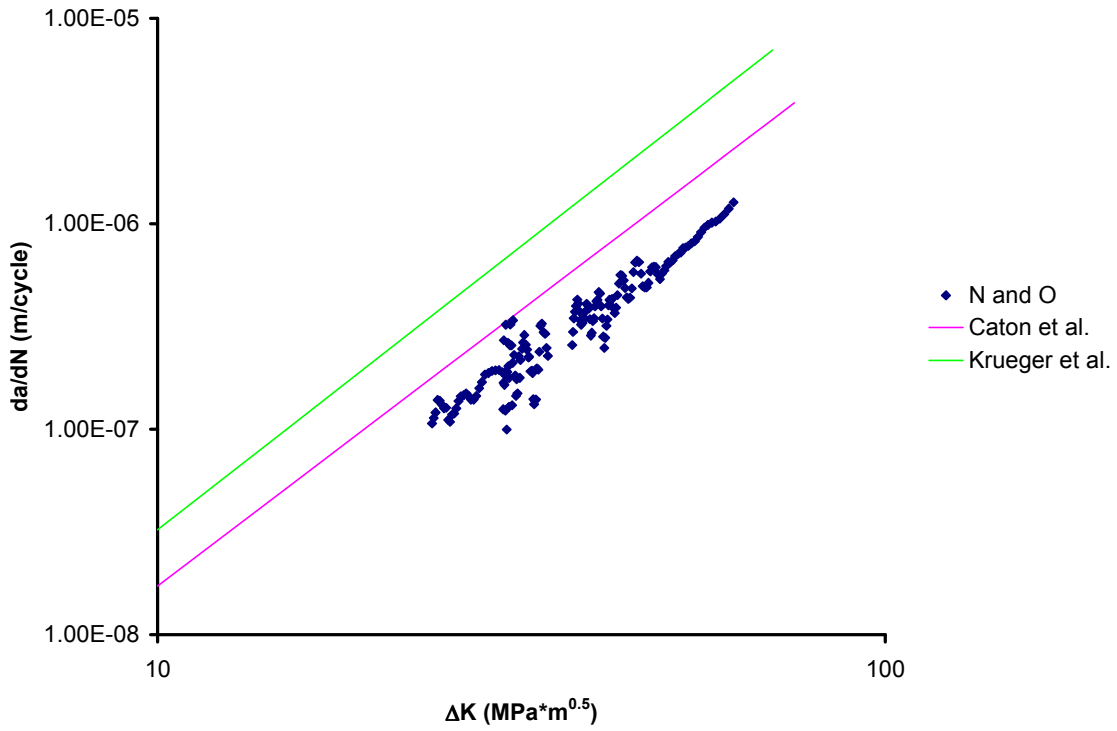

Figure 4.28. Crack growth data taken at 650ºC plotted on a log-log scale obtained from microstructure conditions N and O and compared to data from Krueger *et al*. [1] and Caton *et al.* [2].

The experiments conducted by Krueger *et al*. [1] were performed in air at 650ºC on Rene 88 with a similar grain size and approximately the same γ' size distribution. The testing frequency was equal to 0.33 Hz, which is much lower than the 10 Hz frequency used in these experiments; the lower frequency allows the effects of oxidation to have an influence on the crack growth rate, which explains why the crack growth rate for the Krueger *et al*. data is much higher than the crack growth rate for the N and O or Caton *et al.* conditions over the range of applied ΔK. The Caton *et al.* fatigue crack growth experiments were conducted with a frequency of 20 Hz but at a temperature of 593ºC, and the data lie closer to that for microstructures N and O. It must be added that although the grain size distribution for the material used by Caton *et al.* is approximately the same

as conditions N and O, the γ' size distribution is unknown. Thus, the small differences in the FCGR behavior could be related to microstructural differences and/or differences in the test temperatures.

The Paris Law fit to the N and O condition crack growth data results in the following relationship between crack growth rate in meters/cycle and the stress intensity range in MPa*m$^{0.5}$:

$$\frac{da}{dN} = 4.55 \times 10^{-11} \Delta K^{2.45} \quad (4.8).$$

Using the relationship between the elastic part of ΔJ and ΔK, the following equation is derived between da/dN in meters/cycle and ΔJ in MPa*m:

$$\frac{da}{dN} = 1.81 \times 10^{-4} \Delta J^{1.225} \quad (4.9).$$

4.3. Long Crack Growth Models Applied to Low Cycle Fatigue Conditions

The fatigue crack growth life predictions in this body of work are based on elliptical and semi-elliptical fatigue cracks initiated in round bars. Newman and Raju [3] used finite element models to determine closed form empirical solutions of the stress intensity for several crack and specimen geometries including an elliptical crack inside a rectangular plate (Figure 4.29) and a semi-elliptical crack on the surface of a plate (Figure 4.30) subject to normal loading. For crack sizes that are small compared to the diameter of a round bar, these stress intensity solutions for elliptical cracks in a plate may be good approximations for the actual stress intensities in the round bar geometry. The solutions

consider the crack aspect ratio (*a/c*), the crack depth (*a/t*), the plate width effects (*c/b*), and the location along the crack front (φ). Thus,

$$K_I = \sigma\sqrt{\pi\frac{a}{Q}}F \tag{4.10}$$

where Q is an elliptical shape factor and F accounts for the depth, aspect ratio, width, and location effects.

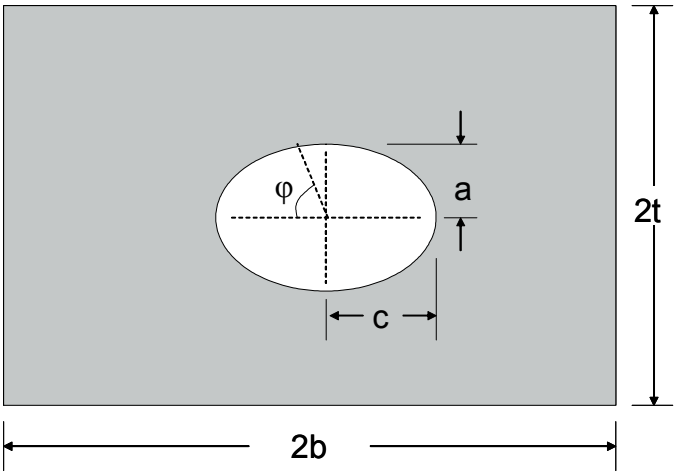

Figure 4.29. Configuration and parameters for an embedded elliptical crack in a plate [3].

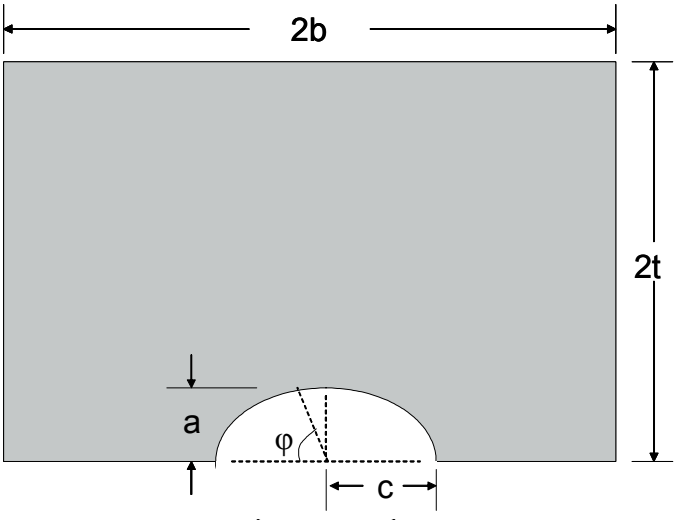

Figure 4.30. Configuration and parameters for a surface semi-elliptical crack in a plate [3].

Their finite element analysis was performed using linear strain and singularity elements around the crack front. A remote stress was applied and the nodal force variation along the crack front was output; these forces were used to compute the mode I stress intensity variation along the crack front. Quarter or half symmetry models were utilized with boundary conditions, where the normal displacements on the three planes of symmetry were set equal to zero. Solutions for the stress intensity where the crack intersects the surface could not be obtained.

The Newman and Raju solution for an elliptical crack in a round bar was applied to the P condition specimens tested with $\Delta\varepsilon = 0.79\%$ for subsurface crack initiation. The inclusions were modeled as the initial elliptical cracks, whose major and minor dimensions were based on an equivalent ellipse that would encompass the inclusions observed on the fracture surfaces; it was assumed that a crack of this equivalent size initiated on the first fatigue cycle. An example of the Newman and Raju geometry applied to the P specimens is shown in Figure 4.31. There are limits to the extent the Newman and Raju solution can be applied to an elliptical crack in a round bar, since the solution is based on an elliptical crack embedded in a rectangular plate. However, the plate width effects, which are described by a term, f_w, that is approximately equal to 1, are minor and the solution can be used for at least a portion of the crack growth in the P condition specimens.

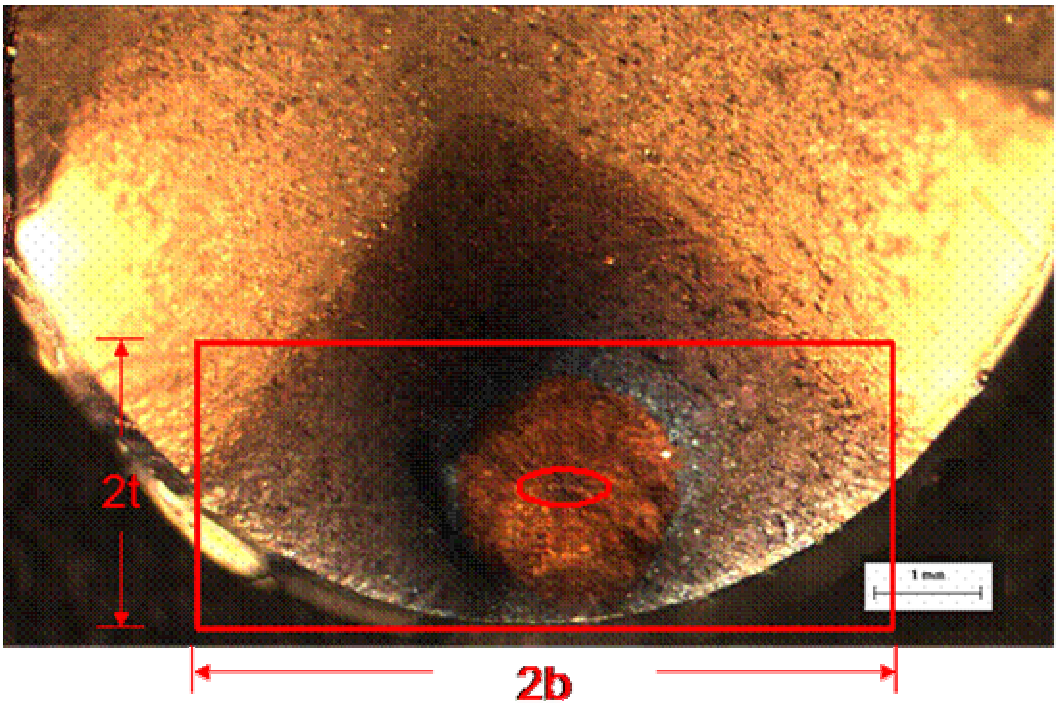

Figure 4.31. The Newman and Raju [3] solution for an elliptical crack in a rectangular bar applied to the round bar fatigue specimens from microstructure condition P.

A linear elastic analysis, as opposed to a nonlinear elastic analysis, can be used in these specific conditions for a number of reasons. SEM analysis shows that the crack growth region in the immediate vicinity of the crack initiation site is very facetted (Figure 4.19), indicating that the crack growth occurred under the constrained conditions of dominantly elastic behavior in the surrounding region. Crack growth where substantial plasticity was prevalent showed characteristics of a more ductile tearing mechanism. The remote applied strain for strain ranges less than $\Delta\varepsilon = 0.79\%$ results in a stress response in the material that is less than the cyclic yield stress for Rene 88DT at 650°C. Because of the anomalous strength behavior of nickel-base superalloys, their yield strength increases up to a certain point with increasing temperature [7]. The tensile data, described previously

in this section, shows that at 650°C, the yield and tensile strength are close to the peak values as a function of temperature. This phenomenon results in smaller plastic zone and creep zone sizes around the crack tip than most traditional alloys. A circular oxide pattern outlines the area of facetted crack growth in Figure 4.18. If it is assumed the crack grows in this pattern, the maximum estimated size of the plastic zone around the crack tip, which would be in plane stress conditions, is [52]

$$r_y = \frac{1}{\pi}\left(\frac{\Delta K_I}{2\sigma_{ys}^c}\right)^2 \qquad (4.11).$$

Using $2\sigma_{ys,c} = 1600\ MPa$ and $\Delta K = 40\ MPa*m^{0.5}$, which is a typical value for intermediate stress intensities as plasticity begins to increase in the remaining ligament between the crack front and specimen surface, the estimated size of the plastic zone is 0.2 mm. Examination of Figure 4.32 reveals that a ductile crack growth mechanism is not observed until the remaining ligament between the crack front and the edge of the specimen is approximately 0.1-0.2 mm. This is consistent with the fact that linear elastic fracture mechanics breaks down when the plastic zone size becomes comparable to a specimen dimension such as the width of the remaining ligament and is associated with very high stress intensities [52]. Thus, it appears that K or ΔK can adequately characterize crack growth in the vicinity of the crack initiation region for these P conditions, where the remote applied stress is less than the cyclic yield stress of the material.

The Newman and Raju solution was used to analyze the evolution of two points, lying on the major and minor axes of the ellipse, around the crack front as the remote stress

was applied over a large number of cycles. The initial dimensions of the cracks analyzed, including the distance of the initiation site to the surface and the associated number of cycles to failure, are shown in Table 4.8. For every cycle, the amount of crack growth in the direction of the major and minor axis was calculated, and a new ellipse was fit to the new crack dimensions. Figures 4.32 and 4.33 show the results of the analysis applied to specimens P 222 and P 122R. The predicted final crack shape is outlined on SEM images; in Figure 4.32, the inner ring is the predicted crack shape and the outer ring is an outline of the actual crack growth based on river pattern markings and elevation changes in the specimen.

Table 4.8. Summary of initial crack dimensions in P specimens exhibiting subsurface initiation.

Specimen	a (μm)	b (μm)	a/b	t (μm)	N_f
133	60	14	4.29	2260	139150
122R	7.5	36	0.21	1270	182200
222	22.5	12.5	1.80	790	197570

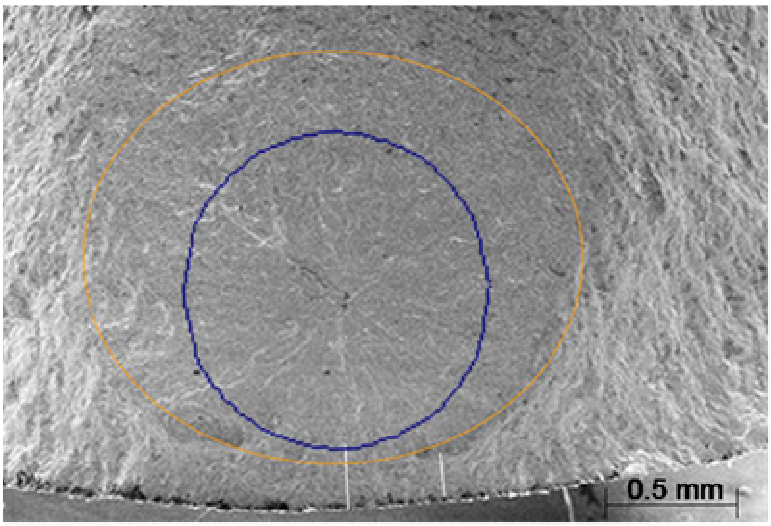

Figure 4.32. SEM image and corresponding prediction of the crack growth shape around the crack initiation region in specimen P 222.

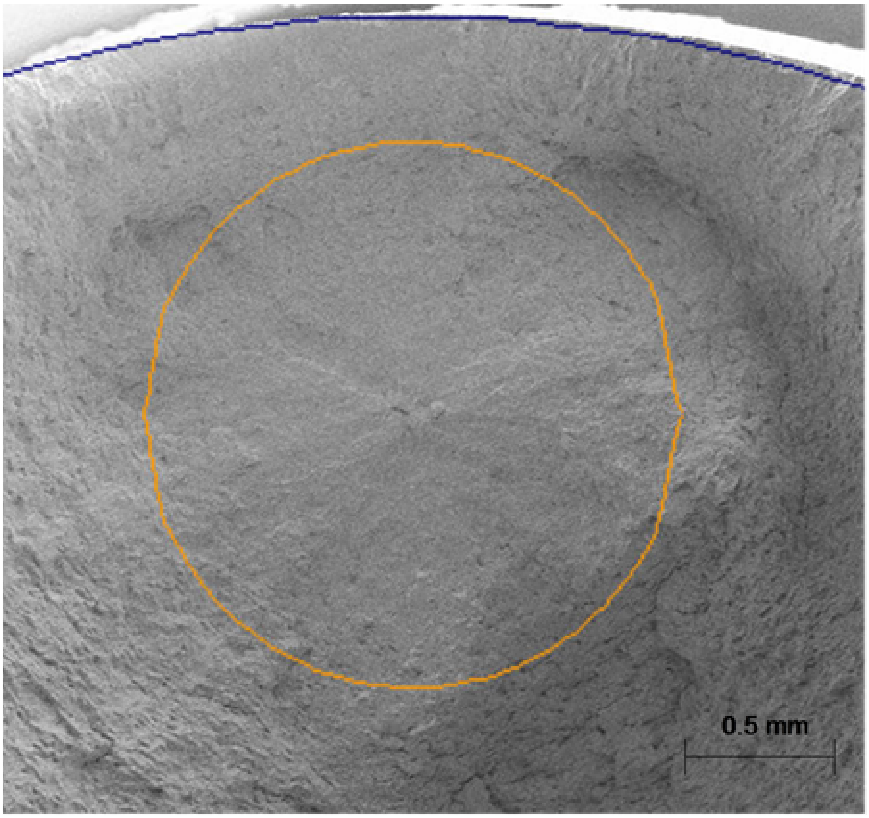

Figure 4.33. SEM image and corresponding prediction of the crack growth shape around the crack initiation region in specimen P 122R.

The deviation between the predicted and actual crack shape evolution may be due to the size of the plastic zone around the crack front approaching the size of the remaining ligament between the crack front and specimen surface as the crack grows and the stress intensity around the crack front increases. If this is the case, a ductile crack growth mechanism should be prevalent in these areas, while more facetted crack growth could be expected where the plastic zone size is small compared to the remaining ligament. Since the Newman and Raju solution predicts a negligible effect of specimen dimensions

except for a/t, the size of the remaining ligaments in the length and width dimensions could produce the disparity between the predicted and actual facetted crack growth shape. The predicted crack growth shape in P 122 R agrees reasonably well with the facetted crack growth shape in the specimen (Figure 4.33). However, in this case, the distance of the initiation site to the surface is much larger than in specimen P 222, where there is less agreement between the predicted and observed crack shape evolution; the distance of the crack initiation site to the surface in P 122 R is approximately 1.27 mm, while the distance of the initiation site to the surface in specimen P 222 is approximately 0.79 mm. The size of the remaining ligament in specimen P 122 R is large compared to the plastic zone size for a longer period of the crack growth, so the crack depth and width dimensions have less effect on the crack shape evolution than they do for specimen P 222.

Predictions of the final crack aspect ratio and crack length yields interesting trends. In both P 122R and P 222, the Newman and Raju solution predicts that the crack aspect ratio stabilizes at approximately a/c = 1. In specimen P 222, the original aspect ratio was a/c = 1.8, while the original aspect ratio in P 122 R was a/c = 0.21; thus, the crack evolves to a/c ~ 1 from two extreme aspect ratios. The predicted final crack dimension, a, for P 222 is approximately 590 μm before it breaks through a remaining ligament with a depth of approximately 200 μm. The predicted final crack dimension, a, for P 122R is approximately 890 μm before it breaks through a remaining ligament with a depth of approximately 380 μm. The predicted final crack dimension, a, for P 133 is approximately 890 μm before it breaks through a remaining ligament with a depth of

approximately 1370 μm. The number of cycles to reach these final crack lengths is 8120, 8630, and 6930 for P 222, P 122R, and P 133 respectively. These values seem to be associated with the starting crack dimension, a, as specimen P 133 has the largest initial crack size and the least number of cycles before high stress intensities are encountered accompanied by substantial plastic deformation in the remaining ligament, and P 122R has the smallest initial crack size and the most number of cycles before substantial plasticity is prevalent; a similar trend exists for the original crack aspect ratio and number of cycles of facetted crack growth. Table 4.9 summarizes the final predicted crack dimensions at the point where there appears to be significant plasticity in the remaining ligament and also the number of cycles to reach this point. At this point, a J-integral limit load solution may be a more appropriate method to evaluate stress intensity at the crack front closest to the specimen surface.

Table 4.9. The predicted final crack dimensions and corresponding number of cycles to reach these dimensions for the P specimens exhibiting subsurface crack growth.

Specimen	N	a (μm)	C (μm)	Ligament Depth (μm)
133	6930	890	865	1371
122R	8630	890	870	380
222	8120	590	576	200

Though the Newman and Raju result can predict the crack shape evolution within a fair degree of accuracy, it conservatively predicts the number of cycles for the crack to reach a size where it breaks through the smallest remaining ligament. Table 4.10 shows that the predicted number of cycles for a crack to grow to the point where it should break through the smallest remaining ligament is less than 10,000 if it is assumed that the crack

initiates around the inclusion on the first cycle. A J-integral finite element analysis, which will be described later in this section, predicts that the number of cycles to failure is less than 2,200 for a semi-elliptical surface crack in a round bar with a/t = 0.2 and $\Delta\varepsilon$ = 0.79%. The actual number of cycles to failure for these specimens is between 140,000 and 200,000, so the fracture mechanics solutions for long crack growth are vastly underestimating the number of cycles to failure. The results obtained from the Newman and Raju solution are similar to scatter observed by Byrne *et al*. [28] in a similar analysis, which was described in Chapter 2. Therefore, there is a missing link in the analysis in the crack initiation stage of fatigue. Possibly, the crack does not initiate around the inclusion on the first cycle but instead the material gradually debonds around the inclusion over several cycles until an elliptical crack is formed. If an elliptical crack forms around an inclusion, the dimensions are only slightly larger than the size of the microstructural feature, the grain size, which is approximately 6 μm. Thus, there may be a short crack growth stage of fatigue after crack initiation, and crack growth rates for short crack growth are typically faster than they are for long crack growth; this could mean that the crack growth stage of the fatigue life is an even smaller portion of the total fatigue life than the crack growth models predict.

The stress intensity variation of a semi-elliptical crack in a round bar (Figure 4.34) was examined by Carpinteri [4] and others [53, 54] for tensile and bending loads, again using a finite element technique. Specifically, the effect of the crack aspect ratio (a/c), the maximum crack depth (a/D), and location along the crack front (ζ/h) were considered. The round bar diameters, D, varied between 20-50 mm, which are much larger than the

round bar specimens used in this research. The crack aspect ratio was varied between a/c = 0 (straight crack front) to a/c = 1 (circular crack front). Three dimensional finite element meshes were generated using 20-node isoparametric elements, with the midside nodes shifted to the quarter point positions along the crack front and element boundaries and nodal points lying along straight lines normal to different locations along the crack front; symmetry conditions were also used (Figure 4.34). After defining the linear elastic material properties and applying a remote load, the resulting stress fields were used to determine the stress intensity and dimensionless stress intensity factors.

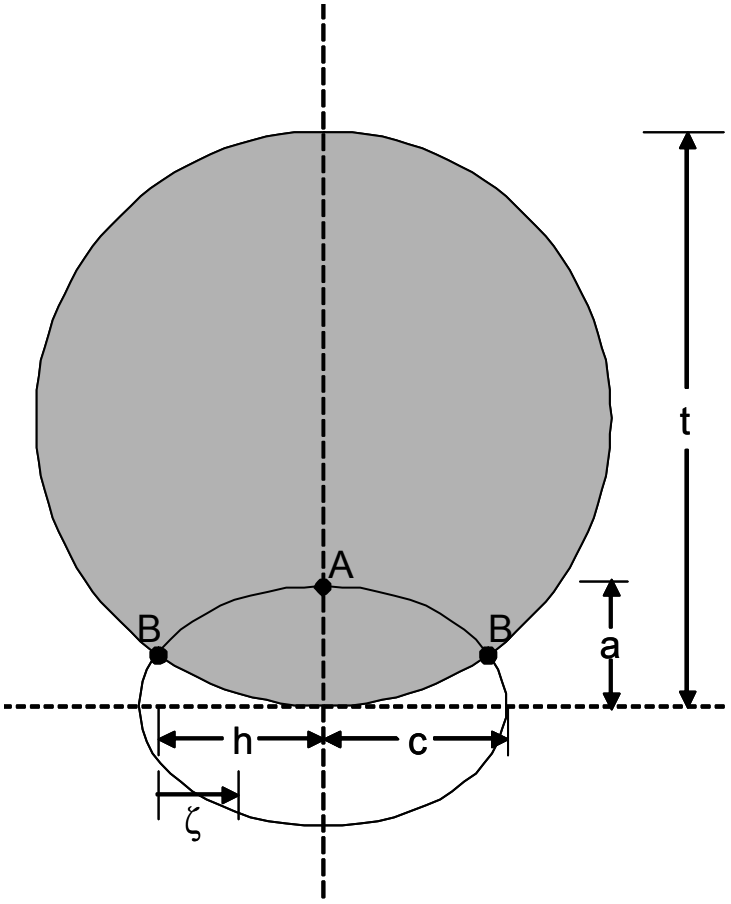

Figure 4.34. Crack configuration for a semi-elliptical crack in a round bar [4].

Several variations of aspect ratio and crack depth configurations were examined with particular attention focused on point A ($\zeta/h=1$) and point B ($\zeta/h=0.1$). Figure 4.35 is a plot of the dimensionless stress intensity factor versus the normalized coordinate ζ/h for cracks of different aspect ratios subject to tension loading and $a/D = 0.3$. For a/c greater than a critical aspect ratio value, the maximum stress intensity occurs at point B, while for a/c less than the critical value, the maximum stress intensity occurs at point A. Finite element researchers, including Carpintieri, discovered that this value is between a/c = 0.6-0.7. If a/D is increased, the variation in stress intensity across the crack front becomes more pronounced. Additionally, a critical value of crack depth, which defines whether the maximum value of stress intensity occurs at point A or B, decreases as crack aspect ratio increases. The location of the maximum value of stress intensity can be used to deduce how the crack shape changes as the crack grows. If the maximum stress intensity occurs at point A, the crack aspect ratio should increase; conversely; if the maximum stress intensity occurs at point B, the crack aspect ratio should decrease.

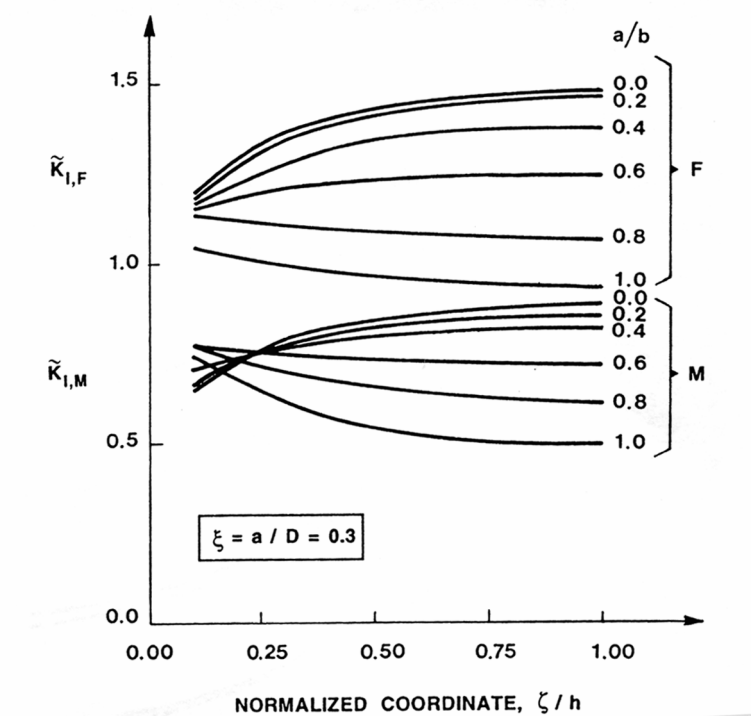

Figure 4.35. Normalized stress intensity factor versus crack tip location for tension and bending [4].

As mentioned previously, the Newman and Raju result for the stress intensity of a semi-elliptical crack on the surface of a plate should be able to approximate the stress intensity of a semi-elliptical crack in a round bar when the size of the crack is small compared to the diameter of the round bar. Third order polynomial relationships were fit to tabulated Carpintieri results at point A for the normalized stress intensity factor of different crack aspect ratios and depths. Then, stress intensity versus crack depth was calculated for a/c = 0.5 and compared to similar results obtained from the Newman and Raju stress intensity relationships (Figure 4.36). The remote stress used for the calculation was 1620 MPa. The results obtained using the two approaches are very similar for all the values of crack depth.

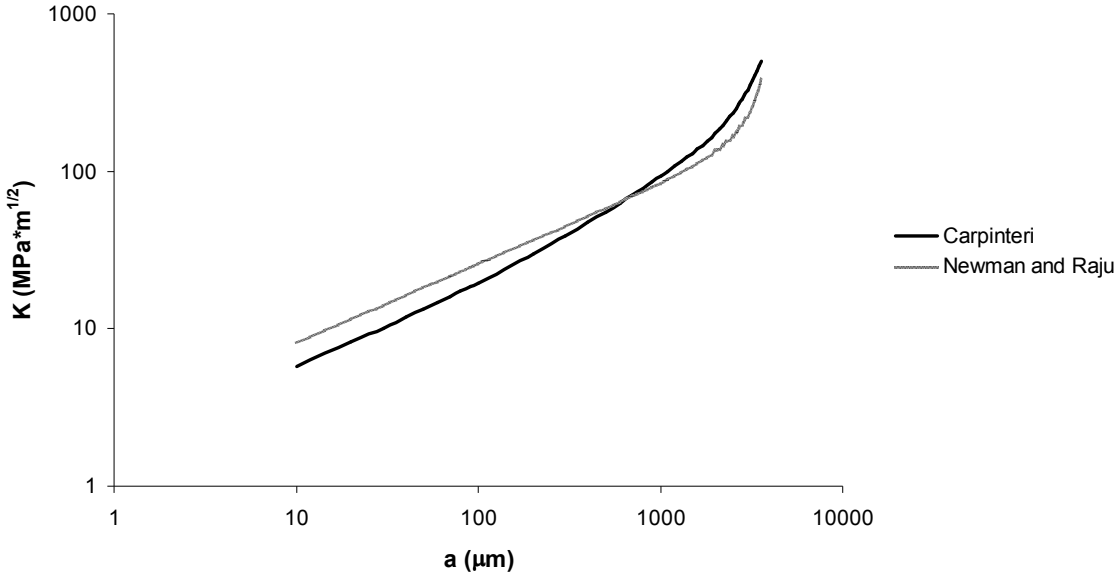

Figure 4.36. Stress intensity versus crack depth at point A using relationships obtained from Carpintieri [4] and Newman and Raju [3] analyses.

In order to assess surface crack length and shape evolution that simulates data from the low cycle fatigue experimentation, finite element modeling was performed using ABAQUS 8.4 finite element software. Previous studies, such as those by Newman and Raju [3] and Carpintieri [4], obtained the linear elastic stress intensity parameter, K, around the crack front. Carpintieri [55] used those values and a da/dN vs. ΔK relationship to predict crack shape evolution during fatigue cycling for crack aspect ratios less than one. In this study, semi-elliptical cracks were observed with aspect ratios greater and less than one, which has not been previously addressed by finite element studies of semi-elliptical cracks in round bars; crack aspect ratios greater than one were observed when cracks initiated in the subsurface of the specimens and then formed semi-elliptical cracks when they broke through the remaining ligament of material between the crack and specimen surface.

Low cycle fatigue testing was sometimes performed under elastic-plastic conditions as described in Section 4.2.2, so an analysis using only K or ΔK may not be complete.

Thus, ABAQUS was employed to obtain J-integral values around the crack front and predict crack growth and shape evolution. Plots of $\Delta\sigma$ versus $\Delta\varepsilon$ were obtained from the low cycle fatigue experiments; then, the Ramberg-Osgood constants could be calculated. The Ramberg-Osgood constants along with the modulus and cyclic yield strength can be directly input into the ABAQUS program as accurate material parameters. A 3-D model was built to simulate the round bar fatigue specimen using quadratic, isoparametric, 20 node elements, which enable an accurate study of the stress and strain fields throughout the model. Because the J-integral is a measure of energy within a relatively remote boundary encompassing the crack tip, the use of elements with nodes at the quarter points of the edges to account for the stress singularity at the crack tip is unnecessary. Due to the symmetry of a fatigue crack in a round bar, only half of the round bar was modeled. It is possible to use the symmetry to only model a quarter of the specimen, but it is difficult to obtain accurate values of stress intensity at the edges of the model [3, 4] and thus, obtaining the value of stress intensity at the center of the crack tip would be challenging.

In order to avoid a vast number of finite element experiments that simulate every observed crack shape and length observed in experiments, a matrix of finite element experiments was developed so that estimations could be made for the relationships between the rate of crack growth, the crack length (a/t), and the crack shape (a/c) at various applied stresses or strains. The matrix included crack lengths, a/t, from

approximately 0.1 to 0.3 and crack aspect ratios, a/c, from 0.5 to 1.5. Measurements taken directly from the fatigue fracture surfaces were used as the basis for deciding the geometries of the finite element models and for subsequent comparison with the model results; the loading conditions and specimen geometry input into ABAQUS were the same as those used in experiment. For each finite element experiment, the J-integral stress intensity was acquired around the crack front with nodes always placed at the deepest point of the crack and at a 45° angle from the center of the crack on the surface (Figure 4.37); the relationships between the rate of crack growth and crack geometry parameters were determined at these points. A side and cross-sectional view of the finite element model are shown in Figure 4.38; the elements are shaded corresponding to different levels of Von Mises stress and the red shade, corresponding to the highest stress intensity, outlines the fatigue crack.

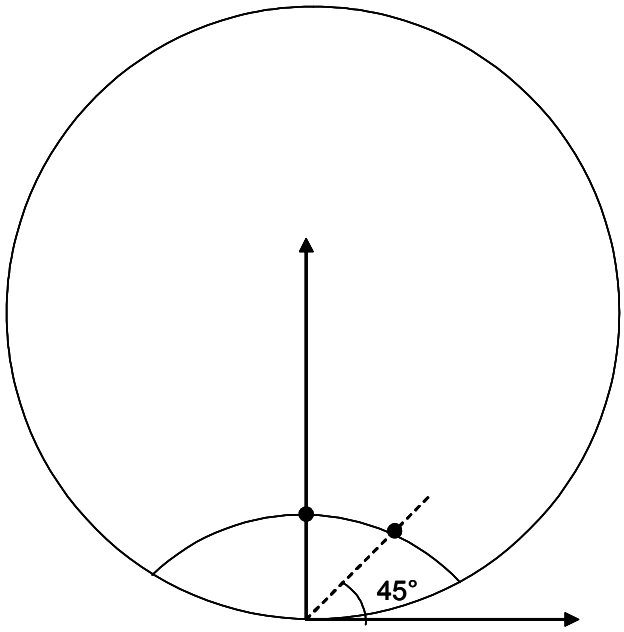

Figure 4.37. Cross section of the round bar fatigue specimen. The black points indicate the focal points for the J-integral and crack growth analysis.

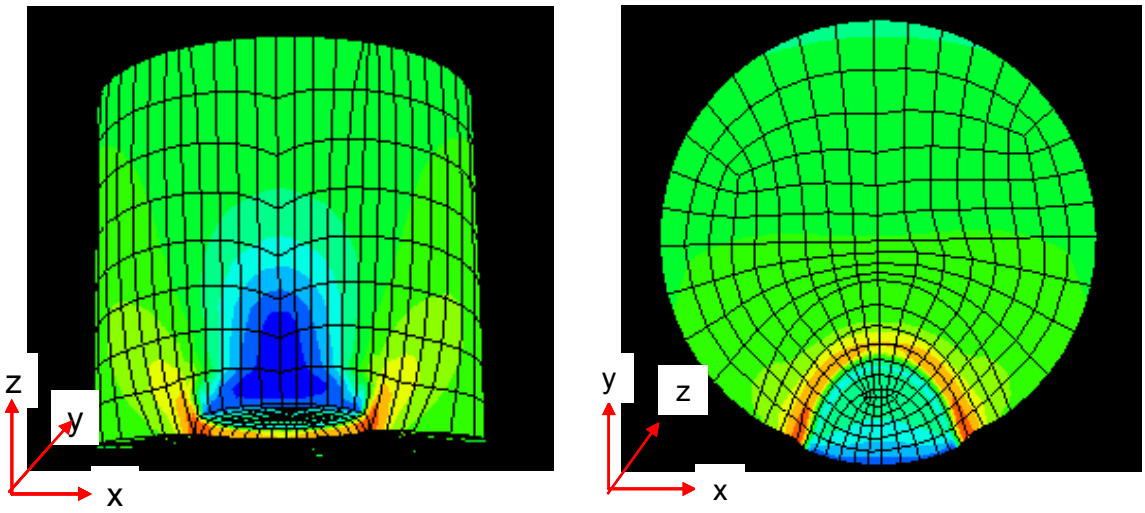

Figure 4.38. Side (left) and cross-sectional (right) image of the finite element models of a semi-elliptical crack in a round bar fatigue specimen.

Verification of the model was again performed by comparing linear elastic solutions obtained from the finite element analysis to solutions obtained by Newman and Raju for semi-elliptical surface cracks in rectangular bars (Figure 4.30). Figure 4.39 shows a comparison between the J-integral results obtained from both the Newman and Raju and finite element analyses for a/t = 0.2 and a range of a/c values using the P specimen geometry; the figure compares values obtained at the center of the crack and 60 degrees from the crack tip. The linear elastic values and trend from the finite element analysis are very similar to the those predicted by the Newman and Raju solution. This is significant because it validates the finite element analysis with known solutions and also further demonstrates that the Newman and Raju solutions can be used to approximate semi-elliptical surface cracks in round bars in linear elastic conditions even though their solution is for a semi-elliptical crack in a rectangular bar.

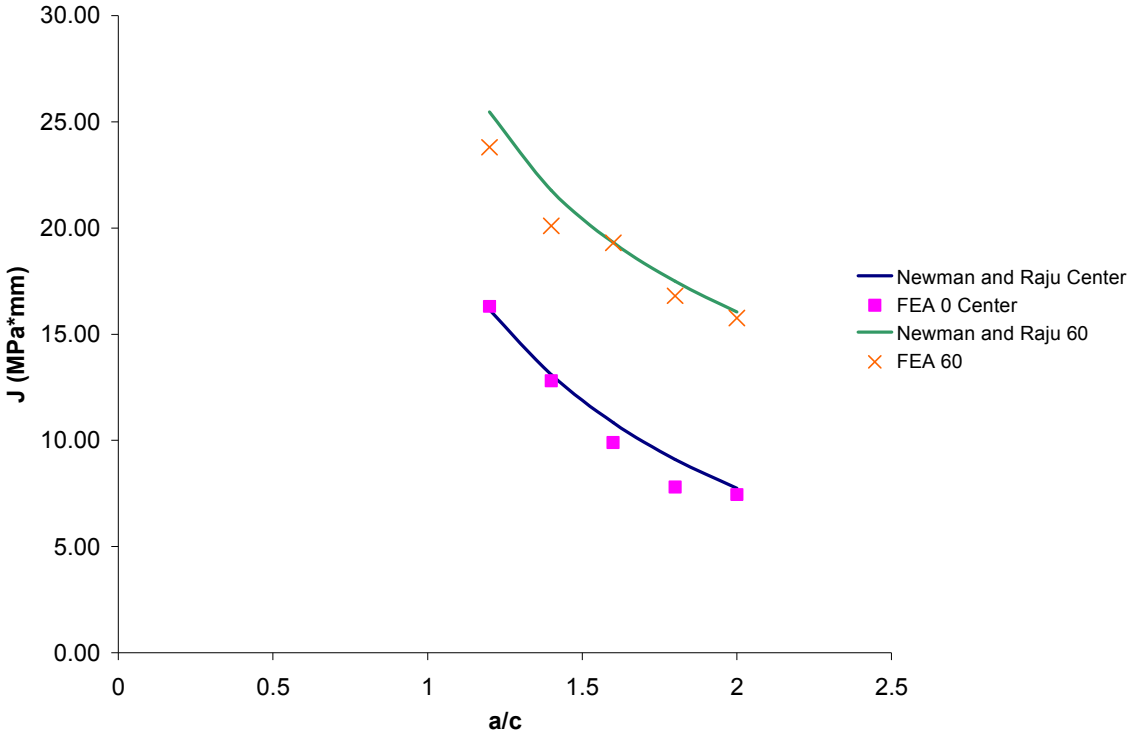

Figure 4.39. Linear elastic J-integral comparison between values obtained from the Newman and Raju solution and the finite element analysis in this research.

To predict long crack fatigue life and crack length and shape evolution, a mathematical fit of the ABAQUS data for the J-integral dependence on a/t and a/c was found for both the N and O and P round bar geometries for $\Delta\varepsilon = 0.66\%$ and $\Delta\varepsilon = 0.75\text{-}79\%$, which are the fatigue conditions with the longest lives; another fit was obtained for $\Delta\varepsilon = 0.94\%$, a more nonlinear elastic plastic condition. The mathematical fit was obtained by examining the dependence of the J-integral on *a/t* and *a/c* individually while keeping the other parameter constant and then combining the expressions and finding the best fit by changing the expression constants. The J-integral dependence on *a/t* can be fit using an exponential term, and the dependence on a/c can be fit with a second order polynomial. The resulting expression is:

$$J = e^{\left(C_1 \frac{a}{t}\right)} \left(C_2 \left(\frac{a}{c} \right)^2 + C_3 \left(\frac{a}{c} \right) + C_4 \right) \tag{4.12}$$

where C_1, C_2, C_3, and C_4 are constants. An expression of this form was derived for various applied remote stresses that simulate the experimental conditions. However, it was necessary to derive the expression for the N and O conditions separately from the P condition because the finite element solutions show a strong dependence on the diameter of the round bar specimens. For example, the J-integral value at the center of the crack tip for a/t = 0.25 and a/c = 1.1 in the N and O geometry is 26.6 MPa*mm, while the J-integral value is 43.7 for the P geometry and similar a/t and a/c values. Much of the literature finite element research on semi-elliptical cracks in round bars has analyzed varying crack sizes in a round bar of constant diameter, so the combined effect of a/t and the absolute crack length, a, has been largely unexplored in round bar specimens. Data was not available to extract such a solution in this research, so the expression in equation 4.12 was used to model the N and O and P geometries separately. Additionally, the above equation was fit to each remote applied strain.

Using the known relationship between the fatigue crack growth rate and ΔJ obtained from fatigue crack growth testing described previously in this chapter, the data fit relationship for the J-integral at the crack tip and at the 45º location can be used to predict crack growth and the shape change. It was found that starting with various values of crack length and crack aspect ratio that a/c converges to a value between 0.85-0.95 before the critical value of the J-integral is reached when the starting crack length is relatively small (Figure 4.40). This is true for both the N and O and P geometries and for Δε = 0.66% and

$\Delta\varepsilon$ = 0.75-79%. As noted previously, a similar trend was reported by others performing finite element analyses on semi-elliptical surface cracks in round bars in linear elastic conditions, but they found the stable value of a/c to be between 0.6 and 0.7 [4, 53, 54]. Again, the difference in the stabilized value in this analysis compared to literature analysis may be due to the allowance of plasticity in the J-integral models. If the starting crack length is larger than a/t=0.1-0.2, than the stable aspect ratio value may not be reached before the crack grows to a critical size. This is especially important when considering semi-elliptical surface cracks that form as a result of a subsurface crack breaking through the surface, because the initial crack aspect ratio is likely greater than one and the initial surface crack is relatively large in size.

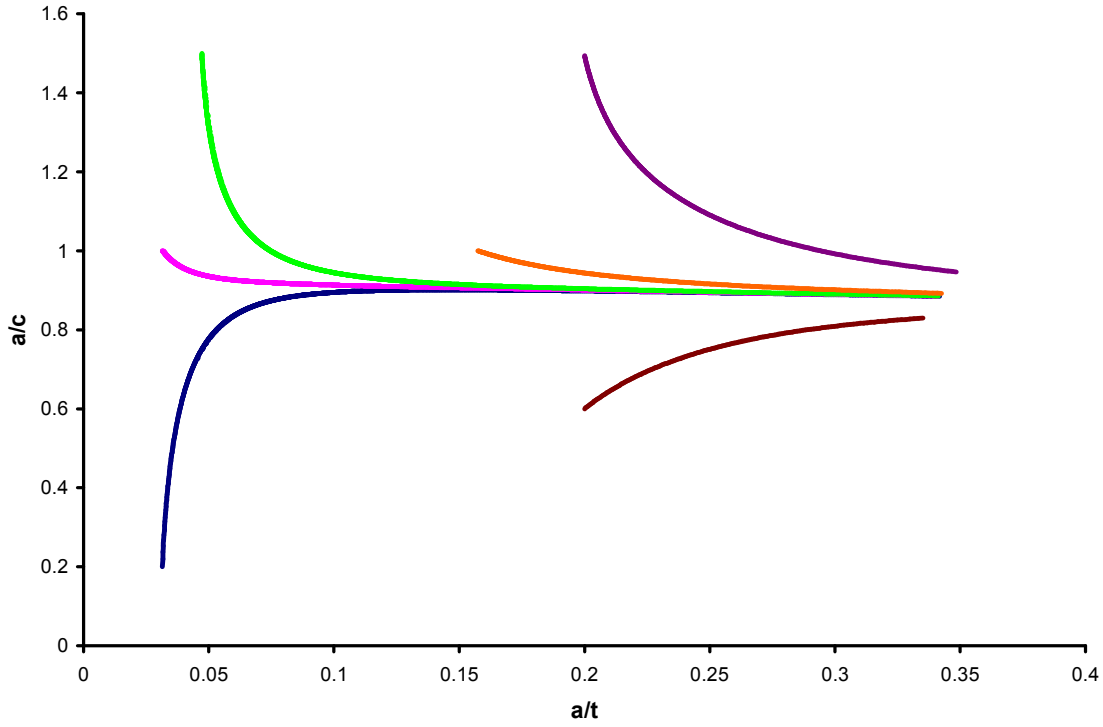

Figure 4.40. Plot of crack aspect ratio versus crack length evolution using the data fit obtained from ABAQUS analysis for various starting values of each parameter.

The mathematical expressions relating crack length, aspect ratio, and J-integral can be used to estimate the number of cycles necessary to reach a critical crack length. The solutions do not consider local microstructural effects on the crack, so the starting crack size for these predictions must be large relative to the largest microstructural feature, which is the grain size. For this analysis, the starting crack size for the N and O conditions is approximately 200 μm if the largest grain size on a lognormal distribution is approximately 40 μm, and the starting crack size for the P condition is approximately 60 μm if the largest grain size is approximately 12 μm. Using the data fit from the finite element analysis for the N and O conditions and $\Delta\varepsilon = 0.75\%$, the number of cycles to failure for a starting crack length of 200 μm and a/c = 1 in the round bar geometry used in the low cycle fatigue experiments is approximately 2,150. The total fatigue life for the N and O condition specimens tested with $\Delta\varepsilon = 0.75\%$ was between 4,700 and 11,000 cycles. It appears that up to half of the total fatigue life is spent in the long crack growth stage, so a considerable portion of the fatigue life takes place in the crack initiation and short crack growth stages. If the same analysis is performed using a starting crack size based on the P condition, the number of cycles to failure is approximately 2,450. The experimentally observed number of cycles to failure for the P condition specimens tested with $\Delta\varepsilon=0.79\%$ is 140,000 to 200,000, so the long crack growth life appears to be a much smaller portion of the P condition specimen lives than it is for the N and O conditions. Similar results were attained for $\Delta\varepsilon = 0.66\%$ (Table 4.10), except that it appears the long crack growth life is an even smaller fraction of the total fatigue life compared to the results from $\Delta\varepsilon = 0.75\%$. An analysis of $\Delta\varepsilon = 0.94\%$ for the P condition predicts

approximately 1,000 cycles in the long crack growth regime, while the experimentally observed cycles to failure varies between 8,000 and 58,000. It is speculated that as the applied strain range increases, the long crack growth life becomes a larger fraction of the total fatigue; this assertion will be complemented by a discussion exhibiting that crack initiation occurs much more readily and homogeneously throughout the material at larger strain ranges. It may also be concluded that the crack initiation and short crack growth resistance in the P condition is much greater than for the N and O condition; the values in Table 4.10, from the finite element predictions, underscore this assertion in a summary of the predicted results. In the next section, models will be developed to describe the crack initiation and short crack growth resistance based primarily on the grain size of the material.

Table 4.10. Summary of results obtained from the fitted equations based on FEA experiments.

				Based on Fitted Equations			
Condition	**$\Delta\varepsilon$**	**a_o (mm)**	**c_o (mm)**	**a_f (mm)**	**c_f (mm)**	**N_f predicted**	**N_f exp**
N&O	0.66%	0.2	0.2	2.52	3.03	3,175	17,000-98,500
N&O	0.75%	0.2	0.2	2.17	2.45	2,140	4,700-11,100
P	0.66%	0.06	0.06	3.53	4.08	4,450	491,000-977,000
P	0.79%	0.06	0.06	2.94	3.41	2,450	140,000-197,500

The fitted equations can also be used to compare to the crack aspect ratio evolution observed experimentally. Figure 4.41 shows fatigue striations used to directly measure the crack shape evolution on the low cycle fatigue specimens. Measurements of the final crack length on an O condition specimen tested with $\Delta\varepsilon = 0.75\%$ showed that the final

crack length was a/t = 0.43 compared to the predicted value of 0.34 from the FEA data fit relationship, and the final aspect ratio was a/c= 0.93 compared to the predicted value of approximately 0.88. The criteria for failure in the ABAQUS analysis was when a J-integral value on the crack tip equaled the critical J value obtained from an R curve which was generated from the fracture toughness experiments. However, the fracture toughness experiments also demonstrated that the material has the ability to repeatedly arrest unstable crack growth due to significant hardening of the material around the crack tip. Thus, the predicted value is probably fairly conservative compared to experimentally measured values of final crack length because the material has the ability to allow increments of unstable crack extension. The disparity in the crack aspect ratio measurements compared to the predictions may arise from the nature of the actual crack growth. As described previously, large shear lips form on the edges of the low cycle fatigue specimens, so there is a combination of mode I and mode II loading in these regions; thus, the rate of crack growth toward the 'c' axis will be slower than the predictions from the model based purely on a mode I analysis. Because of the complexity of modeling mixed mode fracture which would require a complex crack geometry, shown in Figure 4.42, it was postulated that the finite element predictions for crack shape evolution would vary from experimental observations. Nonetheless, the observed final crack aspect ratio is much closer to the prediction based on the nonlinear elastic J-integral analysis than the predictions from literature for linear elastic conditions, which predict a final aspect ratio between 0.6-0.7.

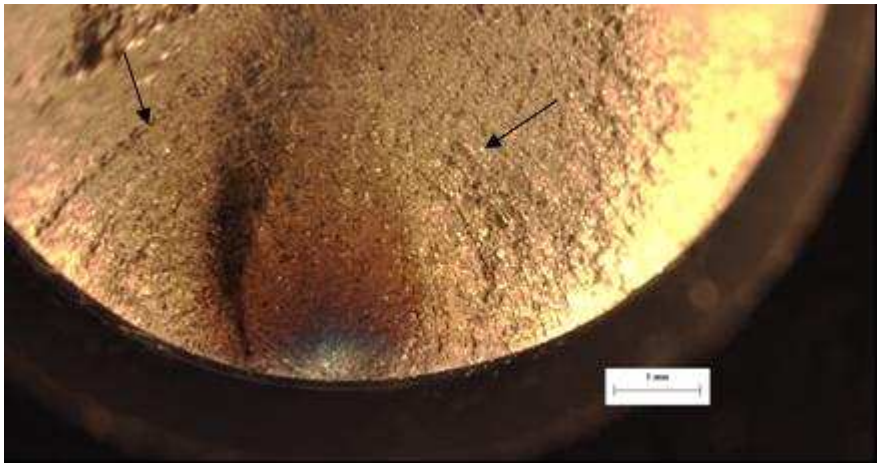

Figure 4.41. Fatigue striations on a specimen tested with a strain range of 0.66% at 650ºC.

Figure 4.42. Fatigue fracture surface from a specimen tested with a strain range of 0.66% at 650ºC.

Fatigue crack striations were easily observed on two of the P condition specimens, P 155 and P 233, tested at $\Delta\varepsilon = 0.66\%$, and they provided at least a few experimental data points for the crack aspect ratio evolution versus the crack depth. The two specimens exhibited two different crack initiation mechanisms: P 155 failed from a crack on the surface and P 233 failed from a subsurface crack starting at a small inclusion. It is not known whether the long crack growth and aspect ratio evolution is affected by the crack initiation mechanism, but predictions from the data fit equations indicate this possibility. Figure 4.43 shows experimentally observed measurements of a/c versus a/t for P 155 and the predicted a/c versus a/t values when the initial crack has the depth and aspect ratio of the first set of experimental data points. Again, the data fit equations predict the aspect ratio changes more quickly than experimental observations demonstrate, which was discussed previously, but the predicted values deviate approximately 5% or less from the observed values throughout the range of observation. The predicted value of the final crack length is smaller than the final experimental observation, which again could be due to the crack growth resistance of the material. Figure 4.44 shows another plot comparing the experimentally measured and predicted crack aspect ratios versus crack depth for P 233. The deviation between experiment and prediction is far greater for this case; there is a difference of up to 15% over the range of experimentally measured values and there seems to be more disparity between the experimental and predicted trends.

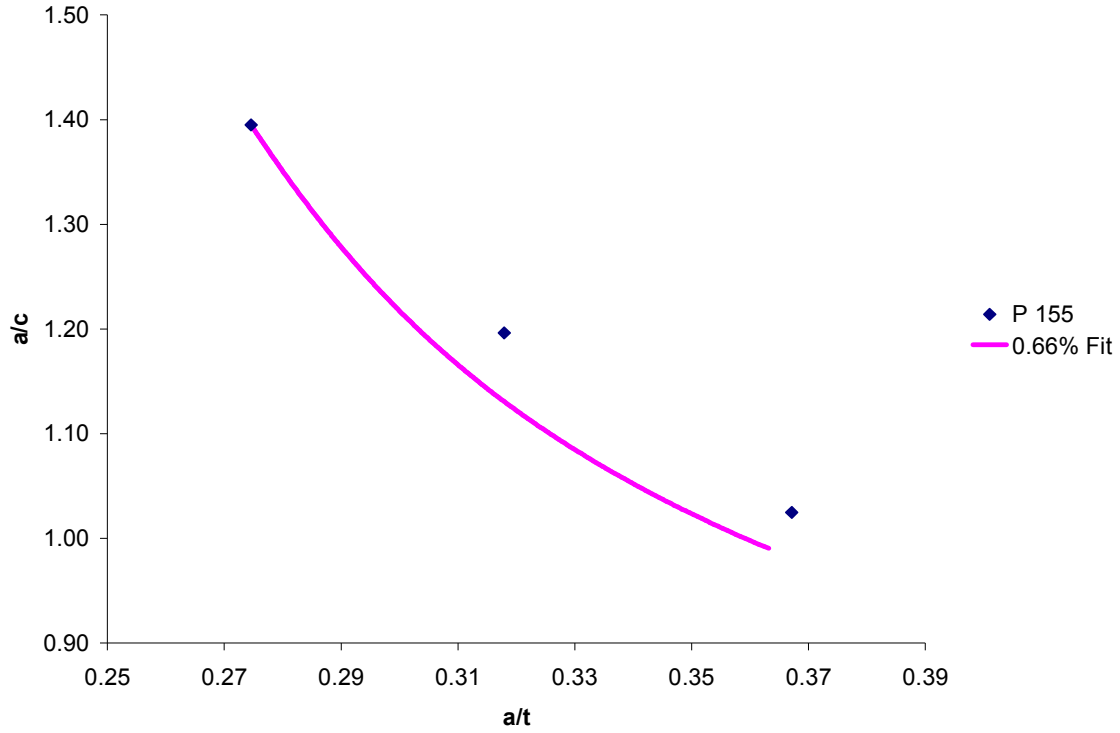

Figure 4.43. Comparison of the aspect ratio evolution versus crack depth between experimental results and the data fit prediction obtained from FEA results for P 155.

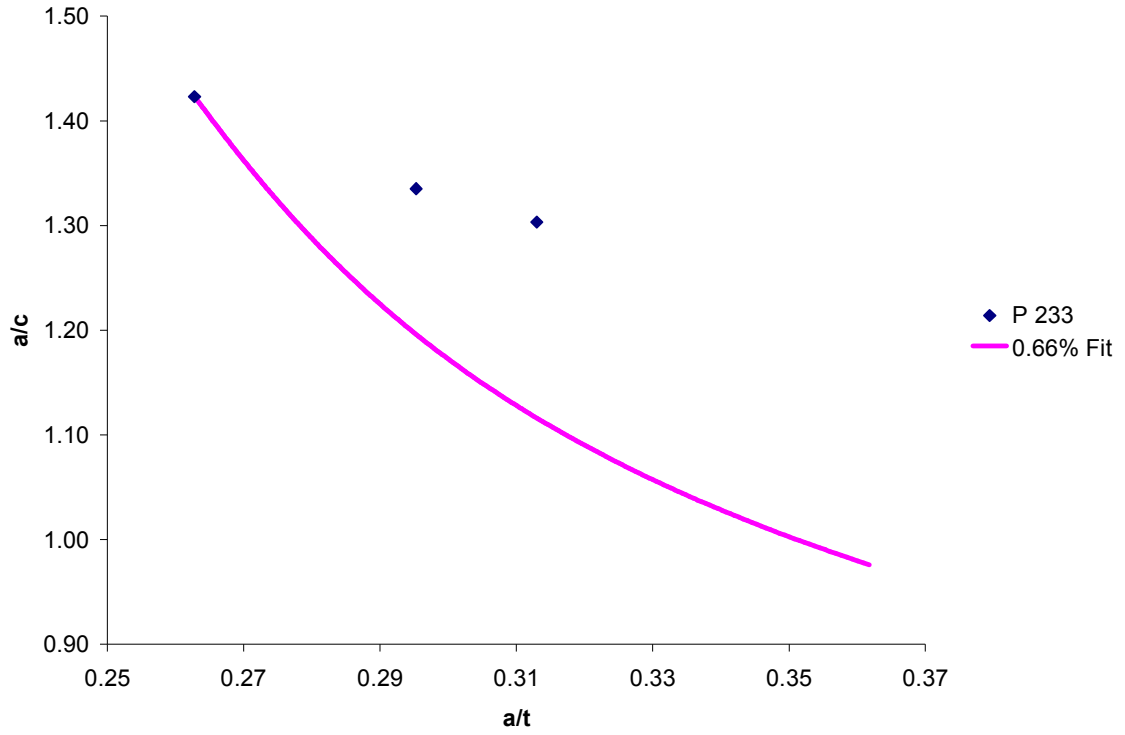

Figure 4.44. Comparison of the aspect ratio evolution versus crack depth between experimental results and the data fit prediction obtained from FEA results for P 233.

A couple different conclusions may be drawn from the varying success observed for the predictions based on the FEA models shown in Figures 4.43 and 4.44. First, the FEA based predictions are currently only useful as an approximation of the actual crack growth and shape evolution. The predictions are capable of simulating the general trend of crack shape change. The observations also show that the initiation mechanism may affect the subsequent long crack growth, which is reflected in the relative accuracy of the predictions for the specimens where a crack initiated on the surface compared to the predictions for subsurface crack initiation. Subsurface crack initiation obviously affects the initial surface crack aspect ratio, but it may also produce an initial crack shape which is less elliptical than a crack initiated on the surface and result in a slightly different crack

growth pattern. The effect of the stress and strain fields from other cracks in the gage section of the specimens should also be considered as a possible influence on the crack growth evolution.

There is a large amount of future work that can stem from this small analysis to estimate long fatigue crack growth in LCF specimens of Rene 88. It is believed that a solution can be extracted that relates the J-integral around the semi-elliptical crack to geometrical parameters including the relative crack depth, a/t, absolute crack length, a, crack aspect ratio, and the round bar diameter; because the solution incorporates plasticity, it should also include terms that relate to the stress-strain characteristics of the material and affect the J-integral value such as the Ramberg-Osgood constants. More finite element models are needed to supplement this study, which incorporate several diameters of round bar specimens and different material hardening stress-strain hardening properties. The current results at least establish that the long fatigue crack growth stage is a relatively small fraction of the total fatigue life and that crack initiation and short crack growth are dominant, life-controlling stages, especially at low strain ranges in the P condition. Even when the FEA results for long semi-elliptical crack growth are summed with the Newman and Raju based results for subsurface crack growth in the P condition specimens tested with $\Delta\varepsilon = 0.79\%$, the predicted low cycle fatigue life is much lower than the experimentally observed fatigue life.

4.4. Crack Initiation and Short Crack Growth Models

It is necessary to begin the analysis of crack initiation and short crack growth models with observations of crack initiation mechanisms from the previously described low cycle fatigue experiments. In the three specimens tested with $\Delta\varepsilon = 0.66\%$ in the P condition, two had dominant cracks that initiated in the specimen subsurface and one had a dominant crack that originated from slip band cracking (Figure 4.45). For the P condition specimens tested with $\Delta\varepsilon = 0.79\%$, all three had dominant cracks that initiated around subsurface oxide inclusions. At higher strain ranges in condition P, dominant cracks always initiated at the surface of the specimen; only one initiated at a surface inclusion, while the others initiated from slip band cracking. In summary, four out of the six P condition specimens tested at $\Delta\varepsilon = 0.66\%$ and $\Delta\varepsilon = 0.79\%$ had failures that initiated from a subsurface feature; Table 4.11 summarizes the P condition crack initiation sites. Statistical inferences cannot be drawn for just six experiments tested at low strain ranges, but these observations may imply that subsurface initiation is at least as likely if not more likely than surface initiation in P condition specimens tested at low strain ranges. Also of interest is the observation that subsurface initiation occurred in these specimens at various distances from the specimen surface and the inclusions were of multiple sizes, though each inclusion cluster was at least four times the grain size; this implies that inclusion location within the specimen may not be of great importance but rather the presence of an inclusion with a critical size may be more significant. Slip band crack initiation must be more difficult than crack initiation and subsequent crack growth from an oxide inclusion at these low strain ranges in condition P when a critically sized inclusion cluster is present; evidence of this is observed in the P condition specimens

tested at applied strain ranges of 0.79% and below and in observations by Caton *et al* [2]. However, at strain ranges that induce a larger amount of plastic strain within a slip band, crack initiation becomes easier and possibly more favorable in a slip band than crack initiation from an oxide inclusion; all the failures in the N, O, and P conditions except for one P specimen failed from a surface slip band crack at applied strain ranges larger than $\Delta\varepsilon = 0.79\%$.

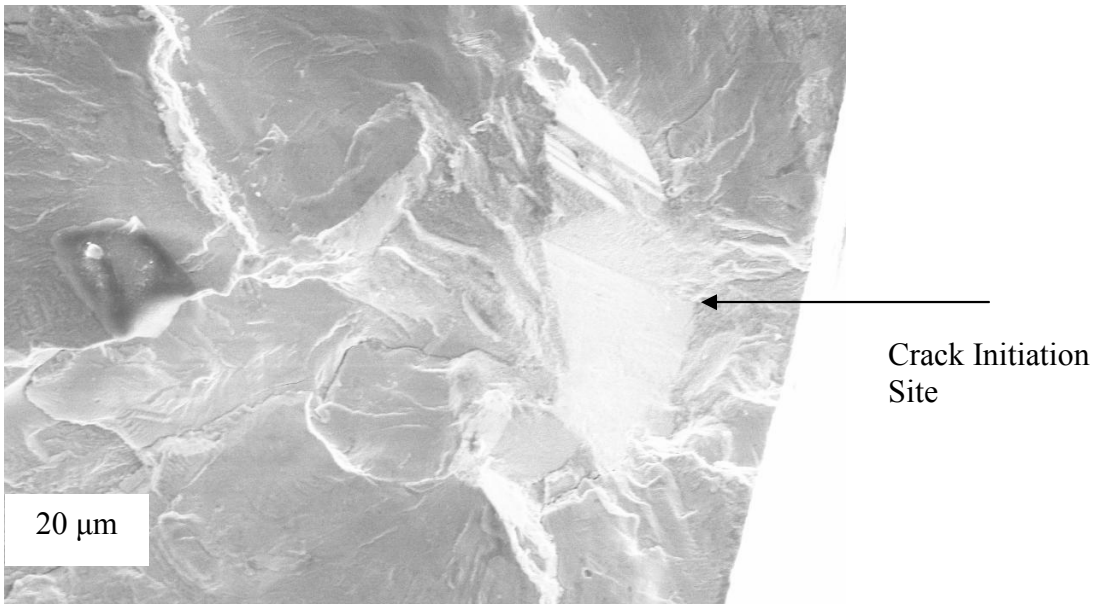

Figure 4.45. SEM image of the crack initiation region of a P condition specimen tested with $\Delta\varepsilon = 0.66\%$.

Table 4.11. Summary of P condition crack initiation sites.

Specimen	Initiation Site	Particle Major Dimension (μm)	Particle Minor Dimension (μm)	Distance from Surface (μm)	Cycles to Failure
211	Surface			on surface	8,040
111	Surface Particle	6.6	6.5	2.4	58,330
133	Inclusion Cluster	120	28	2260	139,150
122R	Inclusion Cluster	72	15	1270	182,200
222	Inclusion Cluster	45	25	790	197,570
233	Subsurface	16	5.6	400	491,180
144R	Subsurface	9.4	6.5	4290	928,420
155	Surface			on surface	977,060

There is obviously a competition between the two crack initiation mechanisms, which may also be partially related to the crack size formed from each mechanism. In the P condition specimens, a crack that initiates in a single grain is approximately 6 to 10 μm in size; a crack that initiates from an inclusion cluster is observed to have one major dimension that is at least 45 μm (Table 4.11). Thus, a crack that initiates from an inclusion cluster has a larger stress concentration around it than a crack initiated from a slip band. This suggests that the critical size of the inclusion cluster may be larger than the grain size of the material. Figure 4.46 shows two aluminum oxide particles in a planar metallographic section from the tested gage section of P specimen 222; it is typical of several particles that are found in the metallographic section that are approximately 1 μm or smaller. The figure shows that particle cracking or debonding may be present, but the crack did not extend into the surrounding microstructure in 197,000 cycles, which is approximately the number of cycles to failure for the specimen. Observations of several particles such as this in the planar metallographic section along with the observed sizes of inclusion clusters on fracture surfaces supports the argument that an inclusion that

initiates a dominant fatigue crack must be of a critical size larger than the grain size of the material; observations by Jablonski [25] and Alexendre *et al*. [36] and described in Chapter 2 complement this assertion. If inclusions of similar size to those observed on the P condition fracture surfaces are present in the N and O conditions, then cracks that initiate around them have a similar stress concentration to the cracks initiated in grains with 10-40 μm diameters. It is also likely that there are several more grains that initiate 10-40 μm cracks than inclusions because of the very low inclusion volume fraction.

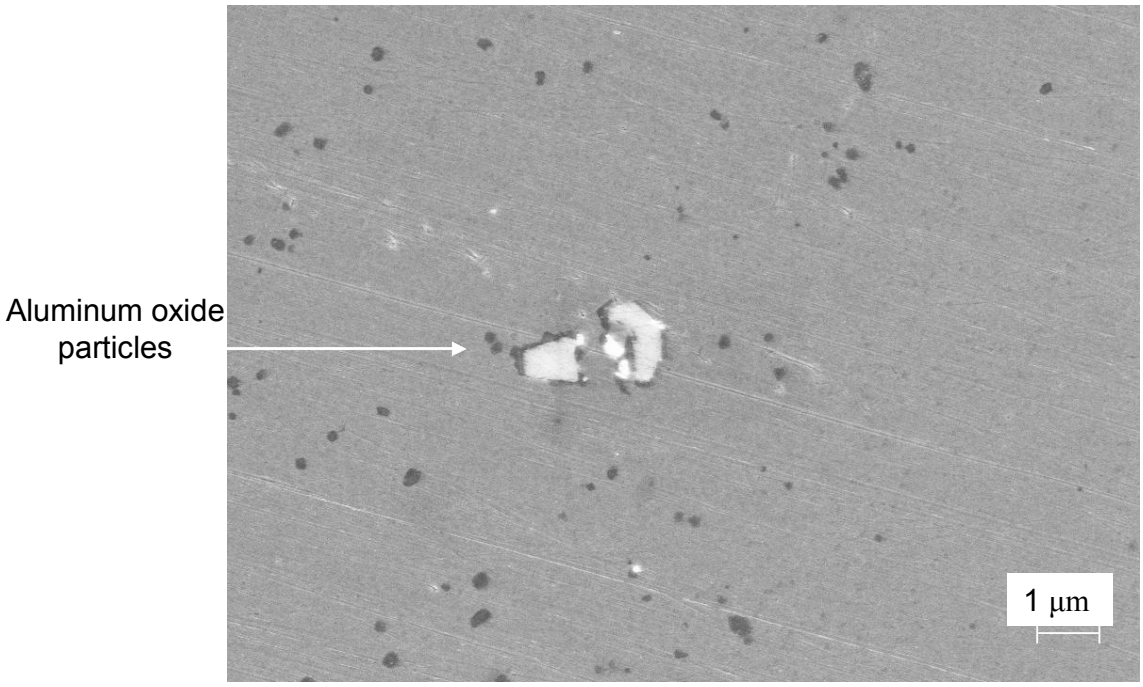

Figure 4.46. Aluminum oxide particles in a planar metallographic section from the gage section of P 222 after testing.

Another aspect that must be considered in this analysis of the competition of crack initiation mechanisms is the relative ease of crack initiation around a subsurface inclusion versus crack initiation from slip band cracking. Inclusions are natural sites for crack

initiation because they have a different coefficient of thermal expansion than the matrix and it is likely that material debonds around the inclusion under strain because there is very little coherency or bonding between the inclusion and the matrix; additionally, they are brittle and may crack with relatively small amounts of applied stress. Slip bands are probably more resistant to crack initiation because the slip band has to develop and damage must accumulate within the slip band in order for a crack to initiate. Figure 4.46 shows that though debonding may occur around even 1 μm inclusions, the crack did not grow into the surrounding microstructure; this is a typical observation of the small oxide inclusions observed in the P 222 metallographic section of the gage material. Once again, this suggests the inclusion cluster must be a large enough size so that a crack that initiates around the cluster provides a stress concentration sufficient to extend the crack into the surrounding material. Recall from the section describing the fracture toughness results that the crack repeatedly grows in an unstable manner and then arrests as the material around the crack tip hardens, increasing the resistance to crack growth. It is possible that even though a crack easily initiates by debonding around an inclusion, it is very difficult for the crack to extend into the surrounding microstructure due to the hardening of the surrounding material. In effect, this makes the competition between inclusion and slip band crack initiation more even with respect to the ease of crack initiation and reduces the possibility of dominant fatigue cracks arising from relatively small inclusions. All of the P condition specimens exhibited very long lives compared to the specimens from the N and O conditions, which implies that it was very difficult to initiate and grow dominant fatigue cracks in the P condition and there are relatively few locations within the material that can do so through inclusion or slip band crack initiation.

Models have been developed to assist in predicting the dominant crack initiation mechanism and subsequent fatigue life based on grain size and applied strain range. The three microstructural conditions, N, O, and P, have very similar primary γ' characteristics that include size distribution, nearest neighbor distance, and volume fraction. However, the average grain size for condition P (6 μm) is more than three times smaller than the average grain size for conditions N and O (20 μm). Also, the dominant crack always initiated at the surface of the low cycle fatigue specimens in the N and O conditions at the various applied strain ranges; however, the P condition exhibited both subsurface and surface initiation, where the subsurface initiation nearly always originated at an oxide inclusion. The cracks initiated on the surface had characteristics implying they originated from slip band cracking. Additional LCF specimens tested by the Caton *et al.* on Rene 88 with a similar grain size to conditions N and O and with strain ranges below 0.5% exhibited mostly subsurface failures, which were not associated with slip band cracking [2]. Thus, the model in this research, which includes grain size as the main microstructural input, was designed with the intent of predicting the likelihood of crack initiation due to slip band cracking and from that, deduce the probability of subsurface crack initiation from an inclusion; these results will also make relative predictions for the relative fatigue life for several applied strain ranges.

Since the likelihood of slip band cracking is dependent on the plastic strain and resulting accumulation of damage within a slip band, models predicting this mechanism should naturally include grain size. Venkatarman *et al.* [56] used an edge dislocation dipole

model to predict slip band spacing from strain energy density calculations. Then, a model predicting the number of cycles to nucleate a crack in one of the slip bands was formed using this result combined the assumption that the strain energy within the band must equal twice the free surface energy to form new crack faces [57]. The resulting expression for the number of cycles to initiate a crack, n_i^α, is

$$n_i^\alpha = 0.037\left(\frac{a}{h}\frac{\mu}{\Delta\tau - 2k}\frac{1}{e}\right)\left(\frac{\gamma_s}{d\mu}\right)^{0.5} \quad (4.13).$$

The number of cycles to initiate a crack is dependent on the plastic strain and damage accumulation within a slip band. Parameters are included in the model which account for the damage accumulation. The grain size, *d*, and slip band width, *h*, are incorporated as well as a term that describes the shear strain within a slip band, $\frac{\mu}{\Delta\tau - 2k}$, where μ is the shear modulus and $\Delta\tau$-$2k$ is the shear stress minus the frictional stress in the slip band. The parameter '*e*' is an effective slip irreversibility factor, which likely has a distribution of values and depends on the test environment, and γ_s is the free surface energy required to make new crack faces. The model uses quantities that are relevant to the crack initiation mechanisms and data available in this study such as grain size and applied strain range.

Though the model based on minimizing strain energy accumulation to predict crack initiation is powerful and incorporates grain size, a parameter has also been developed by Fatemi and Socie [58] and studied further by Bennett and McDowell [37] that predicts crack initiation based on the plastic strain within a slip band and the normal stress to the slip band acting to open up a crack. The parameter is attractive because it includes a

crack opening stress and incorporates the plastic strain damage in the slip band. The expression for the Fatemi-Socie parameter is

$$\frac{\Delta\gamma^{p}_{\max}}{2}\left(1+k^{*}\frac{\sigma_{n}^{\max}}{\sigma_{ys}^{c}}\right) \tag{4.14}$$

where $\Delta\gamma^{p}_{\max}$ is the maximum plastic shear strain amplitude, $\sigma_{n}^{\max}$ is the peak tensile stress normal to the slip band, σ_{ys}^{c} is the cyclic yield strength, and k^* is a fitting parameter that has a value of approximately 0.5.

In deriving their expression for slip band spacing Venkataraman *et al.* determined that the average plastic shear strain amplitude in a slip band in a single grain, γ_p, can be calculated as

$$\gamma_{p} = 1.39(1-\upsilon)\left(\frac{\Delta\tau-2k}{\mu}\right)\frac{a}{w} \tag{4.15}$$

where the parameters have the same definitions as described previously, '*w*' is slip band spacing, and *v* is Poisson's ratio. This expression can be used as the plastic shear strain amplitude for a slip band in the Fatemi-Socie parameter.

The resulting model has several appealing features. If grains are considered individually, the model naturally has a dependence on grain orientation; grains oriented favorably for slip have relatively large values of $\Delta\tau$ and thus, larger values of the parameter. However, the parameter not only relies on the damage accumulation within the slip band but also the normal stress acting to open up a slip band crack. There is a linear relationship between the Fatemi-Socie parameter and the grain size of the material. The major

microstructural difference between microstructure conditions N, O, and P is the grain size, and very different crack initiation mechanisms and fatigue lives have been observed in low cycle fatigue for the three conditions. The grain size for conditions N and O is more than three times larger than the grain size for condition P, meaning the average Fatemi-Socie parameter will have a larger value for conditions N and O than condition P. Conditions N, O, and P have different mean tensile loads during the experiment due to different R ratios; this is accounted for in the modified Fatemi-Socie model in the term describing the maximum normal stress to the slip band of interest. Because the P condition specimens were tested with R=0, the mean tensile stress over all the applied strain ranges is higher than the N and O condition specimens tested with R=-1, which is reflected in a higher maximum stress during testing and leads to a larger maximum normal stress applied to a slip band, $\sigma_n^{\max}$.

The Fatemi-Socie parameter was used to investigate the probability of slip band cracking in the microstructure conditions N, O, and P on an individual grain by grain basis at an intermediate temperature of 650ºC. As a first approximation, a lognormal distribution around the average grain size for each microstructure condition was assumed, with the distribution tails equal to approximately twice and half the average grain size respectively; this is consistent with two-dimensional optical micrographs. Both γ and γ' are face centered cubic phases, and the dominant slip system at intermediate temperatures is in the {111}<110> family. The microstructure conditions have a lack of texture, so a random distribution of grain orientations was also assumed. Thus, if a force or displacement is applied uniaxially, then the dominant slip system in each grain is also

randomly oriented with respect to the loading axis. This scenario was simulated to calculate the distribution of Fatemi-Socie parameter values in individual grains for various applied strain ranges and for the three material conditions. Low cycle fatigue results indicate the materials have similar stress-strain characteristics, so the only variable that differed between the three conditions was the grain size distribution. The frictional resistance, k, was estimated to be 1/8 of the shear stress in the slip band based on approximations of the internal and frictional components of the shear stress [59].

An approximation of the slip band spacing was made based on work by Bailon and Antolovich [60]. Slip band spacing, i, was measured at various applied strain ranges in Waspaloy with an average grain size of approximately 125 μm, and a trend was determined for the relationship between slip band spacing and plastic strain range; the approximate resulting trend is

$$i = -3.23 \ln \Delta\varepsilon - 11.14 \qquad (4.16).$$

This trend was used to predict slip band spacing at various strain ranges in order to calculate the amplitude of the average plastic shear strain in a slip band within a single grain. The grain sizes in this research are much smaller than the grain sizes studied by Bailon and Antolovich; thus, the slip band spacing should be smaller in the Waspaloy than the Rene 88 for any plastic strain range. However, their results are merely used as an order of magnitude approximation for the variation of slip band spacing with applied strain. Since the slip band spacing is inversely proportional to the Fatemi-Socie parameter value, this approximation results in conservative estimates of the Fatemi-Socie

parameter. Combining equations 4.14, 4.15, and 4.16, an expression for the Fatemi-Socie parameter for these Rene 88 microstructures can be stated as

$$\frac{0.52(1-\nu)}{-3.23\ln\Delta\varepsilon - 11.14}\left(\frac{\Delta\sigma}{M\mu}\right)\left(1+\frac{\sigma_n^{\max}}{2\sigma_{ys}^c}\right)d \tag{4.17}$$

Figure 4.47 shows an approximate distribution based on histogram data of the Fatemi-Socie parameter for the N and O condition versus the P condition, where the applied strain range is approximately $\Delta\varepsilon = 0.66\%$. The distribution for the N and O conditions has a larger spread and a higher average value than the distribution for the P condition. A critical value of the Fatemi-Socie parameter, where a dominant crack initiates from a slip band when deleterious inclusions are present in the same material, may be defined. Based on the observations of initiation mechanisms described previously in this section at low strain ranges and the observation of relatively long low cycle fatigue lives in the P condition, assume this critical value lies towards the tail of the P distribution for $\Delta\varepsilon = 0.66\%$; as an example, a Fatemi-Socie value of 0.015 will be used. Approximately 7% of the grains in the P condition have a Fatemi-Socie value that is 0.015 or greater. In the N and O conditions for $\Delta\varepsilon = 0.66\%$, approximately 80% of the grains have a Fatemi-Socie value that is 0.015 or greater. The true critical value of the Fatemi-Socie parameter is not known, and the values of the parameter that control the dominant crack initiation are probably closer to the tail of the distribution with the larger values; however, this exercise demonstrates that if there are a small number of grains that can initiate a dominant crack in the P condition, then the number of grains with a similar value in conditions N and O is far greater. In this example, the Fatemi-Socie value 0.015 is even

below the average for this strain range in conditions N and O, which is approximately 0.022. Figure 4.48 shows a plot of the average Fatemi-Socie parameter for several applied strain ranges for the N, O, and P conditions. Because the tests were strain-controlled, the maximum stress in the P condition specimens decreased as the applied strain range increased, and the disparity between the average value of the Fatemi-Socie parameter in the N and O conditions versus the P condition increases as the applied strain range increases. The average value of the Fatemi-Socie parameter increases approximately as a power law function of strain range, which supports the observation that surface slip band cracking is dominant at the larger applied strain ranges.

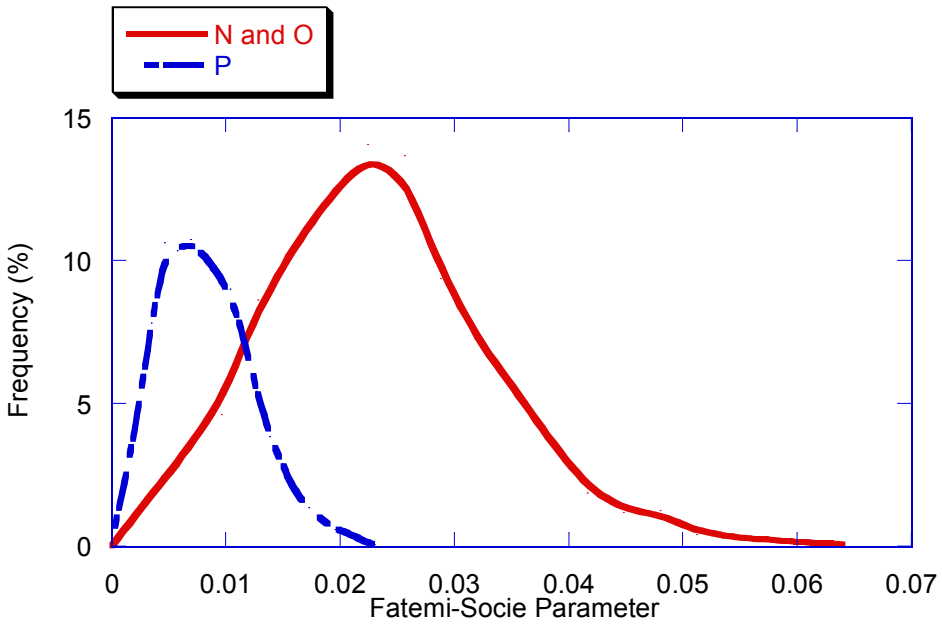

Figure 4.47. Approximate distribution of the Fatemi-Socie parameter for the N and O versus the P conditions with $\Delta\varepsilon = 0.66\%$.

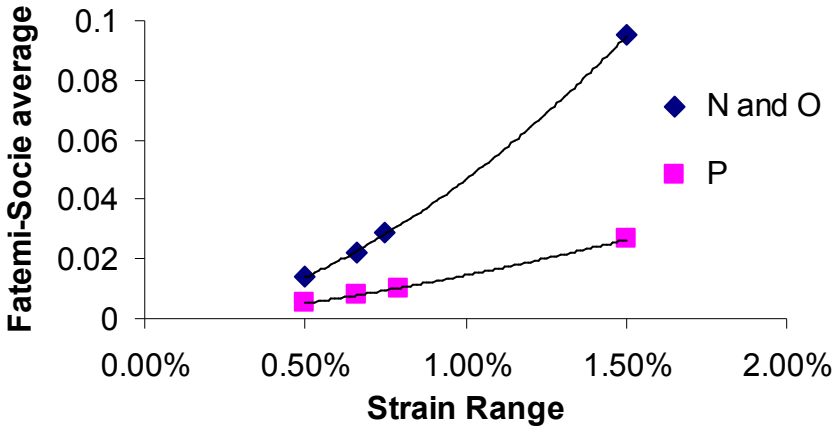

Figure 4.48. Average of the Fatemi-Socie parameter for several strain ranges.

There may be multiple interpretations for the physical significance of a critical value of the Fatemi-Socie parameter where slip band cracking is clearly the dominant crack initiation mechanism. This could simply mean that the damage accumulation within a slip band is sufficient to nucleate a large edge crack faster than a crack can nucleate from a subsurface oxide inclusion. In order for the crack to become the dominant crack, the surrounding grains must be oriented favorably for the crack to grow into the surrounding region; i.e. the surrounding grains must not place too much constraint on a possible crack initiating grain and they must also have large values of the Fatemi-Socie parameter due to the stress concentration from a crack in the initiation grain, which will be described in more detail shortly. If the distribution of the Fatemi-Socie parameter is spread over large values of the parameter, it is also more likely that cracks nucleate in grains in the same vicinity and then link together to form a larger crack; this could aid both in crack initiation and short crack growth and is a much greater possibility in the N and O conditions where a larger number of grains have a substantial Fatemi-Socie parameter value.

When a surface crack originates, there is naturally stress intensity in the vicinity of the crack tip. The stress intensity can promote crack propagation by increasing the damage accumulation and likelihood of crack formation in slip bands in the surrounding grains, which can link with the original initiated crack. Because the initial crack sizes in this analysis are extremely small, the linear elastic Newman and Raju solutions for a surface semi-elliptical crack in a rectangular bar [3] can be used to estimate stress intensity; this is a conservative estimate because the Newman and Raju solution is purely based on mode I loading and the crack is probably oriented approximately 30-45º from the loading axis as described previously. Then, the stress ahead of the crack tip can be estimated using Westergaard's solutions for linear elastic stress fields around a crack tip [61]. The solution begins to lose accuracy when the distance ahead of the crack tip, r, is approximately 0.15 of the crack length, a [52]. This stress is used as a conservative estimation of the stress in the entire grain ahead of the crack tip. When a crack initiates in the N, O, or P condition in one of the grains with a size towards the tail of the larger values of the grain size distribution, the stress at distance of $0.15*a$ ahead of the crack tip is approximately 10% greater than the remote applied stress; thus, the Fatemi-Socie parameter distribution also shifts in the positive direction by 10% and the probability of the initiated crack encountering grains with large values of the parameter increases. If two large grains initiate a crack on the surface due to a low angle of misorientation between them, the stress ahead of the crack tip is approximately 20% greater than the remote applied stress, and the crack would likely be able to propagate more easily into

the surrounding microstructure during the short fatigue crack growth stage and result in a shorter fatigue life than if the crack had initiated in a single grain.

This simple analysis of the Fatemi-Socie parameter probability distribution exhibits how it may be used to explain the difference in observed crack initiation mechanisms and fatigue lives between microstructure conditions N and O versus P. Because of their larger grain sizes, microstructure conditions N and O are much more likely to initiate slip band cracks and propagate them through the short fatigue crack growth stage. This could account for the considerable differences in fatigue life between conditions N and O versus condition P with the much smaller grain size. It can also shed light on the occurrence of the transition strain range defined by Hyzak and Bernstein [26], where subsurface crack initiation is more likely to occur below the transition strain range and surface crack initiation is more likely to occur above it. At the largest applied strain ranges, $\Delta\varepsilon$=1.15% and $\Delta\varepsilon$=1.5%, there were multiple surface crack initiation sites, which indicates the ease and higher probability of multiple grains being favorable for slip band cracking at higher strain ranges. As the remote applied strain increases, the distribution of Fatemi-Socie values within the grains also increases, and slip band crack initiation and growth from the specimen surface becomes easier and more probable than crack initiation from a subsurface feature. The model does not consider the constraint imposed by surrounding grains, which would affect the shear strain and damage accumulation within the grain of interest. Further studies are necessary to determine the extent to which crack initiation is suppressed because of misorientation with respect to surrounding grains. EBSD analysis could provide orientation data on the grains in the vicinity of the crack

initiation region and validate this modified Fatemi-Socie model, which links the probability of crack initiation to specific grain orientations and sizes.

4.5. Results and Discussion Summary

The experiments and analysis conducted in this research provided results that shed light on microstructural influence on the fatigue life of Rene 88DT at intermediate temperatures. Analysis of microstructure conditions N, O, and P indicates the primary γ' volume fraction and size distribution is very similar as well as the carbide content; however, the grain size for the P condition is more than three times smaller than the grain size in the N and O conditions. Tensile, fracture toughness, and fatigue crack growth properties were obtained for conditions N and O, and all the properties were the same for the two conditions. Low cycle fatigue properties were compared between conditions N, O, and P and it was found that the fatigue stress-strain characteristics were the same between the alloys but the fatigue life in the P condition specimens was much greater. Additionally, two mechanisms of fatigue crack initiation were observed: initiation from subsurface inclusions and initiation from surface slip band cracking. Newman and Raju linear elastic stress intensity solutions for elliptical cracks in round bars were employed to estimate fatigue life for subsurface cracking. These results and an ABAQUS analysis of semi-elliptical surface cracks revealed that the long fatigue crack growth stage is a small fraction of the total fatigue life at low applied strain ranges, especially for the P condition. The Fatemi-Socie parameter for crack initiation was utilized to explain the differences in fatigue life between conditions N and O versus P.

CHAPTER 5

CONCLUSIONS AND RECOMMENDATIONS

Low cycle fatigue and fatigue crack growth experiments at an elevated temperature were performed on Rene 88DT with the objective of relating these properties to the life-controlling microstructural features. The results of these experiments have been used to develop models for crack initiation, short crack growth, and long crack growth, and to garner a more in depth understanding of the operative mechanisms during these three stages of fatigue life. The results and analyses have produced the following observations and conclusions:

1. The two-step heat treatments to produce the N and O conditions of the microstructure, where only the first step cooling rate was varied, did not produce the expected γ' size distributions. The grain size and primary γ' volume fraction and size distribution were compared for conditions N, O, and P. The primary γ' volume fractions and size distributions were very similar for the three microstructure conditions, but the precipitate morphology was generally dendritic in the N and O conditions and cuboidal in the P condition. A significant difference was measured in the grain size for the three conditions; conditions N and O had an average grain diameter of 20-21 μm, while condition P had an average grain diameter of 6 μm.

2. The microstructural differences between conditions N, O, and P did not produce significant differences in the elevated temperature cyclic stress-strain properties

of the tested Rene 88 material. Most likely, these properties are more strongly related to the overall γ' volume fraction that did not vary sufficiently with the heat treatments used in the study.

3. There are competing mechanisms that govern the crack initiation in Rene 88 low cycle fatigue specimens at 650ºC. Slip band cracks appeared to form on the specimen surface at all of the experimental strain ranges and critically-sized inclusion clusters appeared to initiate cracks at the low strain ranges. Subsurface crack initiation was only observed in the P condition specimens, which indicates grain size has a large influence on which mechanism dominates; this conclusion is based on the difference in grain sized observed in conditions N and O versus P.

4. Fatigue life estimates from the long crack growth models implemented via finite element analysis account for at most half of the experimentally observed fatigue lives of low cycle fatigue specimens in the N and O condition and a very small fraction of the fatigue lives observed in the P condition at low applied strain ranges. These results underscore the importance of understanding and modeling crack initiation and short crack growth lifetimes because they seem to be the dominant and life-controlling stages in low cycle fatigue conditions.

5. Subsurface crack growth shape evolution can be accurately estimated by Newman and Raju's solution for an elliptical crack in a round bar [3]. However, it was observed that even if the predicted number of cycles required to form a long semi-

elliptical surface crack from the subsurface crack are added to the estimated number of cycles required for a surface crack to reach a critical size based on the FEA analysis, the total number of fatigue cycles are still considerably lower than the observed LCF lives.

6. Microstructure conditions N and O exhibited much lower low cycle fatigue lives than condition P for tests of similar strain ranges. The only major microstructural difference between these conditions is the grain size; condition P has a grain size of 6 μm while conditions N and O have a grain size of 20 μm. The Fatemi-Socie parameter modified by a grain size dependent term that predicts the plastic strain within a slip band may be used to quantitatively describe the ease and probability of slip band cracking in each condition. Based on this analysis, crack initiation is much more probable in the larger grain size N and O conditions. This explains why there is a disparity in the fatigue lives between the different conditions and why subsurface initiation is observed in condition P and not in conditions N and O. It also reinforces the notion of a transition strain range below which subsurface cracking is more probable and above which surface cracking is more likely. Of course, this transition strain range will also be affected by the size of defects in the material and their proximity to the specimen surface.

7. The ability of Rene 88DT to arrest crack growth was exhibited in fracture toughness experiments performed on conditions N and O at 650ºC. A nonlinear relationship and continuous unloading-loading was observed throughout the load versus load-line displacement diagrams, which arose from unstable crack growth “pop-ins” during the experiments. Tensile tests performed on Rene 88 material demonstrate a large

degree of plastic hardening. The ability of the material to plastically harden can act to arrest a mode I crack as stress and strain fields develop around the crack tip and result in unstable increments of crack extension as the crack repeatedly grows and arrests. This ability makes it difficult to predict a critical stress intensity value for Rene 88DT.

The conclusions have opened the possibility for several avenues of investigation regarding the microstructural influence on mechanical properties and the best methods to describe and predict the mechanisms governing fatigue. Thus, the following recommendations for future exploration are presented:

1. Heat treatments can be performed to produce appreciably different conditions of the the γ' size distribution and volume fraction within the microstructure to better determine the strengthening precipitate's influence on low cycle fatigue stress-strain properties and lives. It was concluded that the material's hardening characteristics play a large role in the rate of crack growth, so a relationship between the γ' size distribution and volume fraction, the hardening properties, and the crack growth rate would be valuable. The hardening properties of the alloy may also influence the crack initiation mechanism because slip band cracking is dependent on the amount of damage accumulation within a slip band, so the effect of the γ' size distribution and volume fraction on the competition between crack initiation mechanisms in low cycle fatigue conditions should be investigated.

2. Experiments should be performed with the objective of determining the characteristics of the grains where crack initiation occurs. For example, a focused ion beam could be used to mill a small amount of material from the cross section of the fracture surface crack initiation region producing a very smooth surface. Then, an electron backscatter diffraction analysis could be conducted to determine the grain sizes and orientations that contributed to crack initiation. Alternatively, bending fatigue tests could be performed using rectangular bars instead of uniaxial experiments with round bar specimens. EBSD could then be conducted on the surface of these specimens in the crack initiation region without having to remove material from an uneven geometry such as the round bar specimens to make the necessary flat area to perform EBSD analysis. These experiments would be valuable in complementing existing crack initiation models involving slip band cracking.

3. The Fatemi-Socie parameter and other slip band crack initiation parameters should be developed to account for the constraint imposed by the surrounding grains. This may be a probability-based analysis using the orientation of the surrounding grains with respect to the orientation of the grain in which the crack initiates. Furthermore, the applicability of the Fatemi-Socie parameter to short crack growth should be studied using the probability of finding certain grain orientations around the crack tip to determine the likely short crack growth path.

4. The finite element crack growth predictions in this work are specific to a material, specimen and crack geometry, and applied stress or strain. Further finite

element analysis should be conducted using different specimen and crack geometries to develop complete crack growth models for semi-elliptical cracks in round bars that are dependent on parameters such as crack size, aspect ratio, location along the crack front, material hardening properties, and applied stress or strain. The parameters would ensure the models are valid for a variety of materials with different plastic hardening characteristics.

APPENDIX A

LOW CYCLE FATIGUE Δσ VERSUS Δε CURVES

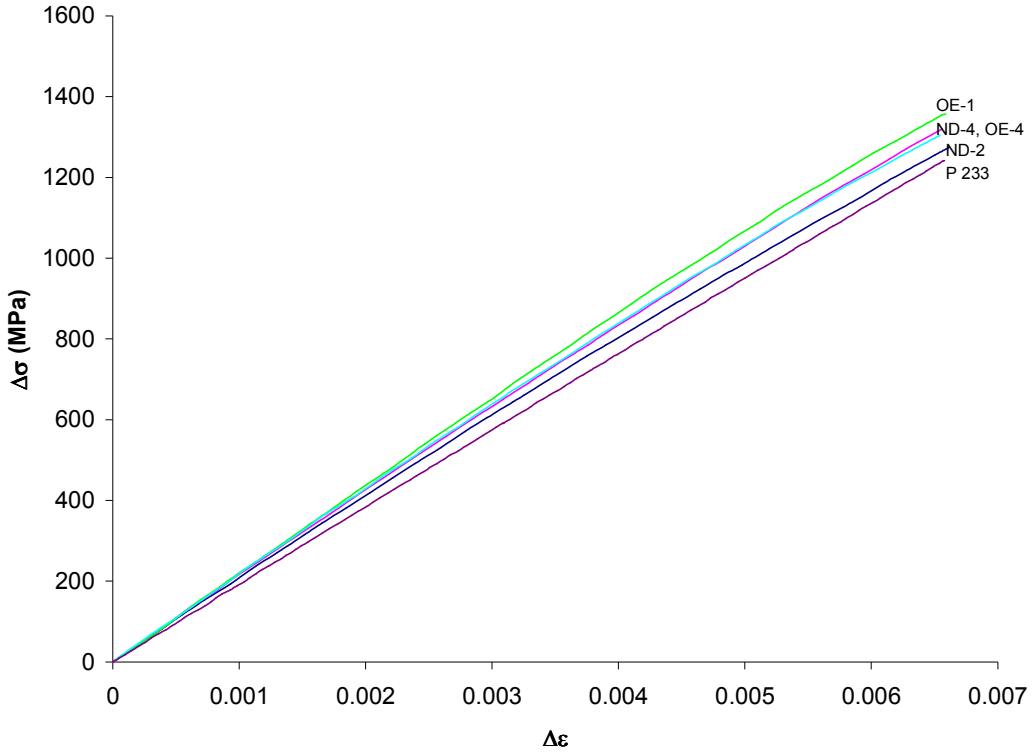

Figure A.1. Plot of Δσ versus Δε for the three microstructure conditions tested with Δε = 0.66%.

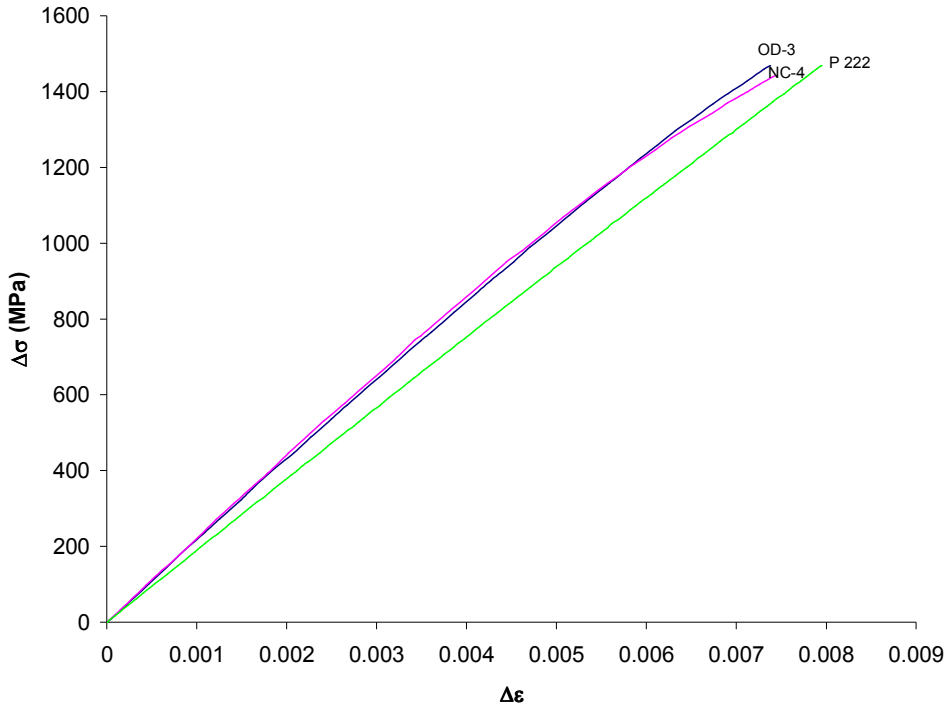

Figure A.2. Plot of Δσ versus Δε for the three microstructure conditions tested with Δε = 0.75% to Δε = 0.79%.

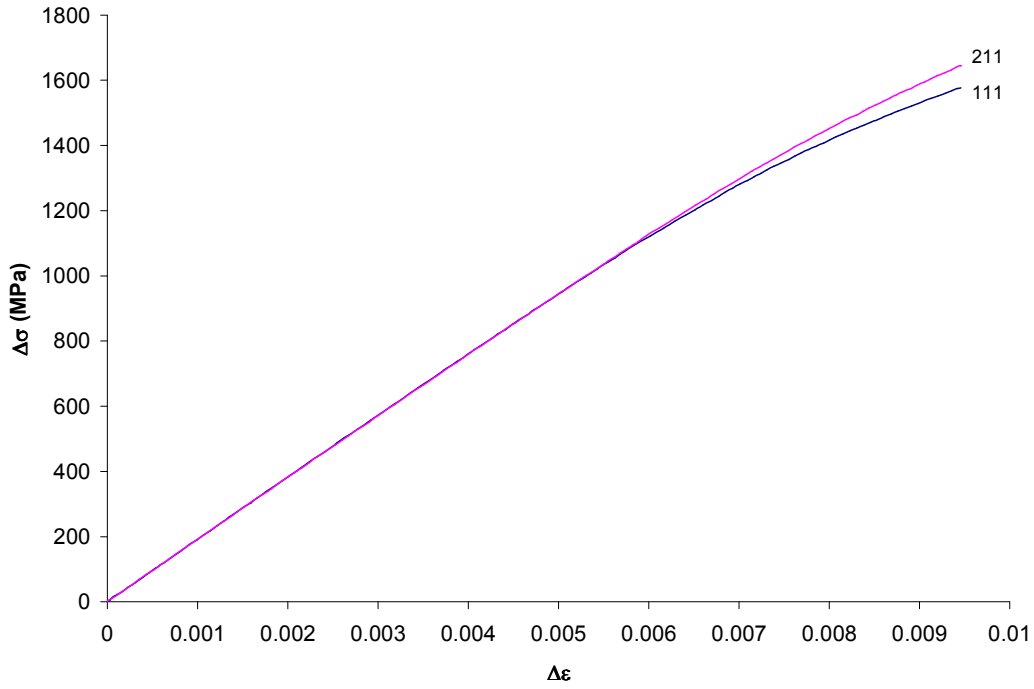

Figure A.3. Plot of Δσ versus Δε for the P condition tested with Δε = 0.94%.

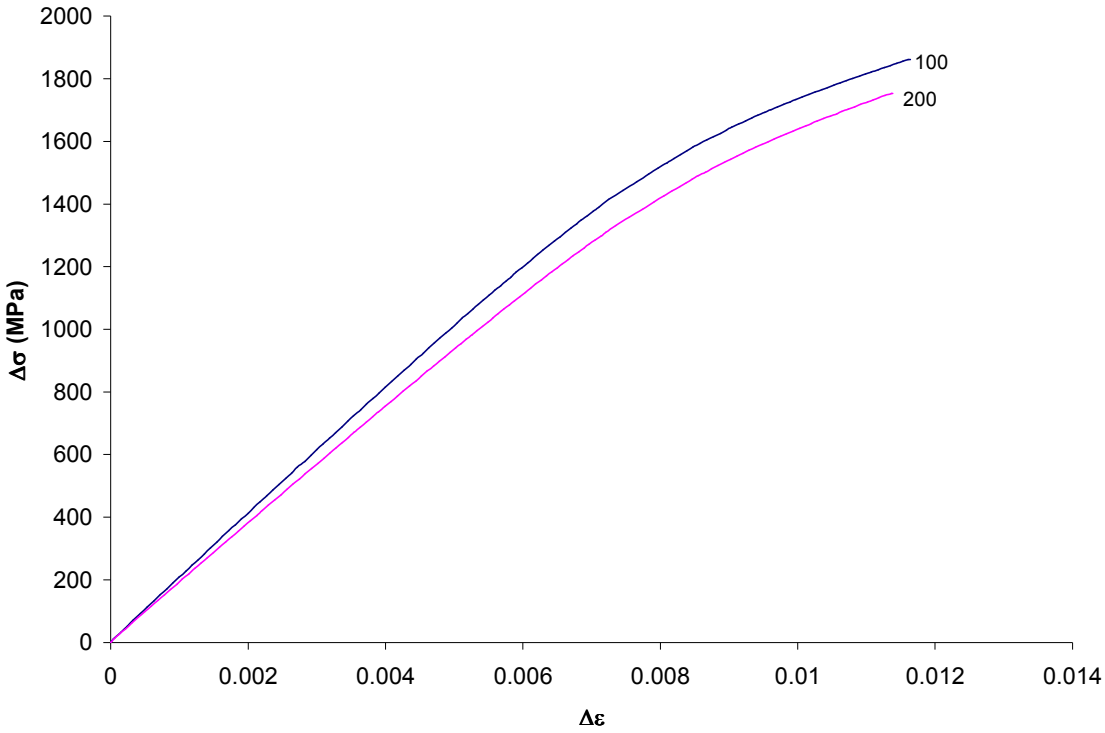

Figure A.4. Plot of Δσ versus Δε for the P condition tested with Δε = 1.15%.

APPENDIX B

TEMPERATURE VERSUS TIME HEAT TREATMENT DIAGRAMS FOR MICROSTRUCTURE CONDITIONS N AND O

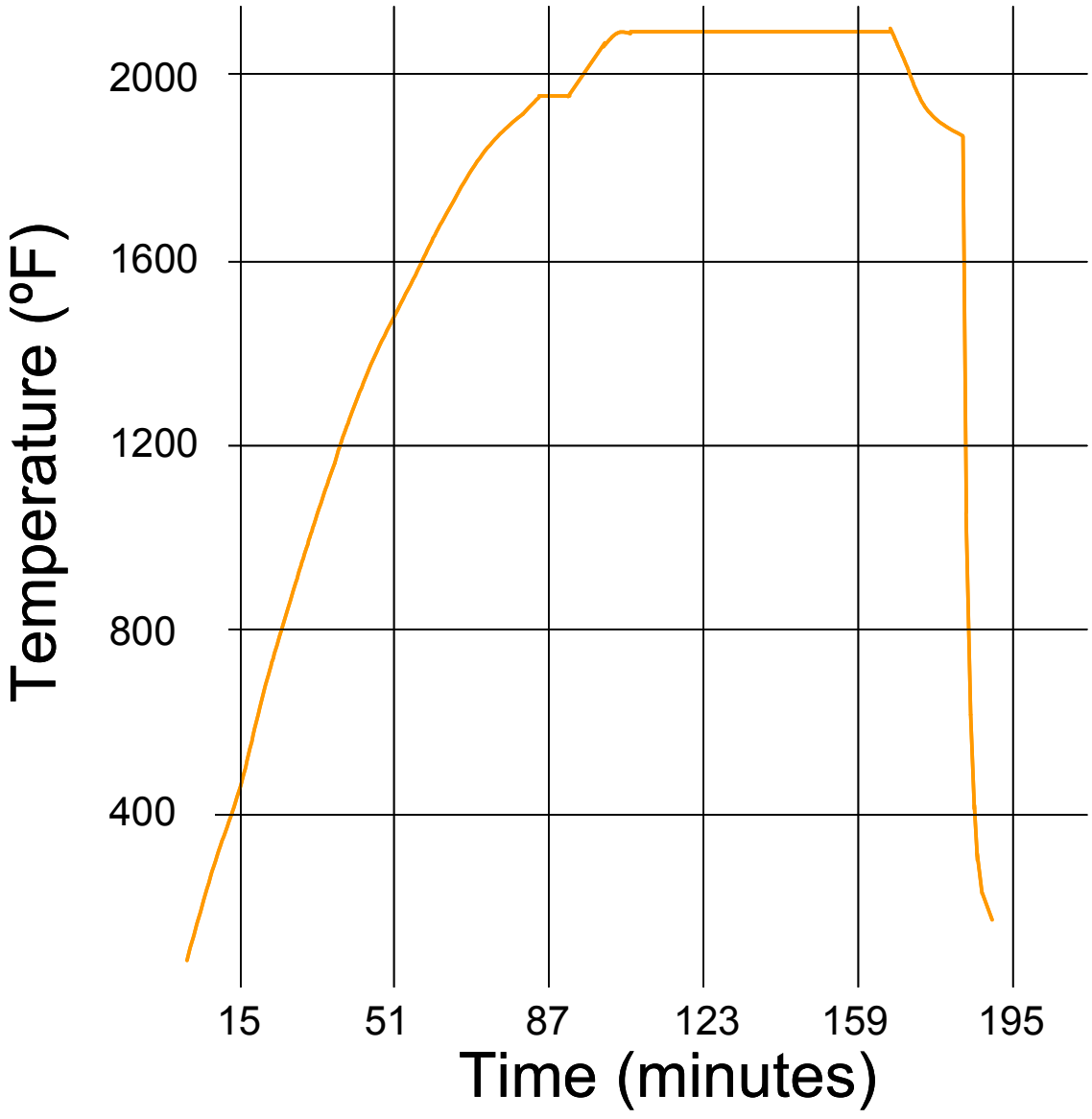

Figure B.1. Temperature versus time for the heat treatment that was used to produce microstructure condition N.

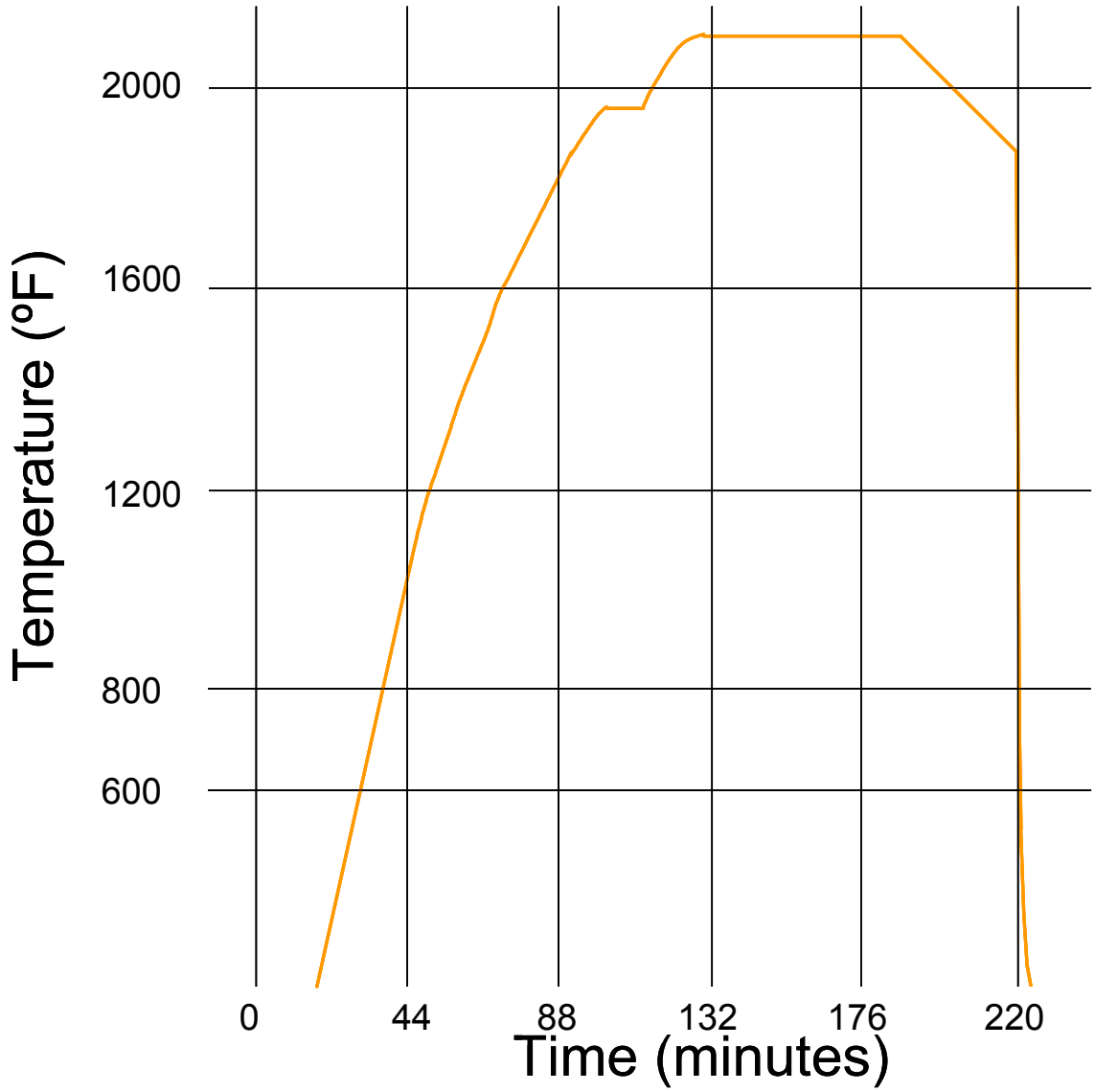

Figure B.2. Temperature versus time for the heat treatment that was used to produce microstructure condition O.

APPENDIX C

LOW CYCLE FATIGUE FRACTURE SURFACE IMAGES

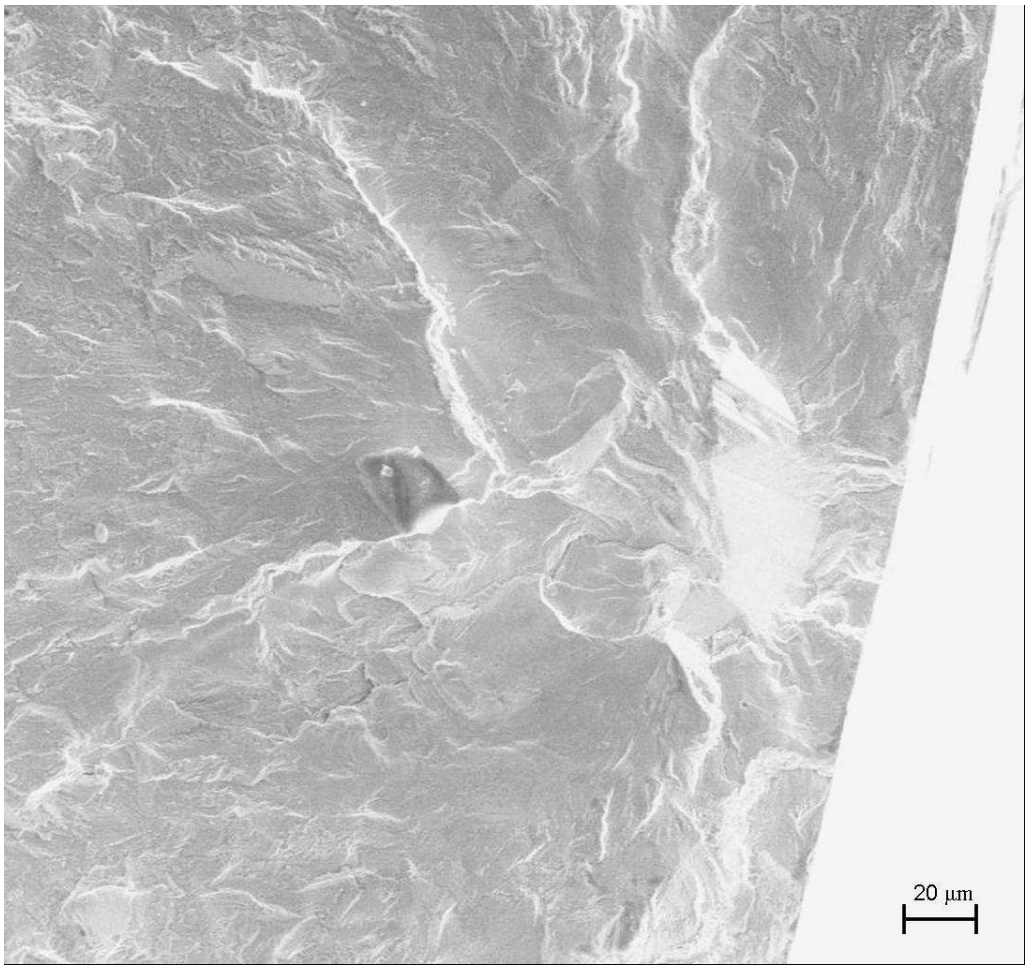

Figure C.1. Crack initiation region in specimen P 155 tested at $\Delta\varepsilon = 0.66\%$.

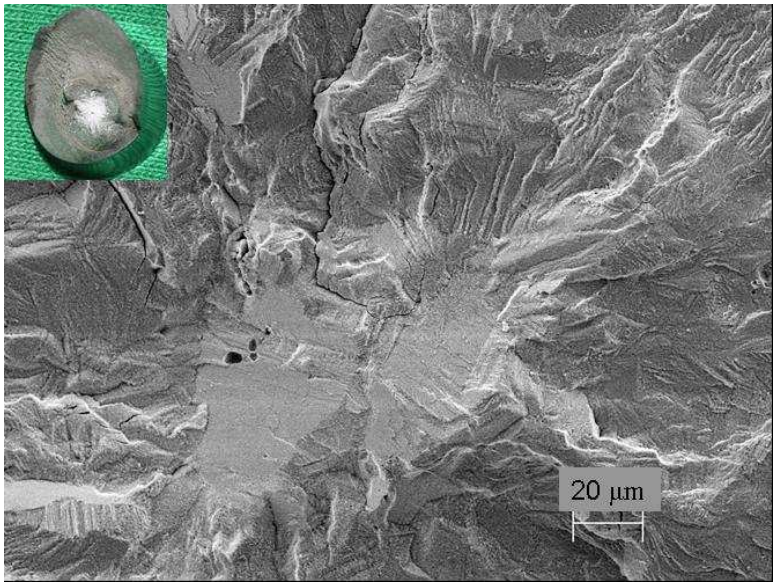

Figure C.2. Subsurface crack initiation region in specimen P 144R tested at $\Delta\varepsilon = 0.75\%$. The inset shows a lower magnification stereoscope image of the specimen.

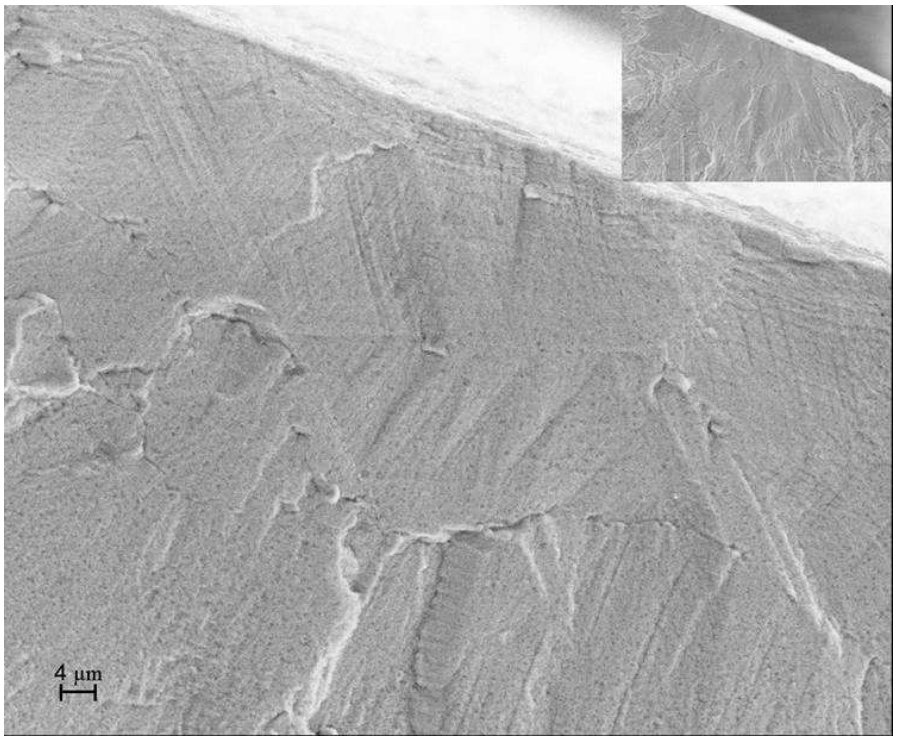

Figure C.3. Crack initiation region in an N condition specimen tested at $\Delta\varepsilon = 0.75\%$. The inset shows a lower magnification SEM image of the initiation site.

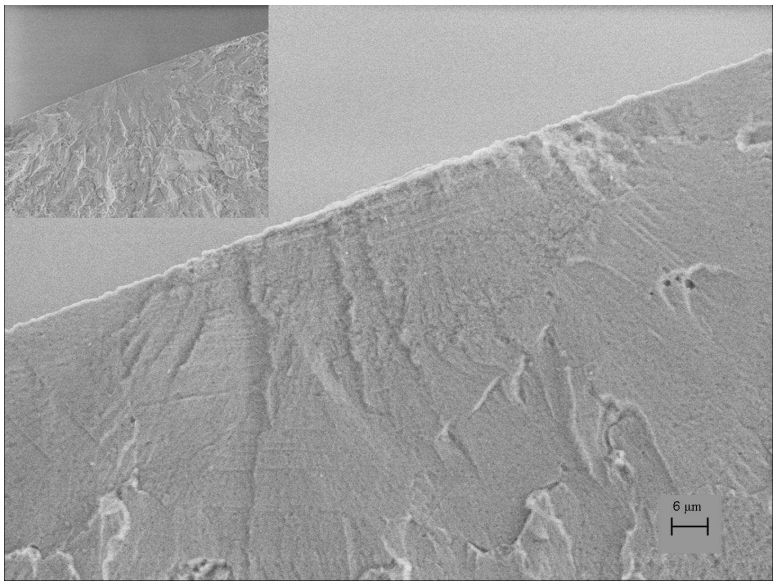

Figure C.4. Crack initiation region in an O condition specimen tested at $\Delta\varepsilon = 0.75\%$. The inset shows a lower magnification SEM image of the initiation site.

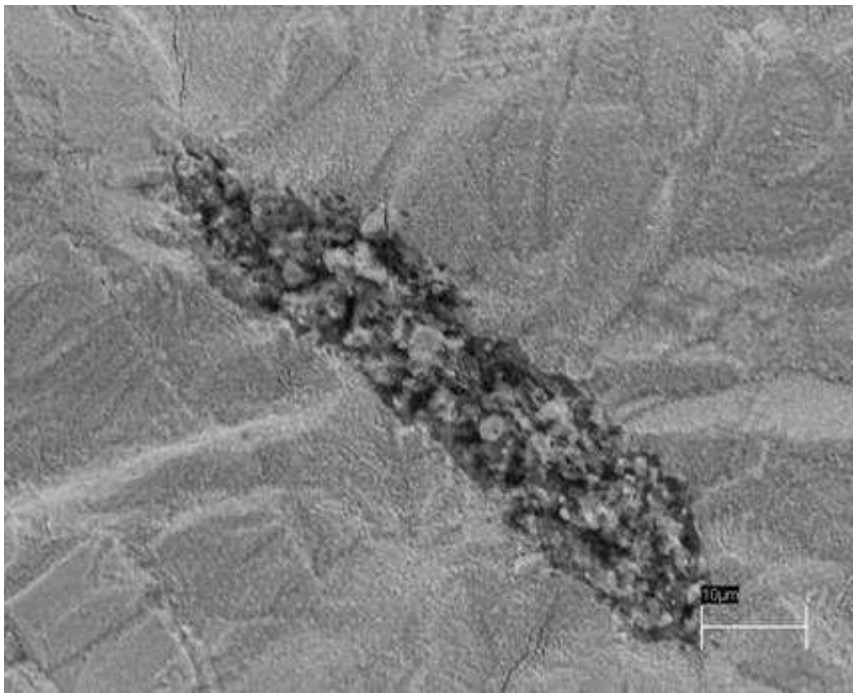

Figure C.5. Subsurface particle cluster in specimen P 122R tested at $\Delta\varepsilon = 0.79\%$.

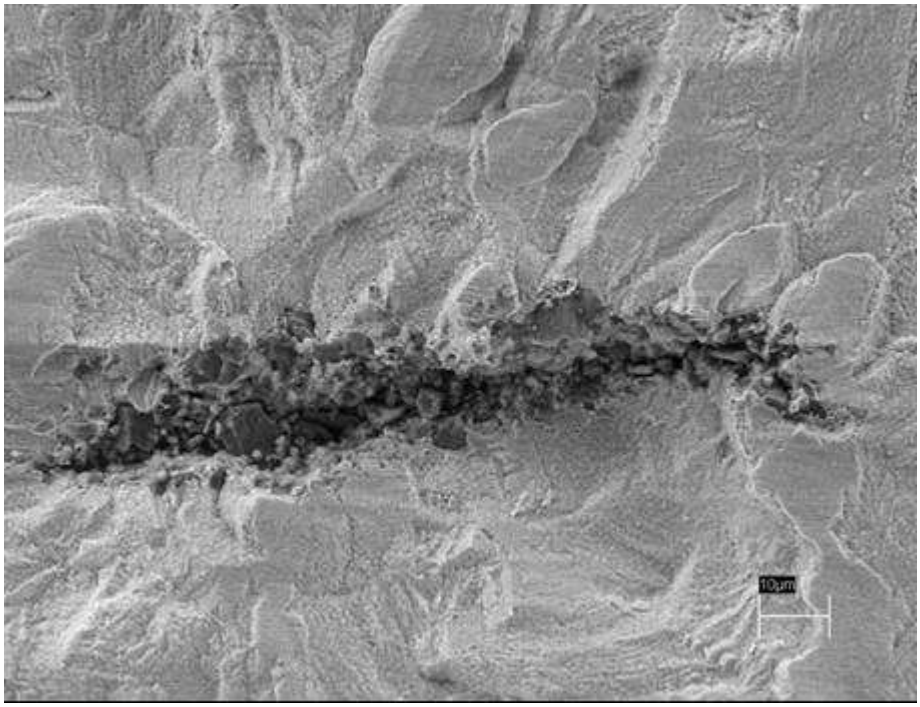

Figure C.6. Subsurface particle cluster in specimen P 133 tested at $\Delta\varepsilon = 0.79\%$.

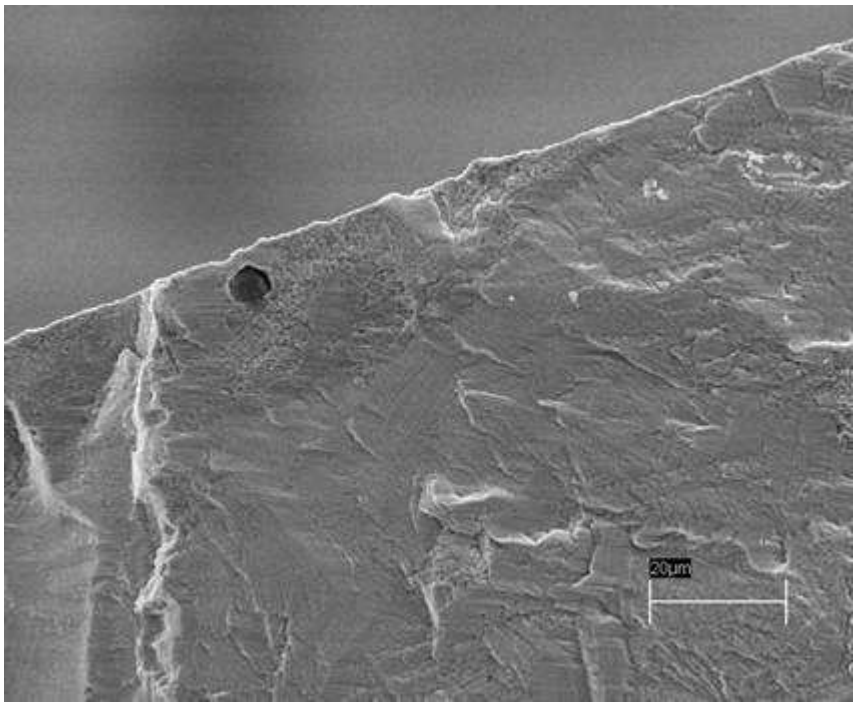

Figure C.7. Crack initiation region of specimen P 111 tested at $\Delta\varepsilon = 0.94\%$. A small particle lies at the surface of the specimen.

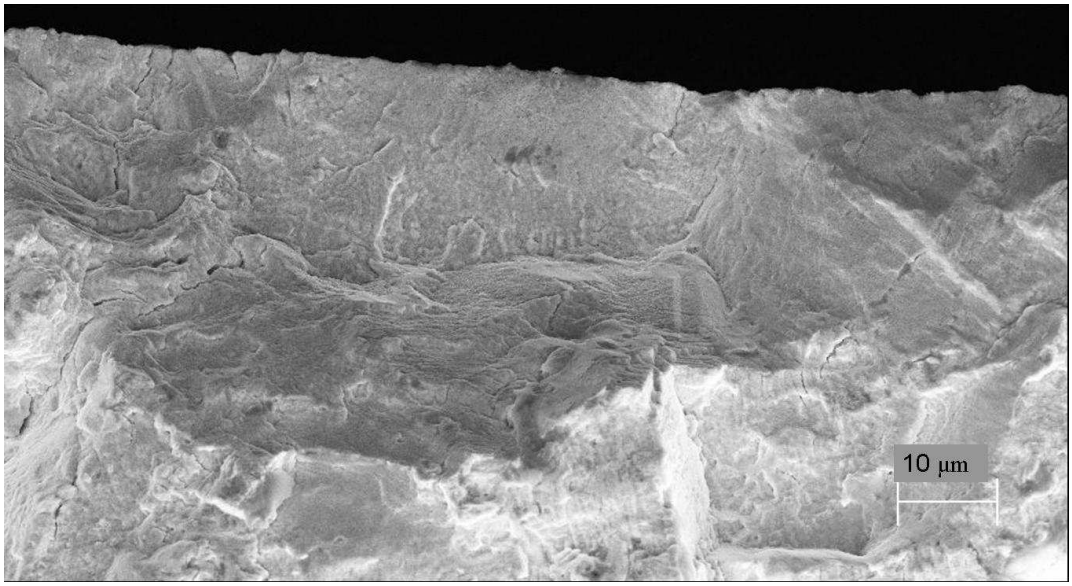

Figure C.8. Crack initiation region of specimen P 200 tested at $\Delta\varepsilon = 1.15\%$.

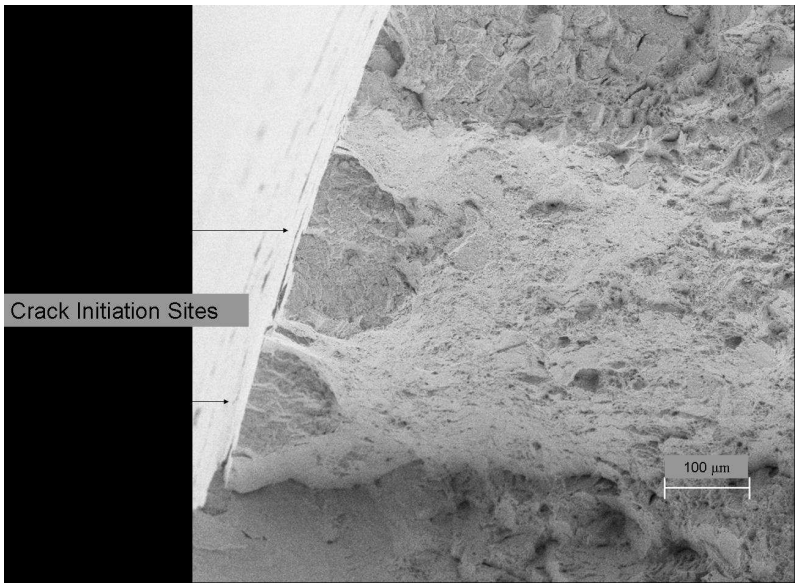

Figure C.9. Crack initiation region of an O condition specimen tested at $\Delta\varepsilon = 1.5\%$ exhibiting adjacent crack initiation sites.

REFERENCES

1. Krueger, D.D., Kissinger, R.D., Menzies, R.G. *Development and Introduction of a Damage Tolerant High Temperature Nickel-Base Disk Alloy, Rene 88DT*. in *Superalloys 1992: 7th International Symposium*. 1992. Champion, PA.

2. Caton, M.J., Jha, S.K., Rosenberger, A.H., Larsen, J.M., *Divergence of Mechanisms and the Effect on the Fatigue Life Variability of Rene 88DT*, in *Superalloys 2004*. 2004. p. 305-312.

3. Newman, J.C., Raju, I.S., *Stress Intensity Factor Equations for Cracks in Three-Dimensional Finite Bodies*, in *Fracture Mechanics: Fourteenth Symposium - Volume I: Theory and Analysis*, J.C. Lewis, Sines, G., Editor. 1983.

4. Carpintieri, A., *Elliptical-Arc Surface Cracks in Round Bars.* Fatigue and Fracture of Engineering Materials and Structures, 1992. **15**(11): p. 1141-1153.

5. Romanoski, G.P., Pelloux, R.M. *The Fatigue Behavior of Small Cracks in an Aircraft Turbine Disk Alloy*. in *Elevated Temperature Crack Growth: Proceedings of Symposium, ASME Winter Annual Meeting*. 1990. Dallas, TX.

6. Backman, D.G., Mourer, D.P., Bain, K.R., Walston, W.S. *AIM - A New Methodology for Developing Disk Materials*. in *Minerals, Metals, adn Materials Society (TMS), Advanced Materials and Processes for Gas Turbines*. 2003. USA.

7. Durand-Charre, M., *The Microstructure of Superalloys*. 1997: Gordon and Breach Science Publishers.

8. Gessinger, G.H., *Powder Metallurgy of Superalloys*. 1984: Butterworth and Company.

9. Kriege, O.H., Baris, J.M., *The Chemical Partitioning of Elements in Gamma Prime Separated from Precipitation Hardened, High-Temperature Nickel-Base Superalloys.* Transactions of ASM, 1969. **62**: p. 195-200.

10. Wlodek, S.T., Kelly, M., Alden, D.A. *The Structure of Rene 88 DT*. in *Superalloys 1996; 8th International Symposium*. 1996. Champion, PA.

11. Mao, J., Chang, K., Yang, W., Furrer, D.U., Ray, K., Vaze, S.P., *Cooling Precipitation and Strengthening Study in Powder Metallurgy Superalloy Rene88DT.* Materials Science and Engineering A, 2002. **332**(1-2): p. 318-329.

12. Stoloff, N.S. *Wrought and P/M Superalloys*. in *ASM International, Metals Handbook*. 1990.

13. Yeom, S.J., Yoon, D.Y., Henry, M.F., *The Morphological Changes of Gamma Prime Precipitates in Ni-8Al (Wt Pct) Alloy During Their Coarsening.* Metallurgical Transactions A, 1992. **24A**: p. 1975-1981.

14. Khachaturyan, A.G., Semenovskaya, S.V., Morris Jr., J.W., *Theoretical Analysis of Strain-Induced Shape Changes in Cubic Precipitates During Coarsening.* Acta Metallurgica. **36**: p. 1563-1572.

15. Parker, B.A., West, D.R.F., *The Influence of Particle/Matrix Interfacial Mismatch on the Size, Shape, and Distribution of Coherent γ′ Particles in Nickel-Based Alloys.* The Journal of Australian Institute of Metals. **14**(2): p. 102-110.

16. Liu, L., Sommer, F., *Effect of Solidification Conditions on MC Carbides in a Nickel-Base Superalloy IN 738 LC.* Scripta Metallurgica, 1994. **30**: p. 587-591.

17. Garosshen, T.J., McCarthy, G.P., *Low Temperature Carbide Precipitation in a Nickel Base Superalloy.* Metallurgical Transactions A, 1984. **16A**: p. 1213-1223.

18. Kotval, P.S., Hatwell, H., *Discontinuous Precipitation of M23C6 Carbide in a Nickel-Base Superalloy.* Transactions of the Metallurgical Society of AIME, 1969. **245**: p. 1821-1823.

19. Chang, D.R., Krueger, D.D., Sprague, R.A. *Superalloy Powder Processing, Properties and Turbine Disk Applications*. in *Superalloys 1984: Fifth International Symposium*. 1984. Champion, PA.

20. Crompton, S., Hertzberg, R.W., *Analysis of Second Phase Particles in a Powder Metallurgy HIP Nickel-base Superalloy.* Journal of Materials Science, 1986. **21**: p. 3445-3454.

21. Reichman, S., Chang, D.S., *Powder Metallurgy*, in *Superalloys II*. 1987, John Wiley and Sons, Inc.

22. Moll, J.H., McTiernan, B.J., *Powder Metallurgy Superalloys*, in *ASM Handbook Powder Metal Technologies and Applications*. 1998. p. 887-902.

23. Boyd-Lee, A., King, J.E., *Short Fatigue Crack Path Determinants in Polycrystalline Ni-Base Superalloys.* Fatigue and Fracture of Engineering Materials and Structures, 1994. **17**(1): p. 1-14.

24. Boyd-Lee, A., *Fatigue Crack Growth Resistant Microstructures in Polycrystalline Ni-base Superalloys for Aeroengines.* International Journal of Fatigue, 1999. **21**: p. 393-405.

25. Jablonski, D.A., *The Effect of Ceramic Inclusions on the Low Cycle Fatigue Life of Low Carbon Astroloy Subjected to Hot Isostatic Pressing.* Materials Science and Engineering A, 1981. **48**: p. 189-198.

26. Hyzak, J.M., Bernstein, I.M., *The Effect of Defects on the Fatigue Crack Initiation Process in Two P/M Superalloys.* Metallurgical Transactions A, 1982. **13A**: p. 33-52.

27. Gell, M., Leverant, G.R. *Fracture*. in *Second International Conference on Fracture*. 1969. London.

28. Byrne, J., *Influence of Sub-surface Defects on Low-Cycle Fatigue Life in a Gas Turbine Disc Alloy at Elevated Temperature.* International Journal of Fatigue, 1999. **21**(2): p. 195-206.

29. Miner, R.V., Dreshfield, L., *Effects of Fine Porosity on the Fatigue Behavior of a Powder Metallurgy Superalloy.* Metallurgical Transactions A, 1981. **12A**: p. 261-267.

30. Luo, J., Bowen, P., *Statistical Aspects of Fatigue Behavior in a PM Ni-Base Superalloy Udimet 720.* Acta Materialia, 2003. **12**(51): p. 3521-3535.

31. Miner, R.V., Gayda, J., *Effects of Processing and Microstructure on the Fatigue Behavior of the Nickel-base Superalloy Rene 95.* International Journal of Fatigue, 1984. **6**: p. 189-193.

32. Boyd-Lee, A., King, J.E., *Discrete Statistical Model of Fatigue Crack Growth in a Ni-base Superalloy, Capable of Life Prediction.* Fatigue Design, 1993. **16**: p. 283-296.

33. Healy, J.C., Grabowski, L., Beevers, C.J., *Monitoring Fatigue of a Nickel-Base Superalloy at Positive and Negative Stress Ratios Using an Optical System.* Fatigue and Fracture of Engineering Materials and Structures, 1991. **15**(3): p. 309-321.

34. Healy, J.C., Grabowski, L., Beevers, C.J., *Short-fatigue-crack Growth in a Nickel-base Superalloy at Room and Elevated Temperature.* International Journal of Fatigue, 1991. **13**(2): p. 133-138.

35. Albrecht, J., *Comparing Fatigue Behavior of Titanium and Nickel-Based Alloys.* Materials Science and Engineering A, 1999. **A263**: p. 176-186.

36. Alexandre, F., Deyber, S., Pineau, A., *Modelling the Optimum Grain Size on the Low Cycle Fatigue Life of a Ni Based Superalloy in the Presence of Two Possible Crack Initiation Sites.* Scripta Materialia, 2004. **50**: p. 25-30.

37. Bennett, V.P., McDowell, D.L., *Polycrystal Orientation Distribution Effects on Microslip in High Cycle Fatigue.* International Journal of Fatigue, 2003. **25**: p. 27-39.

38. Antolovich, S.D., *The Effect of Microstructure on the Fatigue Crack Growth Resistance of Nickel Base Superalloys*. 1987.

39. Dennison, J.P., Holmes, P.D., Wilshire, B., *The Creep and Fracture Behavior of Cas, Nickle-based Superalloy, IN100.* Materials Science and Engineering, 1978. **33**: p. 35-47.

40. Floreen, S., Kane, R.H., *An Investigation of the Creep-Fatigue-Environment Interaction in a Ni Base Alloy.* Fatigue and Fracture of Engineering Materials and Structures, 1980. **2**: p. 151-164.

41. Pineau, A., *Fatigue and Creep-Fatigue Behavior of Ni-Base Superalloys: Microstructural and Environmental Effects*, in *Mechanical Behavior of Materials at High Temperature*. 1996, Kluwer Publishers. p. 135-144.

42. Kang, B.S.-J., Zhang, G., Liu, P., Ellathur, M. *Stress Accelerated Grain Boundary Oxygen Embrittlement on Creep Crack Growth of Nickel-Base Superalloys*. in *Fatigue and Fracture at Elevated Temperatures: 1995 ASME International Mechanical Engineering Congress and Exposition*. 1995. San Francisco, CA.

43. Kissinger, R.D., *Cooling Path Dependent Behavior of a Supersolvus Heat Treated Nickel Base Superalloy*, in *Superalloys 1996*. 1996. p. 687-695.

44. *ASTM Standard E139-96*, in *Annual Book of ASTM Standards*. 1998.

45. *ASTM Standard E606-92*, in *Annual Book of ASTM Standards*. 1998.

46. *ASTM Standard E1820-01*, in *Annual Book of ASTM Standards*. 2001.

47. *ASTM Standard E647-00*, in *Annual Book of ASTM Standards*. 2000.

48. Saxena, A., *Electrical Potential Drop Technique for Monitoring Subcritical Crack Growth at Elevated Temperatures.* Engineering Fracture Mechanics, 1980. **13**: p. 741-750.

49. Suresh, S., *Fatigue of Materials*. 2 ed. 1998: Cambridge University Press.

50. *NIST Propery Data Summaries for Advanced Materials*. 2001.

51. *ASTM Standard E561-98*, in *ASTM Annual Book of Standards*. 1998.

52. Saxena, A., *Nonlinear Fracture Mechanics for Engineers*. 1998: CRC Press.

53. Caspers, M., Mattheck, C., Munz, D., *Fatigue Crack Propagation in Cylindrical Bars.* Z. Werkstofftech, 1986. **17**: p. 327-333.

54. Lin, X.B., Smith, R.A., *Shape Growth Simulation of Surface Cracks in Tension Fatigued Round Bars.* International Journal of Fatigue, 1997. **19**(6): p. 461-469.

55. Carpintieri, A., *Shape Change of Surface Cracks in Round Bars Under Cyclic Axial Loading.* International Journal of Fatigue, 1993. **15**(1): p. 21-26.

56. Venkataraman, G., Chung, Y.W., Mura, T., *Application of Minimum Energy Formalism in a Multiple Slip Band Model for Fatigue-I. Calculation of Slip Band Spacings.* Acta Metallurgica et Materialia, 1991. **39**(11): p. 2621-2629.

57. Venkataraman, G., Chung, Y.W., Mura, T., *Application of Minimum Energy Formalism in A Multiple Slip Band Model For Fatigue - II. Crack Nucleation and Derivation of a Generalized Coffin-Manson Law.* Acta Metallurgica et Materialia, 1991. **39**(11): p. 2631-2638.

58. Fatemie, A., Socie, D.F., *Critical Plane Approach to Multiaxial Fatigue Damage Including Out-of-Phase Loading.* Fatigue and Fracture of Engineering Materials and Structures, 1988. **11**(3): p. 149-165.

59. McDowell, D.L., K.O. Findley, Personal Communication. 2005. Use of Venkataraman and Fatemi-Socie parameters for crack initiation.

60. Bailon, J.P., Antolovich, S.D., *Effect of Microstructure on Fatigue Crack Propagation: A Review of Existing Models and Suggestions for Further Research*, in *Fatigue Mechanisms: Advances in Quantitative Measurement of Physical Damage*. 1983, American Society for Testing and Materials.

61. Westergaard, H.M., *Bearing Pressures and Cracks.* Journal of Applied Mechanics, 1939. **6**: p. 49-53.